Proceedings of

MMM

Third International Conference

Multiscale Materials Modeling

September 18-22, 2006, Freiburg, Germany

Symposium 2
Nanomechanics and Micromechanics

Peter Gumbsch
Editor and Conference Chair

Organized by Fraunhofer-Institute for Mechanics of Materials.
Hosted by University of Freiburg.

IWM
Fraunhofer Institut Werkstoffmechanik

ALBERT-LUDWIGS-UNIVERSITÄT FREIBURG

Imprint

Papers published in this volume constitute the proceedings of the Third International Conference on Multiscale Materials Modeling. Papers were selected by the program committee for oral or poster presentation. They are published as submitted, in the interest of timely dissemination.

Contact
Fraunhofer Institute for Mechanics of Materials IWM
Woehlerstraße 11
79108 Freiburg
Germany
Phone + 49 761 5142 0
Fax + 49 761 5142 110

The complete proceedings of the conference are available at

Fraunhofer Information-Centre for Regional Planning and Building Construction IRB
P.O. Box 80 04 69, D-70504 Stuttgart
Nobelstrasse 12, D-70569 Stuttgart
Fon +49 (0) 7 11/9 70-25 00
Fax +49 (0) 7 11/9 70-25 07
E-Mail irb@irb.fraunhofer.de
URL www.irb.fraunhofer.de
ISBN-10: 3-8167-7206-4
ISBN-13: 978-3-8167-7206-4

Foreword

Computational modeling of materials behavior by multiscale materials modeling (MMM) approaches is becoming a reliable tool to underpin scientific investigations and to complement traditional theoretical and experimental approaches of component assessment. At transitional (microstructural) scales continuum approaches begin to break down and atomistic methods reach inherent limitations in time and length scale. Transitional theoretical frameworks and modeling techniques are developed to bridge the gap between the different length scales.

Industrial success in high technology fields relies on the possibility to specifically engineer materials and products with improved performance. The success factor is the ability to make these material related developments timely at relatively low-costs. This demands not only the rapid development of new or improved processing techniques but also better understanding and control of material chemistry, processing, structure, performance, durability, and their relationships. This scenario usually involves multiple length and time scales and multiple processing and performance stages, which are usually only accessible via multi-scale / multi-stage modeling or simulation.

In high-payoff, high-risk technologies such as the design of large structures in the aerospace and nuclear industries, the effects of aging and environment on failure mechanisms cannot be left to conservative approaches. Increasing efforts are now focused on advancing MMM approaches to develop new material systems components and devices. Appropriate validation experiments are crucial to verify that the models predict the correct behavior at each length scale. Thus, one of the advantages of these MMM approaches is that, at each scale, physically meaningful parameters are predicted and used in models for subsequent scales, avoiding the use of empiricism and fitting parameters.

Recent interest in nanotechnology is challenging the scientific community to design nanometer to micrometer size devices for applications in new generations of computers, electronics, photonics or drug delivery systems. These new application areas of multiscale materials modeling require novel and sophisticated science-based approaches for design and performance evaluation. Theory and modeling are playing an increasing role to reduce development costs and manufacturing times. With the sustained progress in computational power and MMM methodologies, new materials and new functionalities are increasingly more likely discovered by MMM approaches than by traditional trial and error approach. This is part of a paradigm shift in modeling, away from reproducing known properties of known materials towards simulating the behavior of hypothetical composites as a forerunner to finding real materials with these novel properties.

The MMM 2006 conference provides an international forum for the scientific advances of multiscale modeling methodologies and their applications.

I would like to thank the members of the international advisory committee, the local program committee and particularly the organizing team, the symposium organizers and the session chairs and the University of Freiburg for their engagement and support. Without their hard work and their devotion of time and ressources, the Third International Conference Multiscale Materials Modeling would not have been possible.

Finally, I would like to thank our conference sponsors for their financial support: The German Research Foundation DFG, Accelrys Inc., Plansee S.E. and the Ministry of Science, Research and Art, Baden-Württemberg.

Peter Gumbsch
Conference Chair

Conference Committee

International Advisory Committee

Prof. Bacon, David	University of Liverpool, UK
Dr. Baskes, Michael	Los Alamos National Laboratory, USA
Prof. Busso, Esteban	Imperial College, London, UK
Prof. Cale, Timothy S.	Rensselaer Polytechnic Institute, Troy, USA
Dr. Diaz de la Rubia, Tomas	Lawrence Livermore National Lab., USA
Prof. Ghoniem, Nasr	University of California, Los Angeles, USA
Prof. Guo, Xiao	Queens College, London, UK
Prof. Iwata, Shuichi	University of Tokyo, Japan
Prof. Kratochvil, Jan	Technical University, Prague, Czech Republic
Prof. Kremer, Kurt	Max Planck Institute, Mainz, Germany
Dr. Kubin, Ladislas	ONERA-LEM, Chatillon, France
Dr. LeSar, Richard	Los Alamos National Laboratory, USA
Prof. Meguid, Shaker	University of Toronto, Canada
Prof. Needleman, Alan	Brown University, Providence, USA
Prof. Odette, Robert	University of California, Santa Barbara, USA
Prof. Ortiz, Michael	California Institute of Technology, USA
Prof. Pettifor, David	Oxford University, UK
Prof. Phillips, Robert	California Institute of Technology, USA
Prof. Raabe, Dierk	Max Planck Institute, Düsseldorf, Germany
Prof. Shibutani, Yoji	Osaka University, Japan
Dr. Soneda, Naoki	Komae Research Laboratory, Tokyo, Japan
Prof. Suresh, Subra	Massachusetts Institute of Technology, USA
Prof. Tomita, Yoshihiro	Kobe University, Japan
Prof. Van der Giessen, Erik	University of Groningen, Netherlands
Prof. Walgraef, Daniel	Free University of Brussels, Belgium
Dr. Wolf, Dieter	Argonne National Laboratory, USA
Prof. Yip, Sidney	Massachusetts Institute of Technology, USA
Dr. Zinkle, Steve	Oak Ridge National Laboratory, USA

Organizing Committee

M. J. Alava	Helsinki University of Technology, Finland
D. Dimiduk	The Ohio State University, USA
M. Dao	Massachusetts Institute of Technology, USA
M. Doi	University of Tokyo, Japan
C. Elsässer	Fraunhofer IWM, Germany
E. v. d Giessen	University of Gronigen, Netherlands
N. Gov	The Weizmann Institute of Science, Israel
H. J. Herrmann	University of Stuttgart, Germany
R. James	University of Minnesota, USA
K. Kremer	Max Planck Institute for Polymer Research, Germany
J. Korvink	IMTEK, University of Freiburg, Germany
J. Li	The Ohio State University, USA
S. Müller	Max Planck Institute for Mathematics in the Sciences, Germany
A. Paxton	Queen’s University, Belfast, UK
M. Payne	University of Cambridge, UK
D. Raabe	Max Planck Institute fuer Eisenforschung, Germany
N. Soneda	Central Research Institute of Electric Power Industry, Japan
M. Zaiser	University of Edinburgh , UK
S. Zapperi	University of Rome, Italy
F. Willaime	Commissariat a l’Energie Atomique (CEA), France
B. Wirth	University of California, Berkely, USA

Contents

Symposium 2

Symposium 2

Nanomechanics and micromechanics

CRACK GROWTH ALONG SYMMETRICAL TILT GRAIN BOUNDARIES IN COPPER BICRYSTALS

A. Luque, J. Aldazabal, J.M. Martínez-Esnaola, J. Gil Sevillano

CEIT and TECNUN (Universidad de Navarra)
P. Manuel Lardizábal 15, 20018 San Sebastián (Spain)
E-mail: jgil@ceit.es Phone: + 34 943 212800 Fax: + 34 943 213076

ABSTRACT

Mode I crack growth along some grain boundaries of Bi-embrittled copper shows strong anisotropy. For instance, growth along $[1\bar{1}\bar{4}]$ direction on the $\Sigma 9[110]/(2\bar{2}1)$ symmetrical tilt boundary occurs by intergranular brittle fracture, whereas growth along the opposite sense $[\bar{1}14]$ occurs in a ductile manner. In this paper we simulate such growth using molecular dynamics (MD, embedded atom method) in 3-dimensional perfect bicrystalline samples of pure copper of the above orientation at 300 K. In both cases the response is ductile, the crack opening taking place by dislocation emission from the crack tip. The critical stress intensity factors for dislocation emission have been calculated by matching the atomic displacement fields around the tip with the continuum elastic fields. They are of the same order of magnitude for both configurations despite the different morphology of their blunted crack tips and of the patterns of dislocations constituting their plastic zones. It seems that, in agreement with published results of continuum crystalline plasticity for the same problem, the plastic anisotropy associated with the orientation of the slip systems with respect to the crack cannot explain the experimental behaviour observed with Bi-embrittled bicrystals.

1. Introduction

It has been experimentally observed that fracture along the grain boundary of bicrystalline samples depends on the crack growth direction. For embrittled copper, some differences were also observed attending to the sense of growth [1]: a copper bicrystal with the symmetric tilt grain boundary $\Sigma 9[110]/(2\bar{2}1)$ shows this behaviour. Fracture is "essentially ductile" (blunting by dislocation emission), when the crack grows along $[\bar{1}14]$ but when the crack grows along the opposite sense, the observed behaviour is "essentially brittle" (cleavage). Rice and Thomson's criterion distinguishes between the ductile and brittle behaviour of a crack, considering the energetic competence between dislocation emission, G_{disl}, and interfacial decohesion, G_{cleav}. A continuum mechanics calculation predicts $G_{\mathrm{cleav}} \approx G_{\mathrm{disl}}$ for crack growth along $[\bar{1}14]$ and $G_{\mathrm{cleav}} < G_{\mathrm{disl}}$ for crack growth along $[1\bar{1}\bar{4}]$ in pure copper in agreement with Wang and Andersons' experimental work on Bi-embrittled copper bicrystals. The natural explanation for this seems to be the asymmetric configuration of the slip systems with respect to the yz plane (Fig. 1). However, Saeedvafa [2] and other authors showed, by small strain finite element models and hardening at continuum level, that stresses at the tip were not substantially different for the experimental ductile and brittle configurations. The strain fields were different, the plastic zone in the ductile configuration being bigger than in the brittle case. In this work, we have studied crack growth along $\Sigma 9[110]/(2\bar{2}1)$ in pure-copper bicrystals by means of molecular dynamics (MD).

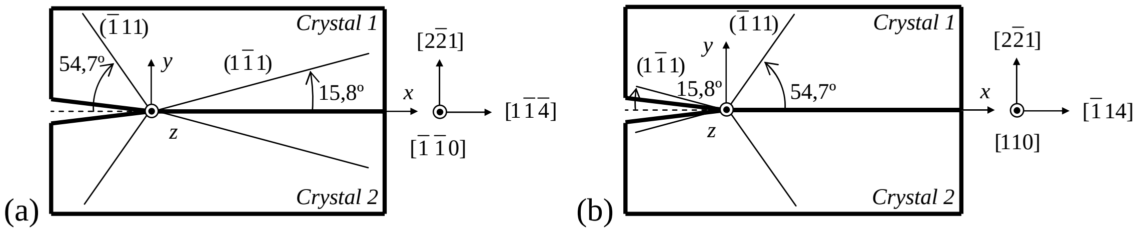

Figure. 1. 2-dimensional representation of a symmetrical tilt boundary $\Sigma 9[110]/(2\bar{2}1)$ in a bicrystal: (a) brittle configuration and (b) ductile configuration.

2. Simulation Method

Atomistic simulations have been performed using the embedded atom method (EAM [3]). The method considers that each atom is under the effect of a nuclear interaction, given by a pair potential, and an electronic interaction, given by an embedding potential that depends on the local electronic density. We use potential values corresponding to copper atoms tabulated in [4]. With these values, forces are evaluated and atomic trajectories are calculated using very small time steps ($\Delta t = 2.5\times10^{-15}$ s). System temperature was set to 300 K and atoms were given an initial velocity of random direction and of modulus equal to the mean velocity equivalent to that temperature. To maintain the system temperature at a constant value, the velocity scaling technique [5] was used in each step. This technique modifies the modulus of the atomic velocities in such a way that the system mean velocity equals the mean velocity that corresponds to the target temperature.

3. Specimen and Test Characterisation

Two 3-dimensional bicrystalline copper specimens of dimensions 23 nm × 15 nm × 9 nm were generated. Each one had a 0.55 nm wide crack,, introduced by removing grain boundary atoms up to half the length of the sample along the *x*-axis. The difference between the samples was the sense of crack growth: it was $[\bar{1}14]$ in the first case (Fig. 2a), and $[1\bar{1}\bar{4}]$ in the second case (Fig. 2b). Two rigid zones of 0.55 nm of width were established at the two opposite ends of the specimen. They were used as clamps during the tests, in which a constant displacement of 3.78×10^{-15} m per step was set along the *y*-axis to each rigid zone. Periodic boundary conditions were imposed along the *z*-axis, while the surfaces perpendicular to *x*- and *y*-axis were free to move. As grain boundary is an atomically disordered region with respect to the perfect crystal, a quasi-static relaxation at 0 K was performed for 25 ps, followed by a 2nd relaxation process at 300 K for 5 ps before starting the sample displacement. This brought the bicrystal to a metaestable energetic state. However, the system turned to be compressively charged due to the applied boundary conditions [6]. During the simulations, the remote load and the imposed displacements were recorded. Atomic positions were periodically stored for analysis in terms of tip blunting and plastic-zone size [7].

4. Results

Fig. 2.a shows the remote nominal stress, σ_{nom} vs. the relative elongation of the specimen, $\Delta L/L_0$. σ_{nom} is calculated as the resulting force along *y*-axis applied over the atoms of the rigid layer, divided by the layer area. For both configurations, stress values are very similar. The compressive stress zone is not shown. Oscillations are due to the temperature. The mechanical behaviour observed is elastic, with apparent Young’s modulus around 100 GPa, up to the dislocation emission.

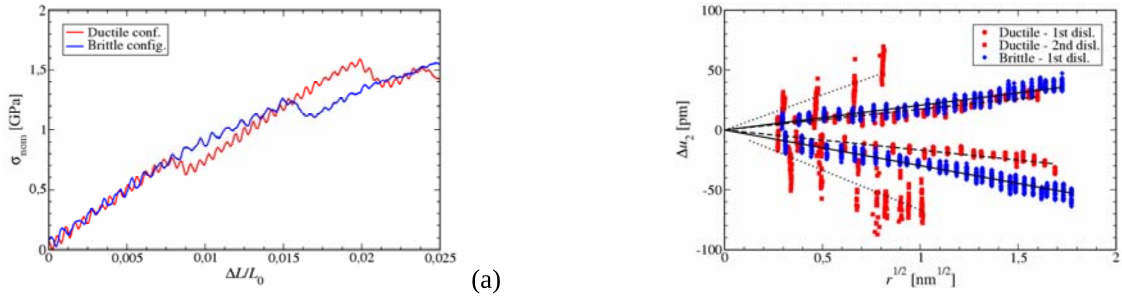

(a) (b)

Figure 2. (a) Remote nominal stress vs. relative elongation curves of the bicrystalline configuration studied. (b) Relative opening displacement as a function of $r^{1/2}$.

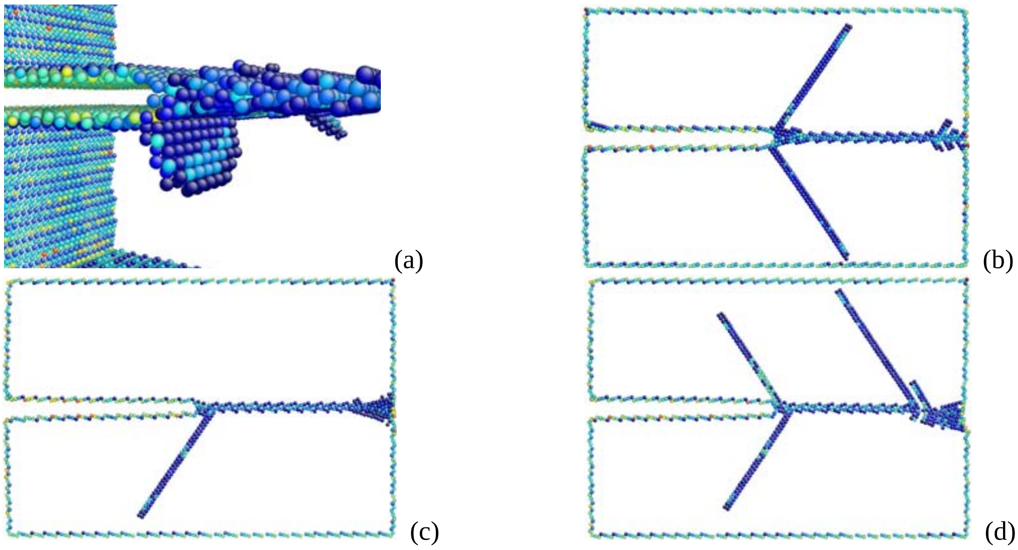

Figure 3. Centrosymmetry of the surroundings of the atoms in the ductile configuration when $\Delta L/L_0$ equals (a) 0.0079 and (b) 0.0208, and in the brittle configuration when $\Delta L/L_0$ equals (c) -0.0008 and (d) 0.0188. Fcc-arranged atoms are not shown.

In the ductile configuration, the elastic regime extends up to $\Delta L/L_0 = 0.0079$ and finishes with the emission of a dislocation. The dislocation, a partial $1/6<112>$, first nucleates in the crack tip (Fig. 3a) and is then emitted along $(\bar{1}11)$. The figure represents a centrosymmetry parameter [7], which characterises the symmetric inversion in the surroundings of each atom. Later, new dislocations are emitted from the outer end of the grain boundary. When $\Delta L/L_0 = 0.0199$, a second partial dislocation is emitted from the tip (Fig. 3b). The bicrystal in the brittle configuration remains in the linear-elastic regime up to $\Delta L/L_0 = 0.008$. However, when the load is first applied, a dislocation is emitted from the crack tip (Fig. 3c). Considering the low stress level for such emission (of the order of the thermal oscillations), the emission must be associated to a local instability of the grain boundary, which favours the emission of this dislocation. From $\Delta L/L_0 = 0.008$ on, there is some dislocation activity in $(1\bar{1}1)$ and $(\bar{1}11)$ far from the tip. When $\Delta L/L_0 = 0.0149$, the generation of a new dislocation occurs at the tip (Fig. 3d).

The stress intensity factor for dislocation emission from the crack tip was calculated. The atomic displacement field in the surrounding of the crack was fitted to the continuum linear elastic solution [8]. For the relative normal displacement, Δu_2, a relationship proportional to $r^{1/2}$ is assumed, r being the distance to the crack tip. This elastic solution is only valid down to certain distance from the tip. Figure 2b shows the evolution of Δu_2 with $r^{1/2}$ for $r \leq 3\,\text{nm}$. Table 1 summarizes the toughness K_c, for the emission of the 1st dislocation from the crack tip for both configurations, and for the emission of the 2nd dislocation in the ductile case. The critical nominal stresses for these dislocations are also included. These values are lower than the ones found in the literature for dislocation emission from crack tips in copper single crystals. Considering the specific bi-crystallography and the presence of the grain boundary at the crack tip, it is reasonable that dislocation emission is favoured.

Table 1. Critical remote stress and toughness for the emission of dislocations from the tip.

Configuration	σ_c (GPa)	K_c (MPa√m)
Ductile – 1st dislocation	0.77	0.054
Brittle – 1st dislocation	1.26	0.080
Ductile – 2nd dislocation	1.59	0.198

5. Conclusions

Mode I crack growth along $\Sigma 9[110]/(2\bar{2}1)$ in copper bicrystals was analysed. Two different simulations were carried out in opposite senses of advance of the crack, namely $[\bar{1}14]$ and $[1\bar{1}\bar{4}]$. After a pure elastic behaviour, cracks blunt by dislocation emission. In the "ductile" configuration, dislocation generation occurs at a lower σ_{nom} than in the "brittle" configuration. The dislocations emitted from the tip are partial 1/6{111}<221>. Considering the atomic normal displacements, K_c for blunting was calculated. A value of 0.054 MPa√m is found for dislocation emission from the tip in the "ductile" sense and a value of 0.080 MPa√m in the "brittle" one. In the latter case, blunting occurs before cleavage for pure copper. Bismuth embrittement should be thus responsible for the experimental results of Wang and Anderson.

Acknowledgements

Authors would like to thank the Education, Universities and Research Department of the Basque Government and the Ministry of Education and Science, for the financial support of this work, through research projects EX2002-6 and MAT2003-04314, respectively. One of the authors, AL, also acknowledges the Fundación de Centros Tecnológicos – Iñaki Goenaga for the grant received to carry out his PhD.

References

[1] Wang, J.-S. and Anderson, P.M., "Fracture behaviour of embrittled FCC metal bicrystals", *Acta Metall. Mater.*, 39, 779-792 (1991).
[2] Saeedvafa, M., "Orientation dependence of fracture in copper bicrystals with symmetric tilt boundaries", *Mechanics Mater.*, 13, 295-311 (1992).
[3] Daw, M.S. and Baskes, M.I., "Embedded-atom method: derivation and application to impurities, surfaces and other defects in metals", *Phys. Rev. B*, 29, 6443-6453 (1984).
[4] Mishin, Y., Farkas, D., Mehl, M.J., "Structural stability and lattice defects in copper: ab-initio, tight-binding and embedded-atom calculations", *Phys. Rev. B*, 63, 224106 (2001).
[5] D.C. Rapaport, *The Art of Molecular Dynamics Simulation*, Cambridge University Press, Cambridge, 2001, p. 65.
[6] Diao J., Gall, K. and Dunn, M.L., "Suface-stress-induced phase transformation in metal nanowires", Nature Materials, 2, 656-660.
[7] Li, J., "AtomEye: an efficient atomistic configuration viewer", *Modelling Simul. Mater. Sci. Eng.*, 11, 173-177 (2003).
[8] Luque A., Aldazabal J., Martínez-Esnaola J.M., Gil Sevillano J., "Atomistic simulation of tensiole strength and toughness of cracked Cu nanowires", *Fatigue Fract. Eng. Mat. Struct.*, 29, 615-622 (2006).

Modeling Size Effects in Sub-Micron Compression Samples

Peter Anderson[1], *Lin Li*[1], *William D. Nix*[2], *Seung Min Han*[2]

[1]*Dept Materials Science and Engineering, Ohio State University, 2041 College Rd, 43201 Columbus, USA*
[2]*Dept. Materials Science and Engineering, Stanford University, 416 Escondido Mall, Peterson Bldg., 94305-4045 Stanford, USA*

Recent compression testing of gold pillars with submicron diameters shows flow strengths as large as 50 times that of bulk counterparts. Corresponding transmission electron microscopy of deformed pillars reveals small dislocation densities, suggesting that such large strengths cannot be explained via traditional strain hardening concepts. Stress-strain traces at uniform strain rate show a rapid build-up to a peak stress, followed by repeated release and build-up of stress. A cellular-automaton model is implemented to determine if these results can be explained by evolution of dislocation content inside a deforming pillar. The model is bas ed on discretizing pillars into cells with prescribed initial dislocation density and distribution of dislocation source lengths. Dislocation density in each cell evolves due to source operation, dislocation breeding, exchange of dislocation content, and load shedding.

These processes are affected by nearby free surfaces present in sub-micron samples, making dislocation cell structure dependent on sample size. Numerical challenges arise due to vastly different dislocation velocities inside versus outside dislocation cells. The model predictions and assumptions are assessed in light of recent experimental stress-strain data.

Prediction of the Morphology of Martensite in Nano-Structured Ni-Ti Alloys

T. Antretter[1], T. Waitz[2], W. Pranger[1], F.D. Fischer[1]

[1]Institute of Mechanics, Montanuniversität Leoben, Franz-Josef Straße 18, A-8700 Leoben, Austria, antrette@unileoben.ac.at; [2]Institute of Materials Physics, University of Vienna, Boltzmanngasse 5, A-1090 Vienna, Austria, waitz@ap.unvie.ac.at

ABSTRACT

Nano-structured NiTi instantaneously transforms from fcc austenite via an intermediate phase (the R-phase) into monoclinic B19' martensite. At a grain size less than a critical limit of about 50nm no transformation can be observed even upon cooling down to cryogenic temperatures. In slightly larger grains the martensite appears as a laminate of alternating twin-related Bain correspondence variants. For grain diameters in the order of 100nm it becomes more likely to observe two such martensite laminates whose arrangement relative to each other, as it appears in a micrograph, gives the impression of a "herring-bone pattern". This term has widely been adopted in the literature for this particular formation.

This paper focuses on the prediction of the resulting morphology, which is determined by the energies involved, i.e. the chemical and mechanical contributions as well as interface energies. This paper evaluates the elastic strain energy as well as the interface energies generated by the transformation eigenstrains of the newly created phases. Various arrangements are calculated and compared with each other in terms of their impact on the total energy balance. Such an approach allows to determine an optimum configuration minimizing the total energy introduced into the system. The herring-bone morphology is also compared with the case of a single laminate as an alternative energy release mechanism. The parameters defining the geometry of the laminates such as the twin band thickness or the laminate width are computed and verified by means of high-resolution TEM images.

1. Introduction

NiTi alloys are the most important practically used shape memory alloys [1]. In contrast to their conventional coarse-grained counterparts, bulk nanocrystalline NiTi alloys attract considerable attention as advanced functional material [2]. In nanograins of NiTi a unique path of atomic scale twinning is encountered [3]. A variety of martensite arrangements allows to accommodate the newly created phase in order to maximize the energy release triggered by the transformation. It is the objective of the present study to investigate the dependence of the martensitic morphology on the grain size of nanocrystalline NiTi alloys by numerical as well as experimental means using transmission electron microscopy (TEM).

Martensitic phase transformations are characterized by the formation of multiple symmetry related variants of the martensite building complex microstructures on different length scales [4]. The eigenstrains that occur during the transformation from the parent austenitic phase to the martensite of lower crystalline symmetry enforce arrangements of fine mixtures of compensating variants that minimize the free energy [5]. The twinned martensitic microstructure strongly depends on the crystallography of the transformation. Similarly, a small grain size of the parent phase can impose geometrical constraints that might significantly affect the martensitic morphology [6].

Fig 1 a and b show TEM bright field images of grains of different size (diameter of about 50 and 100 nm, respectively) that contain B19´ martensite. Atomic scale twinning of the martensite leads to an ultrahigh density of the twins. The twins have equal volume fractions, and their average width is about 2 nm. Different martensitic morphologies are observed in grains of different size: In small enough grains frequently a single laminate of a twinned martensite sequence is encountered (see Fig. 1a). In grains in the order of 100 nm, a banded structure of two such laminates V1 and V2, separated by junction planes indicated by the dashed lines, is observed (see Fig. 1b). The angle between the twin boundary planes (i.e. the solid lines) is 125°. The width of the variant V2 is about 22% of the grain size (measured in a direction normal to the dashed lines).

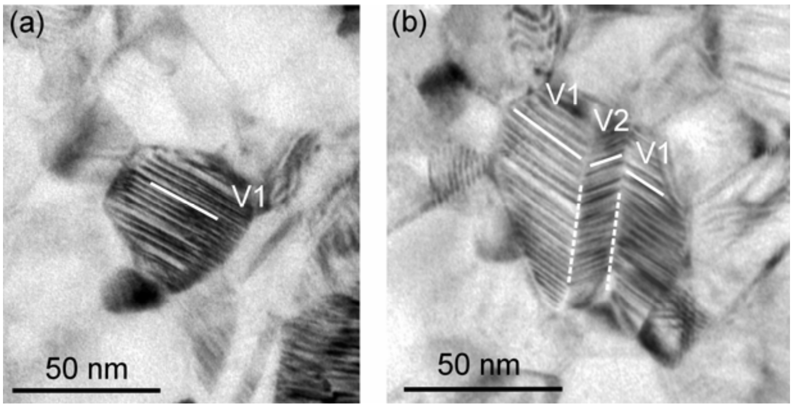

Figure 1. TEM micrographs of martensitic nanograins in NiTi. Atomic scale compound twins of B19´ are indicated by solid white lines. (a) Single variant of twinned martensite. (b) Herringbone morphology of two variants V1 and V2 of twinned martensite (dashed lines indicate the junction planes of V1 and V2).

2. Modeling and Results

For the time being a two-dimensional approach has been chosen in order to enable parametric studies in a cost-effective way. Fig. 2a shows the geometry of a circular grain embedded in a continuum of austenite that is assumed to remain untransformed. The model is characterized by the parameters δ denoting the grain diameter, the width B of the central laminate and the twin band width d. Each laminate is composed of a series of alternating Bain correspondence variants (BCV) highlighted by different shades of gray in Fig. 2a. The junction plane between the two laminates as well as all twin planes between Bain variants, which are perpendicular to the projection plane appear as lines in this view. The current model comprises three sections of twin-related martensite laminates, the central one including an angle of 125° with its neighbors. The transformation eigenstrain components for each Bain variant can be calculated in a coordinate system aligned with the projection plane. As an example the eigenstrains for BCV1 are given here: $\varepsilon_{T,11} = -0.039$, $\varepsilon_{T,22} = 0.076$, $\gamma_{T,12} = -0.105$. Note that also out-of-plane contributions of the transformation strain tensor are expected which will add to the total strain energy. In a plane stress model these additional energy contributions cannot be captured. A quantitative comparison with experimental data at this stage of the modeling work is therefore not yet possible. The finite element mesh has been arranged in such a way that it already contains all the characteristic features of the transformed geometry, i.e. twin planes always coincide with element edges. This guarantees sharp interfaces and captures jumps in the stress distribution. 6-node triangular elements with quadratic shape functions have been chosen, suitable for resolving the stress singularities at the corners of the interface sufficiently well. The triangular element shape allows enough flexibility to mesh the sometimes narrow and misshaped sections at the perimeter of the grain. The transforming grain is assumed to be embedded in an infinitely extended austenitic matrix. Realistically, the stress fields generated by the transformation will decay to zero far away from the boundary of the grain. It is thus admissible to place the grain in the center of a circular patch with a diameter of 10δ without having to cope with undesirable boundary effects at the perimeter of the finite element model. Relatively large elements can be used in the zones far away from the grain where no significant gradients have to be expected (see Fig. 2b). The transformation itself is simulated as anisotropic thermal expansion, the expansion coefficients thus representing the transformation eigenstrains calculated above.

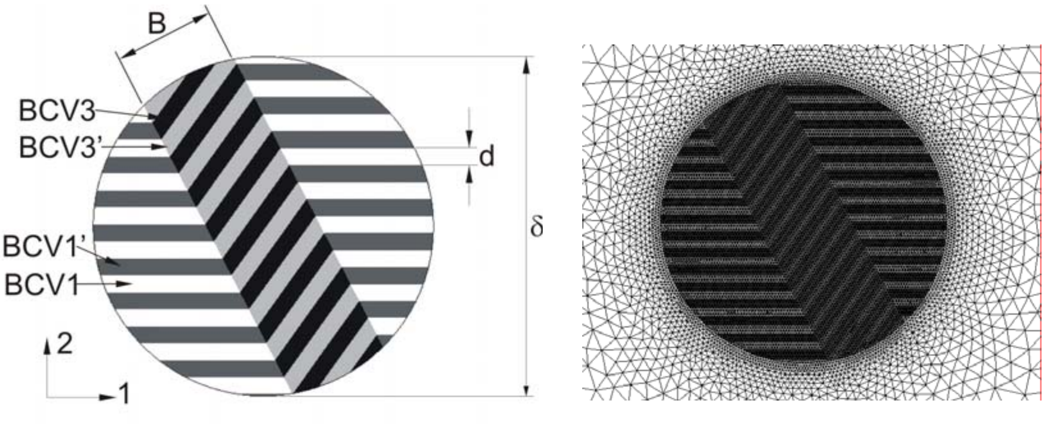

(a) (b)

Figure 2. (a) Geometrical parameters describing the herring-bone pattern of a fully transformed grain. The surrounding austenitic matrix is not displayed.(b) Detail of the finite element mesh in and around the grain.

As a direct result of the numerical calculations the strain energy input into the material can be worked out. A total energy balance, however, also requires taking into account the chemical interface energies at the twin planes as well as the grain boundary and the phase boundary between the two different martensite laminates. These contributions have to be added to the strain energy in a subsequent postprocessing step. For the specific magnitudes of the chemical surface energies the reader is referred to [7]. Given the transformation strains of the martensite variants the total energy introduced by the phase change depends on two geometric parameters, i.e. the fraction of each laminate defined by B/δ and the relative twin band width d/δ. An automated preprocessing procedure enables to create finite element models for various combinations of these parameters. The resulting total energy e_b per grain volume as a function of B/δ and d/δ is shown in Fig. 3a for δ =50nm and Fig. 3b for δ=100nm. These cases are also compared with a single laminate of BCV1 and BCV1', where the central section disappears. For the case of the smaller grain the energy minimum is found for B/δ=0.3 and d/δ = 0.05, i.e. d=2.5nm. This ratio d/δ shifts to lower values as the grain grows while the absolute magnitude of d slowly increases. For d=100nm the optimum twin band width d is at about 3.5nm. These values correspond well to the dimensions found in the micrographs depicted in Fig. 1. The energy consumption relative to the grain volume is higher in the case of the smaller grain making it more difficult for the grain to transform. For the two examples shown in Fig. 3 the herring-bone morphology consisting of three alternating laminates is energetically more favorable than its single-layered counterpart indicated by the dashed line with the white open markers. However, as the grain diameter tends to smaller values this energetic advantage decreases, i.e. the e_b-curve for the single laminate does not rise as rapidly with decreasing δ as the e_b-curves representing the herring-bone structure. Eventually, for small enough grains the single-layered pattern will prevail.

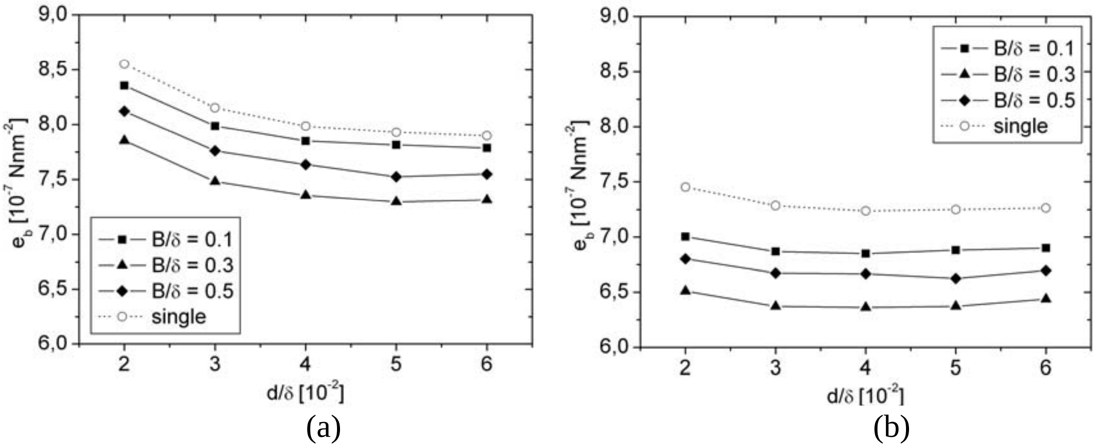

Figure 3. Total energy per grain volume as a function of the relative twin band width evaluated for (a) δ=50nm, and (b) δ=100nm.

3. Conclusions

The morphology of a NiTi nanograin is to a large extent determined by the total energy minimum after martensitic transformation. In terms of this energy a herring-bone pattern of two martensite laminates is compared with the case of a single laminate. For the herring-bone microstructure the width B of the central section as well as the twin band-width d has then been quantified for a given grain diameter δ. The calculated morphology expressed in terms of the ratios B/δ and d/δ is in good agreement with the experimental evidence.

References

[1] Waitz, T., Karnthaler, H.P., 2004. Martensitic transformation of NiTi nanocrystals embedded in an amorphous matrix," Acta Materialia 52, 5461-5469.

[2] Waitz, T., Kazykhanov, V., Karnthaler, H.P., 2004. Martensitic phase transformations in nanocrystalline NiTi studied by TEM. Acta Materialia 52, 137-147.

[3] Hane, K.F. and Shield, T.W., 1999. Microstructure in the cubic to monolinic transition in Titanium-Nickel shape memory alloys. Acta Materialia 47, 2603-2617.

[4] Ball, J.M., James, R.D., 1987. Fine phase mixtures as minimizers of energy. Archive for Rational Mechanics and Analysis 100, 13-52.

[5] Bhattacharya, K., 2003. Microstructure of Martensite. Why it forms and how it gives rise to the shape-memory effect. Oxford University Press, New York.

[6] Fischer, F.D., Schaden, T., Appel, F., Clemens, H., 2003. Mechanical twins, their development and growth. European Journal of Mechanics A22, 709-726.

[7] Waitz, T., Antretter, T., Fischer, F.D., Simha, N.K., Karnthaler, H.P., 2006. Size effects on the martensitic phase transformation of NiTi nanograins, to be published in J. Mech. Phys. Solids.

Multiscale and mesoscopic modeling and simulation of carbon nanotubes

Marino Arroyo

Departament de Matemàtica Aplicada III
Universitat Politècnica de Catalunya
C/ Jordi Girona 1-3, Barcelona 08034, Spain

ABSTRACT

We present theory to deductively construct continuum models for crystalline monolayers from atomistic models. Finite element calculations based on this theory for carbon nanotubes (CNTs) faithfully reproduce orders of magnitude more expensive atomistic calculations. This technique has allowed us to simulate thick multi-million atom MWCNTs, linking directly with experimental observations. The simulations have reproduced the observed rippling deformations of thick MWCNTs, revealing an anomalous nonlinear elastic response to bending and torsion. This is particularly relevant in the view of the number of CNT-based devices in which thick MWCNTs act as structural springs, since according to our predictions, they behave as nonlinear springs at moderate deformations. We propose a further level of model upscaling, by constructing mesoscopic beam models to describe thick MWCNTs, which encode the essential complexity arising from the multi-layer structure, the short-range atomistic interactions, and the van der Waals interactions. According to large-scale multiscale simulations, MWCNTs seen as elastic beams display a non-convex energy-curvature relation, which leads to phase transformations. Physically, one phase corresponds to the smooth bending of the structure, while the second phase corresponds to the rippled bending deformation. We have validated this simple model against faithful atomistic simulations, as well as available experimental data.

1. Introduction

Carbon nanotubes have sparkled intense research since their discovery, and show great potential for nano-devices, sensors and nano-structured materials. Their mechanical response plays a key role in many applications. Experimental observations as well as computer simulations have revealed a quite unique mechanical behavior. Despite being one of the stiffest and strongest materials in nature, carbon nanotubes display a remarkable flexibility and resilience to deformation modes other than uniaxial tension. This is due to their tendency to buckle in a reversible manner. A number of good experiments have probed the mechanics of nanotubes. Nevertheless, the difficulty of extracting reproducible quantitative data for such small structures makes of computer simulations a very valuable means of understanding nanotubes.

2. Modeling and simulation of carbon nanotubes

Atomistic descriptions are the model of choice for computer simulations of carbon nanotubes. *Ab initio* calculations allow us to simulate up to hundreds of atoms, while atomistic simulations with empirical potentials usually reach several million atoms. In order to simulate the mechanics of larger nanotubes, as well as to rationalize their mechanics, researchers have resorted to continuum mechanics. Despite the small size of these structures, continuum mechanics has proven very useful and applicable to a surprising extent.

Two drawbacks of most continuum mechanics models of carbon nanotubes routinely used in the literature are, on the one hand their phenomenological nature, and on the other hand the restriction to small deformations, despite nanotubes display very large elastic deformations. In [1] we presented a theory to construct finite deformation continuum mechanics models for curved lattices such as graphene, and applied this theory to carbon nanotubes. The key element is a kinematic rule relating the curved continuum strains and the discrete deformations in the spirit of the Cauchy-Born rule, the so-called Exponential Cauchy-Born rule (ECB). Salient features of this theory are that it results in a genuinely two-dimensional continuum for a two-dimensional lattice, and that the constitutive model is constructed explicitly in terms of the atomistic model of choice. In [2] the performance of this model was carefully tested against atomistic simulations for a number of benchmark problems.

3. Mechanics of thick multiwalled carbon nanotubes

The efficient and reliable computational method based on the ECB rule and finite elements allows us to study easily multi-million atom systems of thick multi-walled (MWCNTs) with models containing two orders of magnitude less degrees of freedom. These simulations contribute to the understanding of the mechanics of thick MWCNTs, currently serving as structural building blocks in an array of nano-scale devices [4,5]. Previously, these systems were analyzed qualitatively by simplified two-dimensional anisotropic elasticity models, macroscopic rubber scrolls and geometric scaling arguments, or phenomenological shell models. In [3], we presented reliable simulations based on realistic potentials, which revealed the 3D morphological structure of the experimentally observed rippling deformations analogous to the Yoshimura pattern.

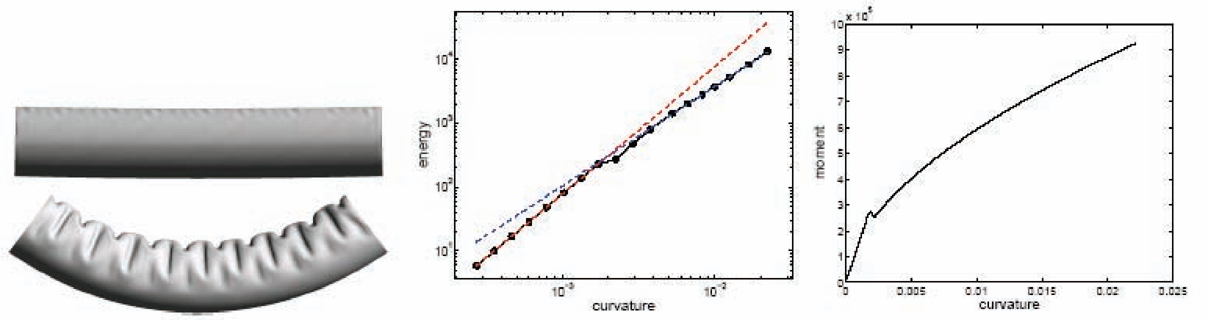

Figure 1. Anomalous elasticity of thick MWCNTs subjected to bending (here a 80 nm long 20-walled CNT).

But the most important result of this study is the identification of two distinct elastic regimes in the mechanical response of thick MWCNTs; initially, these systems behave harmonically, displaying a quadratic growth of the strain energy with deformation, which is followed by a nontrivial well-defined scaling of the energy. The initial harmonic regime is practically absent for thick MWCNTs, and the latter anomalous and genuinely nonlinear structural response dominates the mechanical behavior for moderate and large deformations, such as those encountered in oscillators and devices. The energetics in the anomalous regime follows E □ $deformation^a$, with $1 < a < 2$ and results from a complex interplay of in-plane energy relaxation with nonbonded and bending energy penalties. This response can be clearly observed in Fig. 1, where a 20-walled nanotube is considered. It is apparent form the figure that the harmonic regime previous to rippling only holds in a small neighborhood of the straight configuration. When plotted in a log–log scale, the energy evolution clearly displays two distinct regimes characterized by the slopes 2 (harmonic) and $a = 1.56$ (rippled). This results in a nonlinear moment–curvature relationship, and an elastic modulus that depends on deformation [6]. Simulations with larger tubes suggest that the larger the MWCNT is, the smaller the harmonic regime is and the larger the exponent a is. It should be stressed that all these phenomena are reversible, although a small hysteresis loop is observed upon unloading in the vicinity of the crossover region. Torsional rippling is also predicted by the simulations, which also display an anomalous elastic behavior. Unlike bending rippling, this behavior has not been reported in the literature, although some published images seem to suggest torsional rippling in the view of the simulations [6].

4. Phase-transforming beam models

Though useful and illuminating, the simulations described above are not practical from an engineering prospective for the design of devices or the interpretation of experimental observations. Indeed, each shell of the MWCNT must be explicitly modeled, as well as their interactions, with sufficient resolution to describe the local buckles. The reduction of two orders of magnitude in the number of degrees of freedom as compared to atomistic simulations is not sufficient to avoid parallel computations when long tubes with tens of walls are involved (this is often the case in devices). The prevalent approach, for instance when interpreting measurements, is to assume that MWCNTs behave as Euler-Bernoulli elastic beams. Due to the above-mentioned anomalous elasticity of MWCNTs, this oversimplification can result in gross errors in measured data.

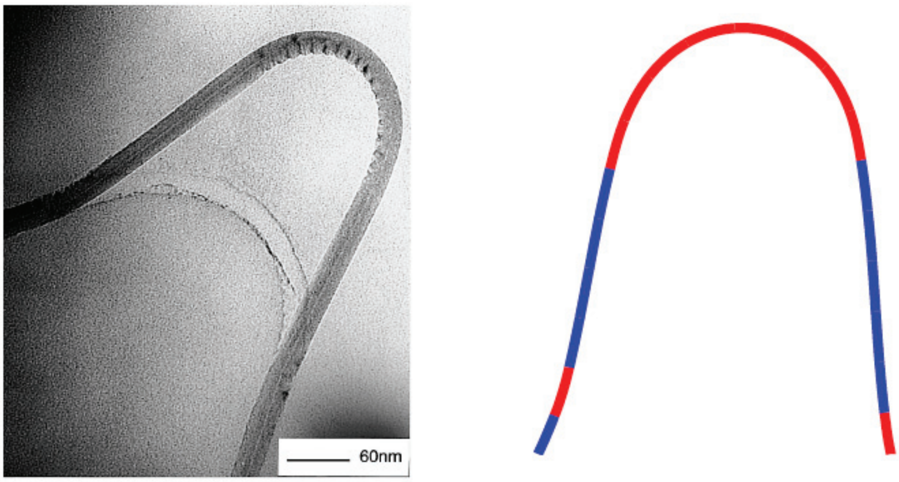

Figure 2. Experimental observation of a MWCNT exhibiting rippled and smooth phases [7], and a corresponding simulation of the beam model with non-convex energy (red: rippled phase, blue: smooth phase).

The simulations presented above suggest a simple reduced model capturing the essential nonlinear mechanics of thick MWCNTs. Indeed, the robust power law for the strain energy as a function of curvature once rippling has occurred, together with the principle of energy minimization, suggests the following constitutive law for a beam deforming in 2D:

$$W(\lambda,\kappa)= W_{stretch}(\lambda) + \min \{C_1 \kappa^2; C_2 \kappa^a\} \qquad (1)$$

In the above equation, λ denotes the stretch of the beam and κ its curvature. The stretch potential is typically very stiff and the beam can be considered as an inextensible elastica. Note carefully that the above bending energy contribution is non convex. When subjected to bending moment, the total energy displays two energy wells, and thus we can anticipate that this energy will lead to phase coexistence and microstructure formation. The first energy well corresponds to smooth bending deformations while the second well entails the rippling instability. Simple simulations show that indeed this is the case, and a stressed microstructure can be observed in Fig. 2. This model is reminiscent of that presented and analyzed in [8].

5. Outlook

Further study of this simple model, particularly with regards to the dynamics (relevant in oscillators) and to the dissipation and hysteresis, will be the object of future investigations. It is expected that such tractable analytical models, which nevertheless retain the essential mechanics, can improve the interpretation of experiments. Further understanding beyond simulations of the complex nonlinearly elastic rippling response is needed. For instance, the systematic dependence of the exponent a on the deformation mode or the number of walls is not clear.

Acknowledgements

The author acknowledges the support of the European Commission through grant Marie Curie-IRG (Proposal N° 029178).

References

[1] M. Arroyo and T. Belytschko, “An atomistic-based finite deformation membrane for single layer crystalline films”, *Journal of the Mechanics and Physics of Solids*, 50:1941-1977 (2002).

[2] M. Arroyo and T. Belytschko, “Finite element analysis of the nonlinear mechanics of carbon nanotubes”, *International Journal for Numerical Methods in Engineering*, 59:419-456 (2004).

[3] M. Arroyo and T. Belytschko, “Nonlinear mechanical response and rippling of thick multi-walled carbon nanotubes”, *Physical Review Letters*, 91:215505 (2003).

[4] Papadakis, S.J., Hall, A.R., Williams, P.A., Vicci, L., Falvo, M.R., Superfine, R., and Washburn, S., “Resonant oscillators with carbon-nanotube torsion springs”, *Physical Review Letters*, 93:146101 (2004).

[5] Poncharal, P., Wang, Z.L., Ugarte, D., and de Heer, W.A., “Electrostatic deflections and electro mechanical resonances of carbon nanotubes”, *Science*, 283(5407):1513–1516 (1999).

[6] M. Arroyo and T. Belytschko, “Continuum mechanics modeling and simulation of carbon nanotubes”, *Meccanica*, 40:455-469 (2005).

[7] Lourie, O., Cox, D.M., and Wagner H.D., “Buckling and collapse of embedded carbon nanotubes”, *Physical Review Letters*, 81(8) (1998).

[8] R.D. James, “The equilibrium and post-buckling behavior of an elastic curve governed by a non-convex energy”, *Journal of Elasticity*, 11(3): 239 – 269 (1981).

Fully Anisotropic 3D Dislocation Dynamics Study of Deformation Behavior in B2 Intermetallic Systems

Q. Chen and *S.B. Biner*

Materials and Engineering Physics, Ames Laboratory (US DOE)
Iowa State University, Ames, IA 50011 USA

ABSTRACT

In this study, the origin of large ductility that is seen in recently discovered rare-earth intermetallic compounds: YCu, YAg and YZn is explored by using fully anisotropic 3D discrete dislocation dynamics simulations. The stability of prefect dislocations, Frank-Read source formation, interaction energy of kink pairs, strength of junctions and dipoles are evaluated and compared to those seen for the common B2 type intermetallics, NiAl and Fe-25Al. The results clearly indicate the role and the importance of elastic anisotropy on the evolution of dislocation microstructures and overall hardening behavior in these systems.

1.Introduction

Most intermetallic alloys exhibit very limited ductility at room temperatures and their brittle behavior, in both single and polycrystalline forms, has been extensively investigated [1-2]. A new class of highly ordered, ductile intermetallic systems has been discovered recently [3]. These alloys have the B2 structure and are based on a rare-earth element and a late transition metal or an early p-element. Apparently, there are 120 such alloys, most of these have not been studied, but at least 12 such compounds have been found to possess significantly high ductility and fracture toughness when tested at room temperature and in air [3].

2.Computational Method and Results

The elastic energy, *E*, per unit length of a straight dislocation in a linearly anisotropic elastic crystal is given by:

$$E = \frac{K\,b^2}{4\pi} \ln\left(\frac{R}{r_0}\right) \qquad (1)$$

where *K* is the energy factor for the dislocation and is a function of both the elastic constants of the anisotropic crystal and the orientation of the dislocation line with its Burgers vector; *R* is the outer radius of integration; and r_0 is the dislocation core radius, which is of the order of b, the magnitude of the Burgers vector. The line tension T_L per unit length of a straight dislocation depends on the energy factor *K* and its second derivative as

$$T_L = \frac{b^2}{4\pi} \ln\left(\frac{R}{r_0}\right)\left(K(\theta) + \frac{\partial^2 K(\theta)}{\partial \theta^2}\right) \qquad (2)$$

If the logarithmic term in Eqn.1 is assumed to be constant for all dislocation orientations, the *1/K* plots are equivalent to the inverse Wulff plots (1/*E*). There are two criteria for dislocation line instability: First, the concavity of the inverse Wulff plot. Second, the negative line tension, which is a sufficient but not necessary condition for instability. All straight dislocations satisfying these conditions will relax their energy by transforming into V-shaped bends or zigzagged bends.

In discrete dislocation dynamics simulations, the forces per unit length causing the mobility of the dislocations is obtained from Peach-Koehler formula:

$$\vec{F} = ((\sigma^{D} + \sigma^{A}) \bullet \vec{b}) \times \vec{t} + \vec{F}_{self} \tag{3}$$

where σ^{D} is the sum of the stress tensor from other remote dislocation segments, σ^{A} is the applied stress tensor, b is the Burgers vector and t is the unit tangent vector of the dislocation line and F_{self} is force arising from the line tension of the dislocation segment. In the evaluation of σ^{D}, the elastic distortion tensor associated with dislocation line segment can be expressed as [4]

$$u_{i,j}(x) = \varepsilon_{jnk} C_{pqmn} b_m \int_L G_{ip.q}(\vec{x} - \vec{x}') v_k \, dl(\vec{x}') \tag{4}$$

where ε_{jnk} is the permutation tensor, C_{pqmn} is the elastic stiffness tensor, b_m is the Burgers vector, v_k is the unit tangent vector and dl is the dislocation line element. The $G_{ip,q}$ term is the derivatives of the Green's function. For an isotropic solid, the Eqn 1,2 and 4 have all closed form analytical expressions. For general anisotropy, the evaluation of these equations requires numerical approaches either solving sextic algebraic equations [5] or integral formalism [6]. In our study we adopted the integral formalism. The heavy computational burden for the evaluation of multiple integrals associated with the Eqn 1,2 and 4 can be reduced to manageable level by expressing them in the form of preprocessed look-up tables of which the details will be given in ref. [7].

The elastic constants of the alloys at room temperature used in our analyses are summarized in Tab 1, together with the anisotropy factors $A=2C_{44}/(C_{11}-C_{12})$ and $H=2C_{44}-C_{11}+C_{12}$. Stability of the dislocations in intermetallics plays an important role in deformation mechanisms for yielding and work hardening. Fig.1 compares the inverse energy (1/K) plots for $(1\bar{1}0)[001]$ slip.

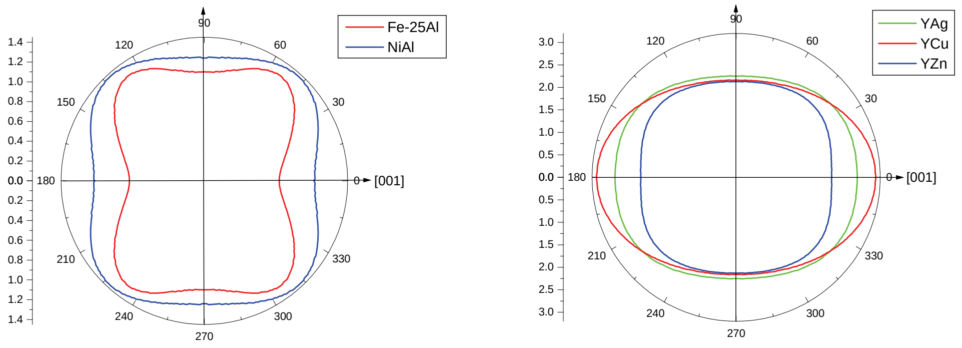

a) b)

Figure 1. (1/K) plot for $(1\bar{1}0)[001]$ glide loop. a) Data for NiAl and Fe-25Al b) Data for YCu, YAg and YZn.

As can be seen, Fe-25Al exhibited two ranges of instability, one centering on screw (θ=0°) and the other centering on edge dislocations (θ=90°). As for NiAl, the instability is only centered on the screw dislocations; no instability is present near the edge dislocations. In contrast, the dislocations with this slip system are all stable in YCu, YAg and YZn as can be seen from the convex shape of (1/*K*) plots in Fig.1b; in addition, for all the θ values their line tension is positive.

Fig.2 summarizes the evolution of dislocation loops from a Frank-Read source in Fe-25Al, NiAl and YCu. The initial length of pure screw dislocation segments ($b = \frac{1}{2}[111]$) was $1000\sqrt{3}|b|$ and located on the $(1\bar{1}0)$ glide plane. Applied uniaxial stress was in [100] direction.

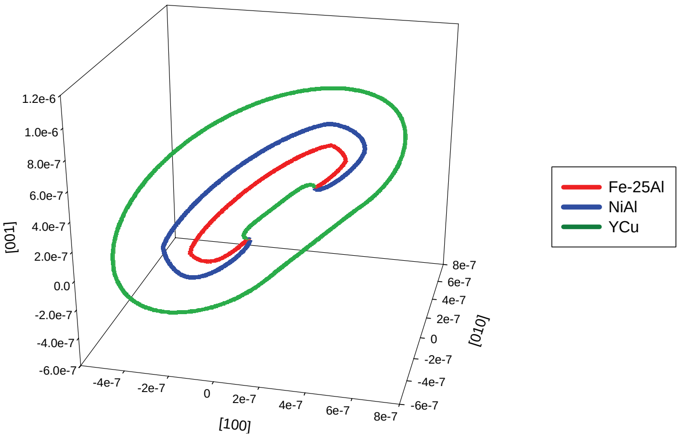

Figure.2 Evolution of an F-R source under applied stress

From Fig. 2, it can be clearly seen that dislocation segment has the greater resistance to shear deformation with higher anisotropic ratio. Under the same applied force, the dislocation segment in YCu bows out furthest and has formed the second dislocation loop, whereas the one in Fe-25Al moved very short distance.

Next, we summarize the behavior of the junctions in these systems. When two attractive dislocations with nonparallel Burgers vector in intersecting planes approach each other, the junction forms once the force between them reaches a critical value. In most cases, junctions are immobile and they restrict the further motion of dislocations thus enhancing the work hardening and limiting the ductility. By using 3D anisotropic dislocation dynamics, we evaluated the formation of junctions under zero applied stress first. After their formation, their strengths were determined as the applied stress values required for their break-up. Possible combinations of primary and secondary slip systems for junction reactions in bcc crystal system are given in [8]. Fig.3 shows the equilibrium morphologies of the junctions forming at slip systems $[111](1\bar{1}0)\,\&\,[1\bar{1}\bar{1}](211)$ in these alloys. In these simulations, the initial angles between the dislocations arms and the intersection line $[\bar{1}\bar{1}3]$ were -25.23^{o} and 31.48^{o} respectively. Both dislocations arms had the same length $100\sqrt{2}b$ and the length of the segments forming the dislocation lines was taken as 5*b*.

In Fig.3, the occurrence of the kinks in dislocation arms in Fe-25Al system can be clearly seen from the figure due to mentioned instabilities associated with the line tension. Also the evolution of the larger junction lengths with increasing anisotropy (Tab.1) can be depicted from the figure. When an applied stress is introduced, the four arms of the junction bow out as small Frank-Read sources and the junction unzips. The break-up stress values for the junctions shown in Fig.3 were (in MPa) 4000, 1800, 1040, 1020,1135 for Fe-25Al, Ni-Al, YAg, YCu and YZn respectively.

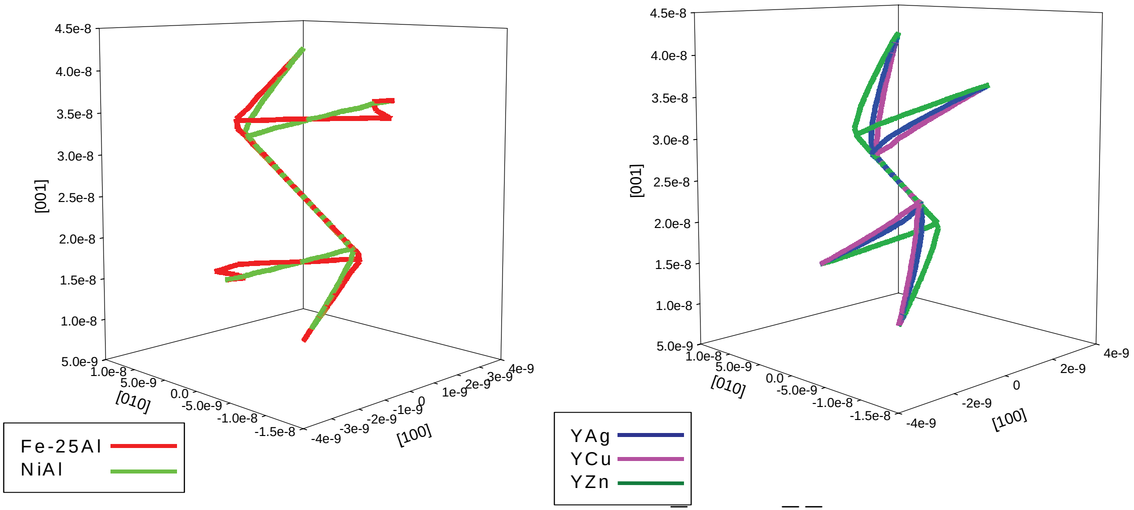

Figure.3 Junction configurations for slip systems $[111](1\bar{1}0)$ & $[1\bar{1}\bar{1}](211)$ in five B2 alloys

3. Conclusions:

1. The convex shape of the inverse energy plots and positive line tension show that the elastic anisotropy is too small to cause any instability of ordinary dislocations in YCu, YAg and YZn.
2. Strength of junctions in YCu, YAg and YZn is much smaller in comparison to Ni-Al and Fe-25Al due to smaller elastic anisotropy.

Acknowledgement:

This work was performed for the United States Department of Energy by Iowa State University under contract W-7405-Eng-82. This research was supported by the Director of Energy Research, Office of Basic Sciences.

Table 1 Elastic constants and anisotropic factors of five B2 alloys

	C_{11} (GPa)	C_{12} (GPa)	C_{44} (GPa)	A	H (GPa)
Fe-25Al	171.0	131.0	132.0	6.6	224.0
NiAl	170.3	115.4	89.7	3.27	124.5
YAg	102.4	54.0	37.2	1.54	26.0
YCu	113.4	48.4	32.3	0.99	-0.4
YZn	94.7	47.8	47.2	2.01	47.0

References:

[1] X. Shi, S. Mahajan, T.M. Pollock and V.S. Arunachalam, *Phil. Mag. A*, **79**, 1555 (1999).
[2] C.T. Liu, J. Stringer, J.N. Mundy, L.L. Horton, P. Angelini, *Intermetallics*, **5**, 579 (1997).
[3] K. Gschneidner Jr., A. Russell, A. Pecharsky, J.R. Morris, Z. Zhang, T. Lograsso, D. Hsu, C.H. C. Lo, Y. Ye, A. Slager and D. Kesse, *Nature Mat*. **2**, 587 (2003).
[4] T. Mura, “Micromechanics of defects in solids”, 2nd ed. (Martinus Nijhoff, Dorecht 1987).
[5] A.N. Stroh, *Phil. Mag*, **3,** 625 (1958).
[6] D.M. Barnett, *Phys. Stat. Sol.(b)*, **49**, 741 (1972).
[7] Q. Chen and S.B. Biner *(to be published*).
[8] W. Puschl, *Phys. Stat. Sol.(a)*, **90**, 191 (1985).

Atomistic Studies of Stimulated Dislocation Nucleation at Crack Fronts

Erik Bitzek

Institut fuer Zuverlaessigkeit von Bauteilen und Systemen, Universitaet Karlsruhe (TH), Kaiserstrasse 12, 76131 Karlsruhe, Germany

One of the great unknowns in the description of semi-brittle fracture is the origin of the dislocations near the crack tip. Preexisting dislocations are known to influence the low temperature fracture toughness and the brittle-to-ductile-transition (BDT) dramatically (see [1,2,3] and references therein). Experiments on single crystalline silicon show that dislocation nucleation can be a highly inhomogeneous process if preexisting defects are present at the crack front. A single dislocation intersecting the crack front can stimulate the emission of other dislocations in an avalanche-type multiplication process [1]. The detailed mechanism of this stimulated emission and multiplication of dislocations at the crack tip are still largely unexplored and the subject of this paper.

We present large scale, three dimensional atomistic fracture simulations using a [001](110) mode I crack in nickel. The interaction of different dislocations with sharp and blunted static ($K < K_{Ic}$) cracks are studied using standard molecular dynamics techniques.

The events during the interaction of an impinging dislocation with the crack of course depend on the character and glide plane of the dislocation. Frequently observed processes include the stimulated emission of full dislocation loops and cross slip of the incoming dislocation. Sharp cracks react on the dislocation stress field by partial crack advance or closure. The thus curved crack front can lead to the emission of dislocations on otherwise inactive glide planes.

The simulation results are analyzed with respect to the driving forces on the dislocations caused by the crack tip stress field and compared with experiments. Implications for mesoscopic modeling of semi-brittle fracture and the brittle-to-ductile transition are discussed.

[1] C. Scandian et al., phys. stat. sol. (a) 171, p.67 (1999)

[2] B.J. Gally and A.S. Argon, Phil. Mag. A 81, p.600 (2001)

[3] P. Gumbsch, et al., Science 282 (1998) 1293-1295.

Interaction of dislocations with grain boundaries in a 3D-nanocrystalline network

<u>Christian Brandl</u>[1], P. M. Derlet[1], H. van Swygenhoven[1]

[1]Paul Scherrer Institute, WHGA/348, 5232 Villigen, Switzerland

In order to incorporate grain boundary effects in mesoscopic models, criteria for dislocation absorption and transmission with grain boundaries have to be formulated. This poster will report on the atomistic details of some mechanisms that have been observed during molecular dynamics computer simulations of deformation of nanocrystalline Al. Particular emphasis will be given to the changes in the grain boundary structure upon emission of a dislocation or upon absorption of a dislocation and how these affect (1) the further ability of the dislocation to act as source and sink for further dislocation activity in the same grain and (2) the initiation of dislocation activity in a neighbouring grain by means of dislocation transmission or the activation of new sources.

Multiparadigm modeling of dynamic fracture of silicon: Crack speeds and instabilities

Markus J. Buehler[1,*], **Harvey Tang**[2], **Janet Rye**[3], **Adri van Duin**[4], **William A. Goddard**[4]

[1] **Department of Civil and Environmental Engineering, Massachusetts Institute of Technology, Cambridge, MA, 02139, USA**
[2] **Department of Aeronautical Engineering, Massachusetts Institute of Technology, Cambridge, MA, 02139, USA**
[3] **Department of Materials Science and Engineering, Massachusetts Institute of Technology, Cambridge, MA, 02139, USA**
[4] **Materials and Process Simulation Center, California Institute of Technology, Pasadena, CA, 91125, CA, USA**

*** Corresponding author, email: mbuehler@MIT.EDU**

ABSTRACT

We report a study of dynamic cracking in a silicon single crystal in which the ReaxFF reactive force field is used for ~3,000 atoms near the crack tip while the other 100,000 atoms of the model system are described with a simple nonreactive force field. The ReaxFF is completely derived from quantum mechanical calculations of simple silicon systems without any empirical parameters. This model has been successfully used to study crack dynamics in silicon, capable of reproducing key experimental results such as orientation dependence of crack dynamics (Buehler *et al.*, *Phys. Rev. Lett.*, 2006). In this article, we focus on crack speeds as a function of loading and crack propagation mechanisms. We find that the steady state crack speed does not increase continuously with applied load, but instead jumps to a finite value immediately after the critical load, followed by a regime of slow increase. Our results quantitatively reproduce experimental observations of crack speeds during fracture in silicon along the (111) planes.

1. Introduction

Brittle fracture is characterized by breaking of atomic bonds leading to formation of two new materials surfaces. Most existing atomistic models of fracture assume an empirical relationship between bond stretch and force. However, breaking of bonds in real materials is an extremely complicated process that could previously only be captured with sufficient accuracy only by using quantum mechanical (QM) methods, which are limited to ~100 atoms. Here we present a new theoretical concept based on building a multi-scale simulation model completely derived from QM principles, while being computationally efficient and capable of treating thousands of atoms with QM accuracy. Fracture of silicon has received tremendous attention due to its complexity of bond breaking and due to interesting failure dynamics observed experimentally [1-5]. These experimental efforts led to critical insight into deformation modes, such as the mirror-mist-hackle transition and orientational dependence of crack dynamics in silicon single crystals [2].

Atomistic modeling fracture of silicon has been the subject of several studies using empirical force fields [5-9]. In contrast to many metals, where fracture and deformation can be described reasonably well using embedded atom (EAM) potentials [10-12], a proper

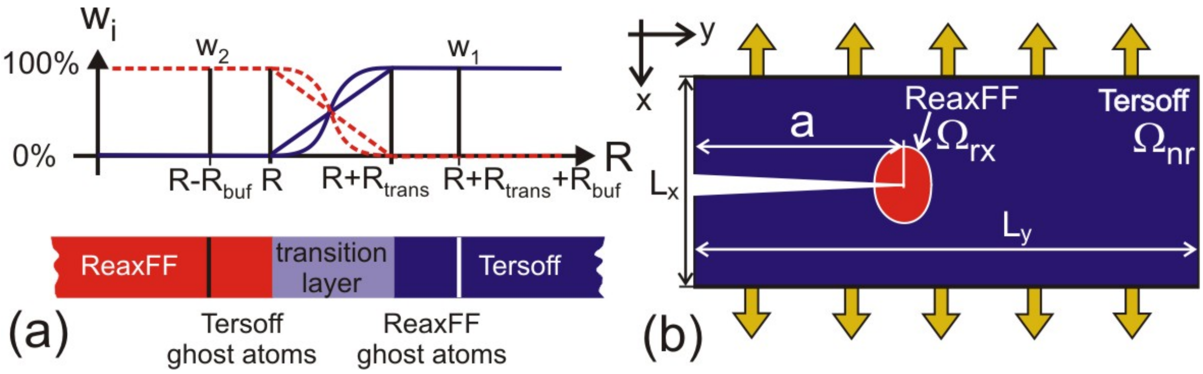

Figure 1: Subplot (a): The interpolation method for defining a mixed Hamiltonian in the transition region between two different paradigms, as implemented in the CMDF framework.As an alternative to the linear interpolation, we have also implemented smooth interpolation function based on a sinusoidal function. This enables using slightly smaller handshake regions thus increasing the computational efficiency. Subplot (b): Geometry used for simulating mode I fracture in silicon. The (110) crack surface system contains 28,800 atoms with L_x≈230Å, and L_y≈460Å. The (111) crack surface system contains 86,400 atoms with L_x≈400Å, and L_y≈1130Å. At the tip of the crack, up to 3,000 atoms are modeled with ReaxFF.

description of fracture in silicon has proved to be far more difficult, requiring a more accurate treatment of the atomicinteractions. There have been several previous attempts to describe fracture of silicon using atomistic methods. Early attempts to model fracture in Si used Tersoff's classical potential [13] and similar formulations such as the Stillinger-Weber [14] or the EDIP potential [8]. These attempts failed due to an incorrect description of the bond breaking process. Baskes and coworkers used their modified EAM formulation (MEAM) to describe crack motion in silicon [9] and to investigate the critical load for fracture initiation. However, the MEAM formulation cannot describe bond formation and breaking of silicon with other elements such as oxygen.

It has become clear that in order to obtain an accurate description of the dynamics of fracture of materials, the accuracy of QM for atoms near the propagating crack tip is necessary to describe the very large potentially plastic strains as chemical bonds are broken while coupling this to the more gradual near elastic strains over much larger regions. This has been successfully demonstrated in earlier work for example in the MAAD approach [6] by coupling QM regions to empirical potentials. However, for an adequate description of bond breaking in Si, it is necessary to include ~3,000 atoms in the reactive region, which has not been possible.

Here we present the results for an alternative approach utilizing the ReaxFF reactive force field developed to reproduce the barriers and structures for reactive processes from QM, but at a computational cost many orders of magnitude smaller [15]. The challenge of modeling the physics of fracture is that bond-breaking processes must be simulated while allowing the heat generated to be dissipated properly to the remaining system and while modeling the flux of energy towards a moving crack tip. Time scales of microseconds to milliseconds may be needed to follow the crack propagation across grains to various surfaces. Such calculations have not previously been possible. Here we describe the first simulation treating the silicon system with this level of accuracy.

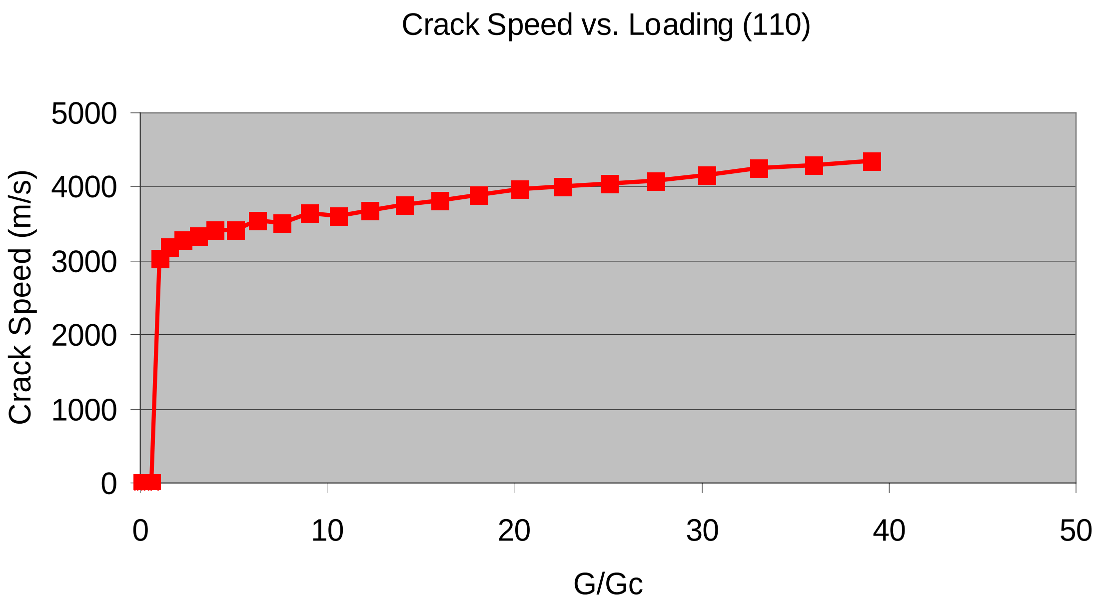

Figure 2: Crack speed as a function of reduced load, for a crack in the (110) orientation. For small loads ($G/G_C < 1$), the crack speed is zero. Above $G/G_C > 1$ we observe a finite crack speed, with a sudden jump to approximately 3,000 m/s. Then the crack speed displays a steady, linearly increasing, trend with strain load. The average limiting crack speed is measured while the crack travels in the region 200 Å < y < 400 Å (sufficiently far away from the boundary). The crack speed at large loading approaches approximately 4,200 m/s.

We use a hybrid simulation technique in which the ReaxFF reactive potential for silicon [16, 17] is used for a modest region of a few thousand atoms close to the crack tip while a computationally inexpensive but non-reactive Tersoff potential is used to describe the other 100,000 more distant atoms needed to include their elastic constraints on the propagating tip. Tersoff-type potential and ReaxFF lead to similar materials behavior (equation of state) for small strains, but deviate strongly at large strains. The fact that both descriptions overlap for small strains enable a smooth handshake between the two methods.

2. Computational method: Hybrid ReaxFF-Tersoff model

The Computational Materials Design Facility (CMDF) is a Python [18] based simulation framework allowing multi-paradigm multi-scale simulations of complex materials phenomena operating on disparate length- and time scales. Individual computational engines are wrapped using the “Simplified Wrapper and Interface Generator” (SWIG) for rapid integration of low-level codes with scripting languages. The CMDF framework enables the combination of ReaxFF to capture the QM description of reactions with classical non-reactive potentials to describe nonreacting regions providing the means for describing many complex materials failure processes as reported herein. This is the main focus of this paper.

To simulate the atoms around the crack tip we employ ReaxFF [16]. As described in [17], this potential has been tested against QM for a wide range of processes [19], including Si-Si bond breaking in H3Si-SiH3 and Si=Si bond breaking in $H_2Si=SiH_2$, equations of state for 4-coordinate silicon (diamond-configurations) and 6-coordinate silicon phases **β-t**in), and simple cubic crystal. This force field is also capable of treating interactions of Si with O and H. We recently added the stability and equation of state of a 5-coordinate Si-condensed phase to the Si training set, and we re-evaluated the Si-Si bond and Si-Si-Si angle parameters to

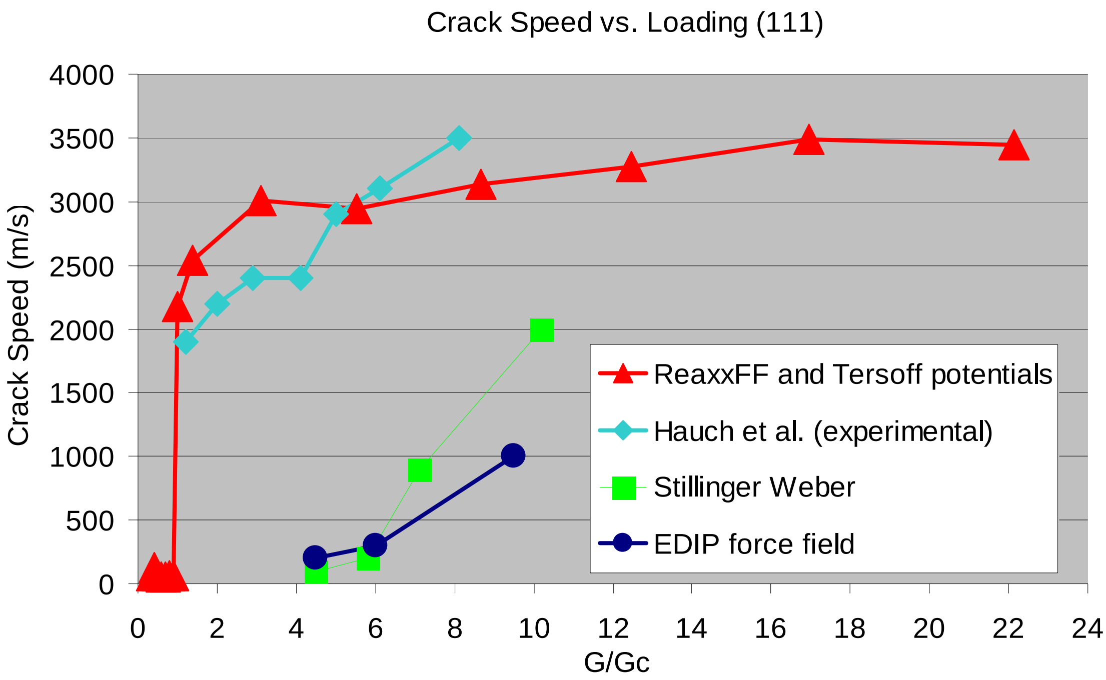

Figure 3: Crack speed as a function of reduced load, for a crack in the (111) orientation. For small loads ($G/G_C < 1$), the crack speed is zero. Above $G/G_C > 1$ we observe a finite crack speed, with a sudden jump to approximately 2,000 m/s. Then the crack speed displays a steady, linearly increasing, trend with strain load, approaching approximately 3,500 m/s. The average limiting crack speed is measured while the crack travels in the region 250 Å < y < 400 Å (sufficiently far away from the boundaries). At the intermediate values around $G/G_C \approx 1$, the crack does not propagate through the entire slab. When stable crack propagation is observed, the average crack speed approaches the initial velocity of approximately 2,000 m/s. Our results show a quantitative correlation with the experimental results obtained by Hauch and coworkers [20] (representative data plotted in the figure). The plot also contains data obtained with the Stillinger-Weber force field and the EDIP force field (data taken from [20]); these models fail to reproduce the experimental behavior.

improve the fit to the energy and equation of state of this phase. All parameters are completely derived from QM calculations. Because of the complexity of the mathematical expressions describing the partial bond orders, energies, and charges, ReaxFF is 1-2 orders of magnitudes more expensive than the Tersoff potential but several orders of magnitude faster than QM.

We use a simple general approach to describe the transition region between the two paradigms ReaxFF and Tersoff. The role of the handshake regions is to ensure that the correct boundary conditions are applied to each side, and that each side senses proper continuation in distribution or density and forces. Figure 1 illustrates the approach. The transition region is described by two parameters, R_{trans} for the width of the transition region, and R_{buf} for the width of the ghost atom region. In bridging such distinct computational engines we find it useful to use spatially varying weights w_i to determine the weighting of the force and energy contribution from different simulation engines. Every computational engine i has a specific weight w_i associated with it. The N weights always add up to one, as

$$\sum_{i=1..N} w_i = 1. \tag{1}$$

The force on each atom is then given by the weighted sum of all force contributions of each method,

$$F = \sum_{i=1..N} w_i F_i \,. \tag{2}$$

Different simulation regimes are coupled to one another by smoothly interpolating between different engines by using smoothly varying weighting functions. The width of the transition region R_{trans} depends on the nature of the system, but it should generally be larger than the typical atomic distance in a lattice or in an organic molecule (here we choose R_{trans} =6 Å). The width of the buffer layer is R_{buf} =5 Å.

The size of the reactive region is based on the strain energy density of each atom. All atoms with a strain energy larger than -3.5 eV are embedded in a cylindrical reactive region of 10 Å. The union of all those regions yields the total reactive region. When oxygen atoms are present in the system, a similar procedure is applied and in addition to the criterion based on the strain energy density, each oxygen atom is embedded in a cylindrical reactive region of 10 Å. We update the calculation regimes every 10 integration steps.

Figure 2 depicts our atomistic model. We consider a perfect crystal with an initial crack of length *a* serving as the failure initiation point. We strain the slab with strain in mode I prior to simulation as done in . The boundaries are held fixed during the simulation so that the stress in the material can only be relieved by crack propagation. The crack starts to nucleate shortly after the simulation is started.

3. Simulation results

The main objective of this paper is to perform a systematic study of the steady-state crack speed as a function of the applied load. Figure 2 plots the crack speed as a function of G / G_C, for a crack in the (110) orientation. Note that G_C is the critical energy release rate at the onset of fracture. We observe a lattice-trapping effect, similar as seen in experimental studies [4] and discussed in computational modeling recently [20]. Figure 3 plots the results obtained for the (111) orientation. This is the identical orientation as used in experiment and computational studies. Our hybrid model is capable of reproducing the experimental results quite accurately, showing some quantitative agreement. In the studies shown in Figures 2 and 3, the load applied to the system is held constant during the simulation.

Figure 4 shows the results for slowly increasing load (strain rate 0.0005% per integration step). Figure 4(a) shows the crack speed as a function of iteration number, including some snapshots of crack tip mechanisms and bond breaking events. Figure 4(b) shows some snapshot of the system as the crack propagates.

4. Discussion and conclusion

We have presented a new numerical method integrating the ReaxFF and Tersoff force fields to allow a physics based description of the fracture mechanics of silicon. Our new scheme represents a new multi-scale approach of coupling the QM scale of chemistry and bond breaking and formation with the scale of mechanics of materials. Our method is completely based on first-principles, with *no* empirical parameters used for fitting of ReaxFF for silicon. Our studies suggest that there exist lattice trapping effects that lead to a discretization of accessible crack speeds in silicon, clearly corroborating earlier experimental results (Figures 2 and 3). In contrast to previous attempts of modeling this experimental phenomenon with empirical potentials such as EDIP or Stillinger-Weber, our new hybrid model reproduces experimental results, at a fraction of the computational cost of QM based methods. It is remarkable that our model is capable of even reproducing experimental results quantitatively (see Figure 4), without any parameter fitting. Our theoretical results further provide insight into the crack-tip mechanisms during fracture initiation, indicating formation of a 5-7 membered Si ring (see inlay, Figure 4).

Since ReaxFF is capable of describing a wide heterogeneous range of materials, our approach provides a practical means to studying the coupling of complex chemical reactions to mechanical properties. Our hybrid method could enable studies of stress corrosion processes and other degradation and aging mechanisms.

5. Acknowledgements

HT and JR acknowledge support from MIT’s UROP program m. MJB acknowledges support from the MIT’s CEE department. We thank Dr. C. Schwartz and S. Wax of DARPA for encouraging this development by funding first a special CMDF project and then the CMDF part of the DARPA-PROM project. Additional funding for this project was provided by DOE-ASC and NSF-ITR.

6. References

1. Deegan, R.D., et al., *Wavy and rough cracks in silicon.* Phys. Rev. E, 2003. **67**(6): p. 066209.
2. Cramer, T., A. Wanner, and P. Gumbsch, *Energy dissipation and path instabilities in dynamic fracture of silicon single crystals.* Phys. Rev. Lett., 2000. **85**: p. 788-791.
3. Cramer, T., A. Wanner, and P. Gumbsch, *Crack Velocities during Dynamic Fracture of Glass and Single Crystalline Silicon.* Phys. Status Solidi A, 1997. **164**: p. R5.
4. Hauch, J.A., et al., *Dynamic fracture in Single Crystal Silicon.* Phys. Rev. Lett., 1999. **82**: p. 3823-2826.
5. Holland, D. and M. Marder, *Ideal brittle fracture of silicon studied with molecular dynamics.* Phys. Rev. Lett., 1998. **80**(4): p. 746.
6. Abraham, F.F., et al., *Spanning the length scales in dynamic simulation.* Computers in Physics, 1998. **12**(6): p. 538-546.
7. Bailey, N.P. and J.P. Sethna, *Macroscopic measure of the cohesive length scale: Fracture of notched single-crystal silicon.* Phys. Rev. B, 2003. **68**(20): p. 205204.
8. Bazant, M.Z., E. Kaxiras, and J.F. Justo, *Environment-Dependent Interatomic Potential for bulk silicon.* Physical Review B-Condensed Matter, 1997. **56**: p. 8542.
9. Swadener, J.G., M.I. Baskes, and M. Nastasi, *Molecular Dynamics Simulation of Brittle Fracture in Silicon.* Phys. Rev. Lett., 2002. **89**(8): p. 085503.
10. Baskes, M.I., *Embedded-atom method: Derivation and application to impurities, surfaces and other defects in metals.* Phys. Rev. B, 1984. **29**(12): p. 6443-6543.
11. Baskes, M.I., *Embedded Atom Method Atomistic Calculations Of The Dynamic Interaction Of An Edge Dislocation In Nickel With Helium Clusters.* Journal Of Metals, 1988. **40**(11): p. 123-123.
12. Finnis, M.W. and J.E. Sinclair, *A simple empirical N-body potential for transition metals.* Phil. Mag. A, 1984. **50**: p. 45-55.
13. Tersoff, J., *Empirical interatomic potentials for carbon, with applications to amorphous carbon.* Phys. Rev. Lett., 1988. **61**(25): p. 2879-2883.

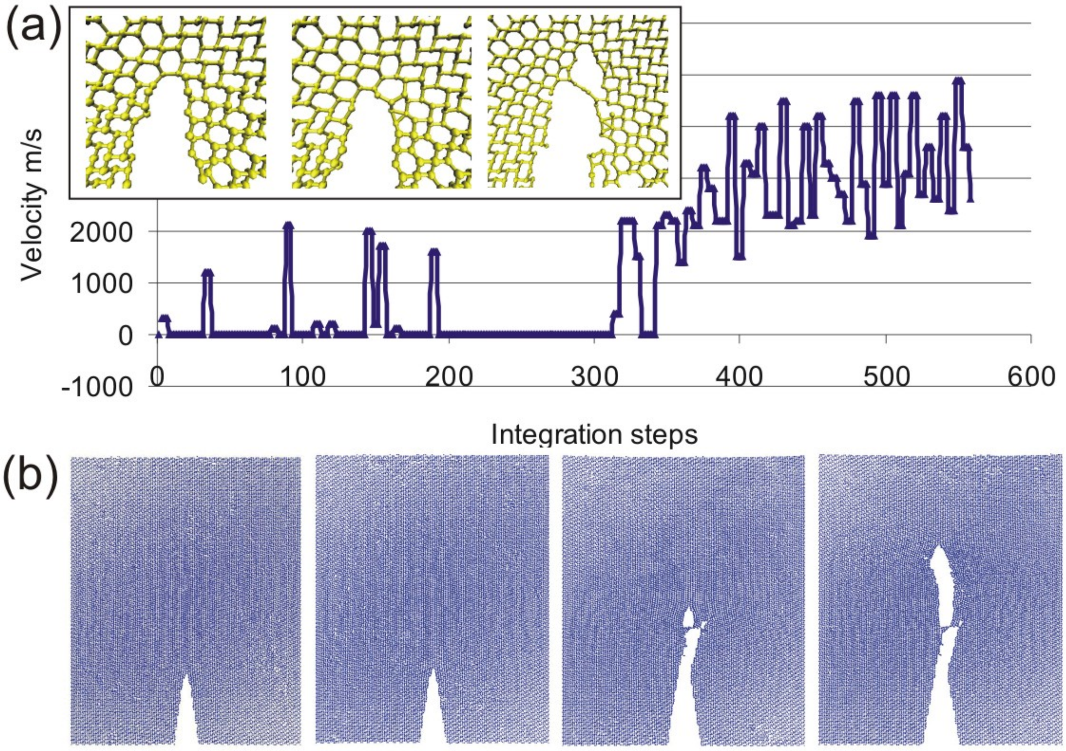

Figure 4: Subplot (a): Crack speed as a function of iterations. The inlays show a few snapshots of bond breaking processes during crack initiation. We observe that the crack does not start to propagate until a critical loading time, after which the crack speed jumps to around 2,000 m/s. This result agrees with the data shown in Figure 2 and 3, suggesting that crack propagation is not possible for speeds below a critical speed. Preliminary analysis suggests that this behavior is due to atomic rearrangements at the tip of the crack, leading to formation of a 7-5 membered Si-ring. Subplot (b): Snapshots of crack extension during the simulation. After a short period of straight crack extension, the crack starts to change direction, creating a rough crack surface.

14. Stillinger, F. and T.A. Weber, *Computer-simulation of local order in condensed phases of silicon.* Phys. Rev. B, 1985. **31**(8): p. 5262-5271.
15. Buehler, M.J., A.C.T.v. Duin, and W.A. Goddard, *Multi-paradigm modeling of dynamical crack propagation in silicon using the ReaxFF reactive force field.* Phys. Rev. Lett., 2006. **96**(9): p. 095505.
16. Duin, A.C.T.v., et al., *ReaxFF: A Reactive Force Field for Hydrocarbons.* J. Phys. Chem. A, 2001. **105**: p. 9396-9409.
17. Duin, A.C.T.v., et al., *ReaxFF SiO: Reactive Force Field for Silicon and Silicon Oxide Systems.* J. Phys. Chem. A, 2003. **107**: p. 3803-3811.
18. Parker, S.G., C.R. Johnson, and D. Beazley, *Computational steering software systems and strategies.* IEEE Computational Science and Engineering, 1997. **4**(4): p. 50-599.
19. Becke, A.D., *Density-function thermochemistry. 3. The role of exact exchange.* J. Chem. Phys., 1993. **98**(7): p. 5648-5652.
20. Bernstein, N. and D.W. Hess, *Lattice trapping barriers to brittle fracture.* Physical Review Letters, 2003. **91**(2).

Plasticity and Dislocation Dynamics in Micro and Nano-scale Cylinders

Wei Cai

Mechanical Engineering Department, 496 Lomita Mall, Durand Building, 94305-4040, Stanford, USA

Comparing theoretical models and experimental measurements on the deformation of crystals at the micro and nano-scale is expected to bring new understanding on the fundamental nature of plasticity. Recently, a dislocation-starvation model was proposed to explain the dramatic increase of flow stress as the diameters of gold micro-pillars go to nanoscale (Greer and Nix, Applied Physics 2005). On the other hand, recent indentation experiment on gold nanowires indicates dislocation hardening even at the nanoscale (Wu et al. Nature Materials, 2005). To investigate this controversy, we develop Dislocation Dynamics (DD) simulation models in a cylinder with its diameter ranging from micro to nanoscale. Such simulations are enabled by an efficient algorithm to account for the image stress of the traction-free cylindrical surface, based on the analytic expressions of the elastic displacement potentials. The DD simulations also account for the orientation dependence of dislocation core energy and mobility computed from atomistic models. Stress-strain curves calculated by these simulations will be compared with experimental measurements.

Contribution to the study of kinematics of the damage zone in a brittle material

M. Chabaat & S. Djouder

Department of Constructions, Civil Engineering Faculty, U.S.T.H.B.
B. P. 32 El-Alia, Bab Ezzouar, Algiers, 16111 Algeria mchabaat2002@yahoo.com

ABSTRACT

In this study, kinematics of the Damage Zone (DZ) or the so-called Fracture Process Zone (FPZ) which often precedes the crack during its propagation and characterized by few degrees of freedom (elementary movements) such as translation, rotation, isotropic expansion and distortion are considered. On the basis of a stress field distribution obtained by the use of a Semi-Empirical Approach (SEA), which relies on the Green's functions, these driving forces corresponding to the mentioned degrees of freedom are formulated within the framework of the plane problem of elastostatics. Thus, expressions for translation (J), isotrope expansion (M), distorsion (N) and interactions effects representing the active parts of crack driving forces known as energy release rates are formulated in a purely theoretical context.

1. Introduction

Evaluation of Energy Release Rates (ERR) for a single edge notch specimen containing a crack surrounded by a Damage Zone (DZ) is considered. This zone can reveal itself as microcracks, voids, pores, slip lines, etc… [1-3]. Thus, a number of theoretical models have been proposed for the description of a stress field and kinetics of a DZ [4]. The traditional one identifies the DZ as a plastic zone and uses the well developed technique of the plasticity theory for the determination of its size, shape, energy release rates etc… According to recent experimental results, some damage patterns do not yield any model of plasticity [4]. As an example, a cross section of an actual fractured specimen [5] shows that the shape of the damage is quite different (see Fig. 1a and 1b). Because of this difference, a plasticity critera is not adequate for damage characterization. However, elastoplastic solution is currently employed due to the lack of other approaches.

In this study, a Semi Empirical Method (SEM) is proposed for evaluating the stress field and the different energy release rates. This approach is based on the representation of displacement discontinuities by means of the Green's function theory [6, 7]. Herein, we suggest a more realistic model for which the result can be obtained using the experimental data and thus avoiding the difficulties of analytical solutions.

a) Shape of plastic zone (elastoplastic solution).

b) Distribution of damage through (semi-cristaline Polymer [1]).

Figure 1 : Plastic zone size specimen.

2. Description of the procedure:

The displacement field $\widetilde{U}(\tilde{\ })$ at a point $\tilde{\ }$ generated by a discontinuity at point $\tilde{\ }'$ (see Fig. 2) can be represented for a plane problem as

$$\widetilde{U}^{\mathrm{d}} = \int_{\Omega} \tilde{\mathrm{b}}(\tilde{\mathrm{x}}')\Phi(\tilde{\mathrm{x}}, \tilde{\mathrm{x}}')\,d\tilde{\mathrm{x}}' \tag{1}$$

where $\tilde{\mathrm{b}}(\tilde{\mathrm{x}}')$ is the discontinuity displacement (or potential density), $\Phi(\tilde{\mathrm{x}}, \tilde{\mathrm{x}}')$ is the second Green's tensor which is defined as the displacement response at the point of observation $\tilde{\mathrm{x}}$ due to a force dipole applied at the point of discontinuity $\tilde{\mathrm{x}}'$ and the integration is performed along the discontinuity line Ω. This second Green's tensor for a plane stress problem is given as follows [7]:

$$\Phi(\tilde{x},\tilde{x}')=\frac{(1+\nu)}{4\pi R^2}\left\{(1-\nu)\left[\tilde{n}_{\tilde{x}'}.\tilde{R}-\tilde{\mathrm{R}}.\tilde{\mathrm{n}}_{\tilde{x}'}-\tilde{\mathrm{n}}_{\tilde{x}'}.\tilde{R}.\tilde{E}\right]-2\frac{\tilde{\mathrm{n}}_{\tilde{x}'}.\tilde{R}}{R^2}.\tilde{R}.\tilde{R}\right\} \tag{2}$$

where $\tilde{\mathrm{n}}_{\tilde{x}'}$ is the unit normal vector in the dipole's direction $\tilde{\mathrm{x}}'$, ν is the Poisson's ratio, $\tilde{\mathrm{E}}$ is the unite tensor, and $\tilde{\mathrm{R}}$ is the position vector $\left(\tilde{R}=\tilde{\mathrm{X}}'-\tilde{\mathrm{X}}\right)$.

The problem is then formulated in terms of a system of singular equations for the unknown densities for each microcrack considered. The system of equations represents the boundary conditions both on the array of microcracks and on the main-crack as well. This system may be derived from Eqn. (1) by evaluating tractions and then setting them to zero on all the cracks considered in the system (crack surfaces are traction free). Besides, the conditions on the outer border are satisfied because of the properties of the second Green's tensor. In order to avoid solving the system of integral equations, a semi-empirical procedure based on experimental results is suggested.

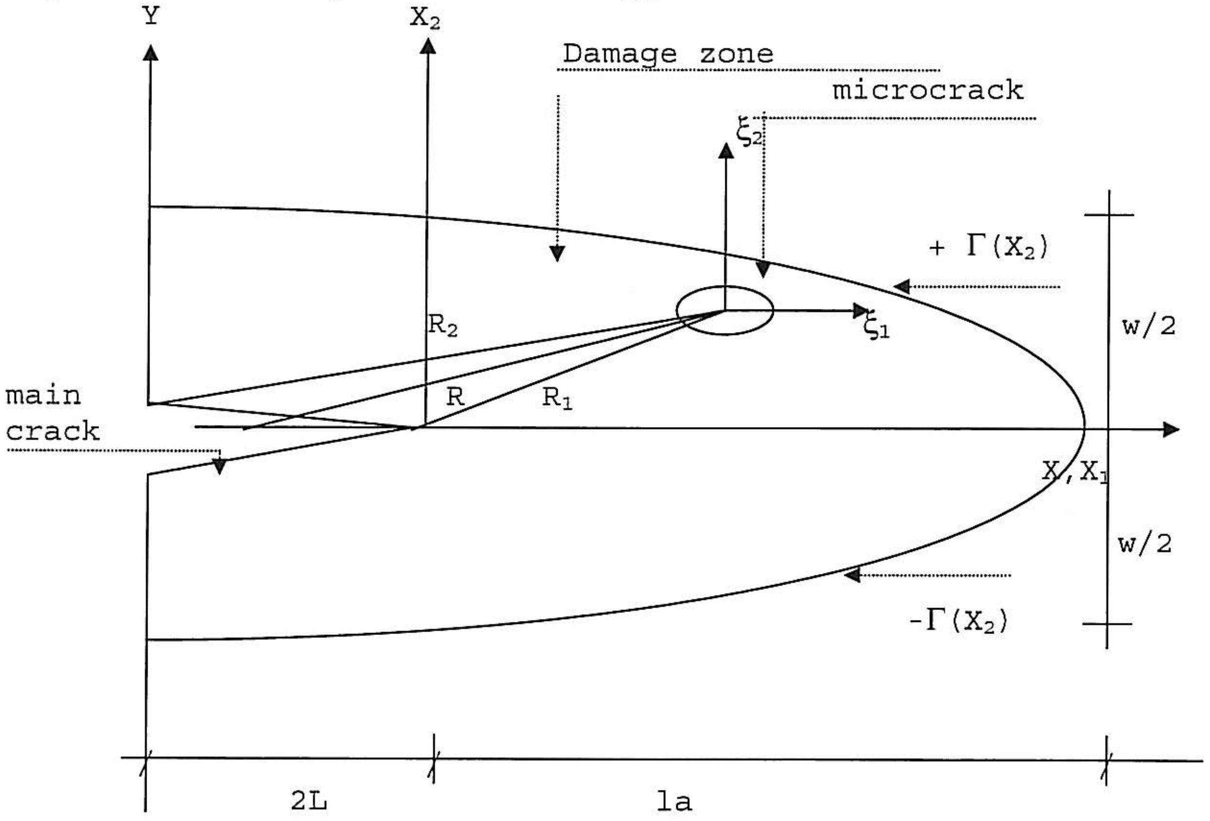

Figure 2 : Schematic representation of the damage zone.

At first, divide the area around the crack-tip into a network of small squares having N_1 vertical lines and N_2 horizontal lines as in Fig. 3a. Then, the displacement field $\widetilde{U}(\widetilde{x})$ due to discontinuities in each mesh can be represented as follows:

$$\widetilde{U}^{d}(\widetilde{x})=\sum_{k=1}^{N}\int_{\Omega^{k}}\widetilde{b}^{(k)}(\widetilde{x}').\Phi(\widetilde{x}',\widetilde{x})\,d\widetilde{x}' \tag{3}$$

where N is the number of discontinuities. Taking into account that for all discontinuities (Fig. 3b), Eqn. (3) becomes:

$$\widetilde{U}^{d}(\widetilde{x})=\sum_{\alpha_1=1}^{N_1}\sum_{\alpha_2=1}^{N_2}\sum_{k=1}^{N}\int_{\Omega^{(k)}\in A_{\alpha_1\alpha_2}}\widetilde{b}^{(k)}(\widetilde{x}').\Phi(\widetilde{x}',\widetilde{x})\,d\widetilde{x}' \tag{4}$$

For small mesh size in comparison to the size of the specimen, meaning $|\widetilde{x}'-\widetilde{x}|>>\max|\Delta\widetilde{x}'|$, we approximate $\Phi(\widetilde{x}',\widetilde{x})$ by $\Phi(\widetilde{x}_0',\widetilde{x})$ where $\widetilde{x}_0'$ is the position vector of the center of the mesh. With that in mind along with the mean value theorem, Eqn. (4) takes the following form:

$$\widetilde{U}^{d}(\widetilde{x})\cong\sum_{\alpha_1=1}^{N_1}\sum_{\alpha_2=1}^{N_2}\Phi(\widetilde{x}_0',\widetilde{x}).\widetilde{C}(\widetilde{x}').\Delta x'_{\alpha_1}\,\Delta x'_{\alpha_2} \tag{5}$$

where $\widetilde{C}(\widetilde{x}')=\dfrac{\sum_{k=1}^{N}\int_{\Omega^{(k)}\in A_{\alpha_1\alpha_2}}\widetilde{b}^{(k)}(\widetilde{x}')\,d\widetilde{x}'}{\Delta x'_{\alpha_1}\,\Delta x'_{\alpha_2}}$ is the concentration of discontinuities (or damage density). For infinitesimal squares ($N_1, N_2\mapsto\infty$) while $\Delta x'_{\alpha_1}$ and $\Delta x'_{\alpha_2}$ approaching zero, the sum in Eqn. (5) becomes a double integral over the entire damage zone in the limit. Thus, the displacement field due to the presence of damage may be presented in the following form:

$$\widetilde{U}^{d}(\widetilde{x}')=\iint_{V_d}\Phi(\widetilde{x}',\widetilde{x}).\widetilde{C}(\widetilde{x}')\,d\widetilde{x}' \tag{6}$$

in which V_d stands for the volume of the damage zone.

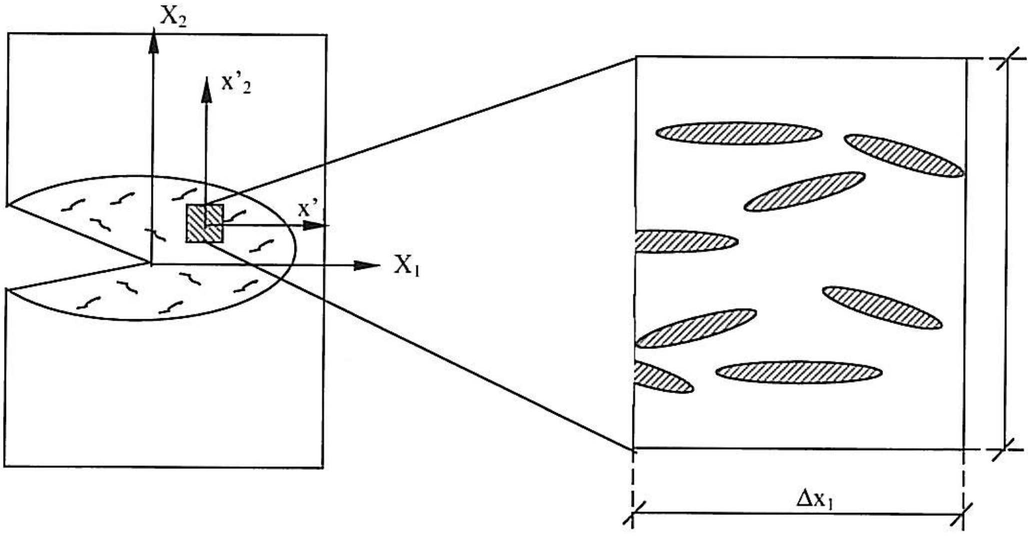

a) Subdivision of the damage zone into meshes

b) Representation of typical square for microcracks opening density.

Figure 3 : Schematic representation of the damage zone

3. Energy release rates evaluation

Consider a Single Edge Notch (SEN) specimen as shown in Fig. 4 in which a crack propagates surrounded by a layer of damage. The work W done by an applied force F at the grips ($x_2 = h$) is given as follows:

$$W = F.U_{\mathrm{Total}} \tag{7}$$

where U_{Total} is the total displacement at the grips. This latest is taken as a sum of the displacement at the grips in the initial state (with no cracks) U_{I} and the displacement at the grips due to the presence of the damage U_{DZ}, in other terms;

$$U_{Total} = U_{\mathrm{I}} + U_{\mathrm{DZ}} \tag{8}$$

The elastic potential energy P is given as:

$$\mathrm{P} = -(1/2).\mathrm{W} = -(1/2).F.U_{\mathrm{Total}} \tag{9}$$

Then, the total energy release rate A_{I} takes the following form:

$$A_{\mathrm{I}} = -\frac{1}{2\,\mathrm{t}}\frac{\partial \mathrm{P}}{\partial \mathrm{L}} = \frac{1}{2\,\mathrm{t}}F.\frac{\partial U_{\mathrm{Total}}}{\partial L} \tag{10}$$

where t is considered as the specimen thickness. Since U_{I} (no cracks) is independent of the crack length, Eqn. (10) is reduced to:

$$A_{\mathrm{I}} = \frac{1}{2\,\mathrm{t}}F.\frac{\partial U_{\mathrm{DZ}}}{\partial L} \tag{11}$$

The displacement U_{DZ} is an average of the displacement along the grips for a specimen of width B,

$$U_{CL} = \frac{2}{\mathrm{B}}\int U_2(\tilde{x})\Big|_{x_2=h}\,\mathrm{d}x_1 \tag{12}$$

where $U_2(\tilde{x})$ is derived by the use of the aforementioned Eqn. (6) given in section 2.

$$U_2(\tilde{x}) = \int_0^L \Phi_{22}(x_1' - \mathrm{x}_1, \mathrm{x}_2)\,\mathrm{b}_2(x_1')\,\mathrm{d}\mathrm{x}_1' + \iint_{V_{\mathrm{d}}} \Phi_{2\mathrm{j}}(x_1' - \mathrm{x}_1, \mathrm{x}_2' - \mathrm{x}_2)\,\tilde{\mathrm{C}}_{\mathrm{j}}(\tilde{x}')\,\mathrm{d}\tilde{\mathrm{x}}' \tag{13}$$

Carrying out this procedure, the variation of the displacement U_{DZ} given in Eqn. (12) takes the form;

$$\begin{aligned} \frac{\partial U_{CL}}{\partial L} &= \frac{2}{\mathrm{B}}\int_0^B \frac{\partial U_2^C(\tilde{x})}{\partial L}\bigg|_{x_2=h} dx_1 + \frac{2}{\mathrm{B}}\int_0^B \frac{\partial U_2^d(\tilde{x})}{\partial L}\bigg|_{x_2=h} dx_1 \\ &= \frac{2}{\mathrm{B}}\hat{\Phi}_{22}.\frac{\partial \hat{b}_2}{\partial L} + \frac{2}{\mathrm{B}}\hat{\Phi}_{2j}\hat{C}_j\frac{\partial V_d}{\partial L} + \frac{2}{\mathrm{B}}\hat{\Phi}_{2j}V_d\frac{\partial \hat{C}_j}{\partial L} \end{aligned} \tag{14}$$

where $\hat{\Phi}_{22}$, $\hat{\mathrm{b}}_2$, $\hat{\Phi}_{2\mathrm{j}}$ and $\hat{\mathrm{C}}_{\mathrm{j}}$ represent the average expression of $\Phi_{22}, \mathrm{b}_2, \Phi_{2\mathrm{j}}, \mathrm{C}_{\mathrm{j}}$ after integration, respectively. Then, the total ERR A_{I} in Eqn. (11) becomes by the use of Eqn. (14);

$$A_{\mathrm{I}} = \frac{F}{\mathrm{B\,t}}\hat{\Phi}_{22}\frac{\partial \hat{b}_2}{\partial L} + \frac{F}{\mathrm{B\,t}}\hat{\Phi}_{2j}.\hat{C}_j.\frac{\partial V_d}{\partial L} + \frac{F}{\mathrm{B\,t}}\hat{\Phi}_{2j}.V_L.\frac{\partial \hat{C}_j}{\partial L} \tag{15}$$

The above Eqn. (15) can be rewritten in a simplied way as

$$A_I = \lfloor J_I + M\partial_L \ell + \tilde{N}\partial_L \tilde{d} \rfloor + \Gamma\partial_L t \qquad (16)$$

where J_I, M and N correspond to the translational, the isotropic expansional and distorsional energy of the active zone, respectively. Here, Γ is the change in concentration (flaws and new crazes) and interaction effects (time dependency).

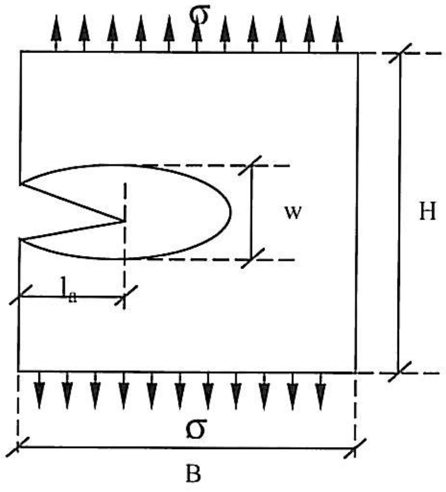

Figure 4 : Size dimensions of the proposed model

4- Conclusion

Theoretical expressions for translation (J), isotrope expansion (M), distorsion (N) representing the active parts of crack driving forces are formulated. It is also shown in a number of cases that J has a significant statistical distribution. It is the expenditure of energy into various modes of crack propagation meaning the translational motion of the crack with the process zone unchanging on one hand and the expansion as well as the distorsion of the DZ on the other hand. The latter constitutes an important percentage of the total energy release rate. Besides, the distribution of energy into modes varies size from one experiment to the other as being a loading history dependant quantity.

References

[1] J. Botsis, A. Chudnovsky and A. Moet, "Fatigue crack layer propagation in polystyrene", *Int. J. of Fracture,* Parts I and II, Vol. 33, 1987, pp.263-284.

[2] M. T. K. Takemori, "Fatigue fracture of polycarbonate", *Polymers Engng. and Sci.,* Vol. 22, 1982, pp. 937-645.

[3] M. Chabaat, "Comparison of minimal principal stress trajectories with crazes distribution", *Int. J. of Fracture,* Vol. 37, 1988, pp. 47-54.

[4] A. Chudnovsky, I. Palley and E. Baer, "Thermodynamics of the quasiequilibrial growth of crazes", *Int. J. of Mat. Sci.*, Vol. 16, 1981, pp.35-44.

[5] R. W. Hertzberg and J. A. Manson, Fatigue of engineering plastics, Academic Press, New York, 1980.

[6] M. Chabaat and S. Djouder, "Crack-microcracks interactions using a semi-empirical approach", *Int. J. of Mat. Sci. and Engng. A,* Vol. 387-389, 2004, pp. 361-3666.

[7] M. Chabaat, S. Djouder and M. Touati, "Semi-empirical stress analysis of a brittle material in a vicinity of a stress concentrator", *Int. J. of Applied Mech. and Mat.* Vol. 3-4, 2005, pp. 243-252.

On the role of lattice discreteness in brittle fracture

Mariella Ippolito,[1,2] **Alessandro Mattoni**[2] **and Luciano Colombo**[1,2,3]

[1]**Dept. Physics, Univ. Cagliari, Cittadella Universitaria, I-09042 Monserrato (CA), Italy**
[2]**SLACS Laboratory (CNR-INFM)**
[3]**DEMOCRITOS National Simulation Center (CNR-INFM)**

ABSTRACT

We investigate at atomistic level the failure strength in brittle solids containing isolated stress concentrators such as straight crack, circular hole and spherical hole. By means of molecular static calculation we found that in the case of nanosized stress concentrators there is a strong dependence on the defect size in contrast with the prediction of linear elasticity theory. We compare the atomistic results with an analytical theory named quantized fracture mechanics which takes into account the discreteness of the crystal lattice by introducing within the framework of the continuum elasticity theory the hypothesis of discrete crack propagation (fracture quantum). By a suitable choice of the fracture quantum it is possible to reconcile the atomistic results for the failure strength with the continuum theory at the nanoscale.

1. Introduction

Although solid mechanics is a well established field of investigation at the macroscopic level, a basic question is still open: whether continuum laws of mechanics are valid at the nanoscale. In particular, in the technologically relevant case of nanosized stress concentrators the linear elastic fracture mechanics (LEFM) theory fails to correctly predict the failure strength and therefore an alternative approach is required.

As a matter of fact, for the case of a straight crack, stress and strain fields computed by LEFM became mathematically singular at a vanishing distance from the crack tip, thus making hard to predict relevant quantities (like toughness or crack resistance) by using local stress criteria. Furthermore, at the nanoscale the linear elasticity theory fails also in the case of blunt defect such as elliptical cracks or holes. For istance, the case of a cylindrical or spherical hole a constant stress intensification is expected, regardless of the hole size. While such a prediction is valid for macroscopic defects it is in contrast with experimental and numerical results at the nanoscale.

Atomistic simulation have demonstrated to be a valuable tool to study the crack resistance of nanocracked brittle solids [1]. In the present work we used atomistic simulation to calculate the failure strength of cubic silicon carbide (β-SiC) containing nanosized stress concentrators. By investigating the failure strength dependence upon the defect size we found a strong deviation from the linear elasticity prediction for defects as small as few nm. The atomistic results are compared to the expectation of an energy based theory, named Quantized Fracture Mechanics (QFM) [2], that modifies same basic assumption of the standard continuum based fracture

2. Theoretical framework

Inter-atomic forces were calculated according to a modified version of Tersoff potential [3,4] that correctly reproduces the brittle failure of silicon carbide [1].

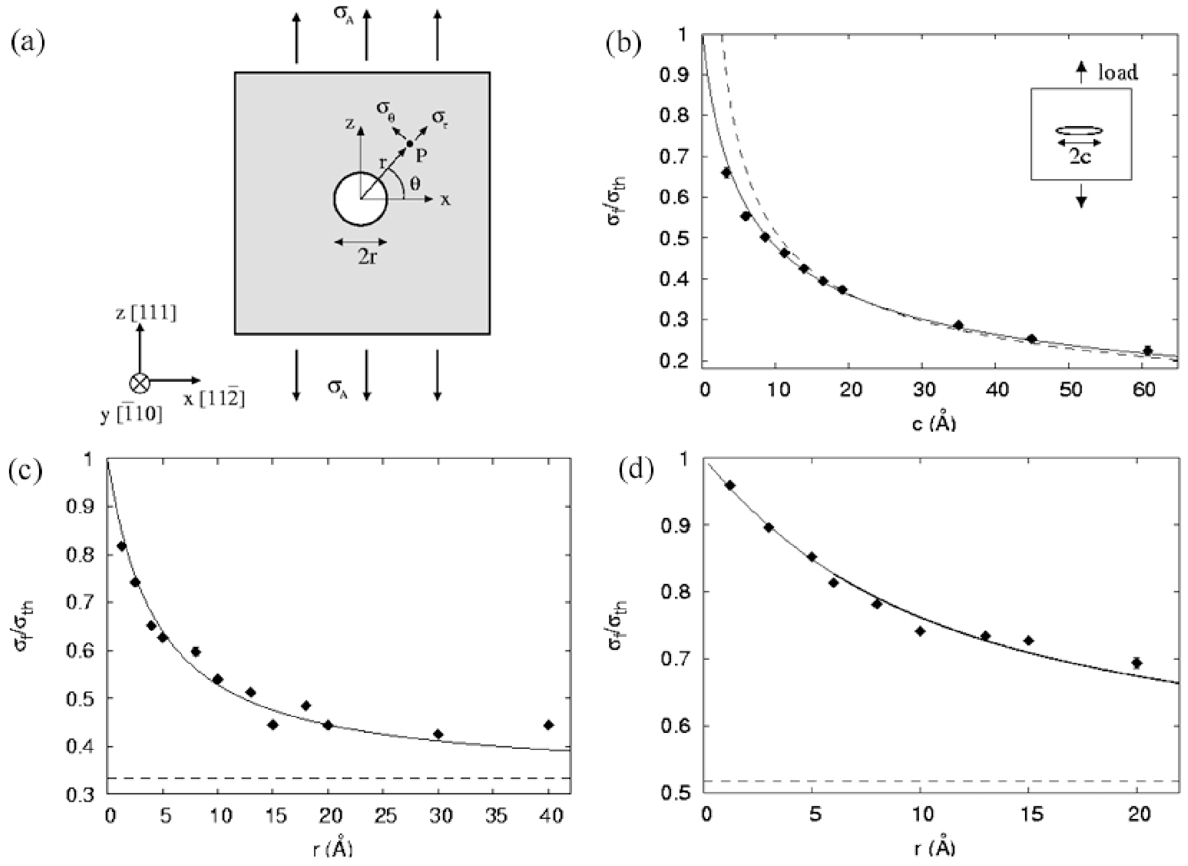

Figure 1. (a) Geometry of a plate containing a cylindrical hole and strained along z-direction. The alignment of the crystallographic axes is reported. (b) Failure strength of a plate containing a crack of semi-length *c*. Symbols are atomistic data; the continuum line is the QFM fit and the dashed line is the Griffith curve. (c) Failure strength of a plate containing a cylindrical hole of radius *r*. Symbols are atomistic data; the continuum line is the QFM fit and the dashed line is the liner elastic expectation $\sigma_f / \sigma_{th} = 1/3$. (d) failure strength of a plate containing a spherical hole of radius r. Symbols are the atomistic data; the continuum line is the QFM fit and the dashed line is the liner elastic expectation $\sigma_f / \sigma_{th} \approx 1/2$.

The simulation cell consists of a β-SiC monocrystal containing three different types of isolated defects: a straight crack, a cylindrical hole (Fig. 1 (a)) and a spherical hole. In order to reproduce the plane strain condition, in the x-y plane the system was kept fixed at the equilibrium lattice parameter of β-SiC (4.318 Å) and periodically repeated. A tensile load σ_A was applied along the z direction according to the constant traction method [5].

For each geometry and for a given load we relaxed the atomic force by a dumped dynamics minimization algorithm. To estimate the failure strength of the defected specimen we varied the applied load up to the failure condition $\sigma_A = \sigma_f$ At loads higher than this critical threshold a fracture originates from the defect and a brittle failure occurs along the [111] plane in all the considered cases.

3. Results

For all the defects considered we found that the failure strength increases as the defect size decreases and approaches a maximum value that corresponds to the ideal strength σ_{th} of β-SiC (we calculated $\sigma_{th} \approx 58$ GPa).

The results for a straight crack are reported in Fig. 1 (b). According to LEFM (dashed line) a singularity is expected at vanishing crack lengths. At variance, the atomistically calculated critical stress (symbols) monotonically approaches the ideal strength σ_{th} of the crystal.

The results obtained for the cylindrical and spherical hole are reported in Fig. 1 (c) and (d), respectively. The linear elastic prediction, $\sigma_f / \sigma_{th} = 1/3$ for the cylindrical case and $\sigma_f / \sigma_{th} \approx 1/2$ for the spherical case (horizontal dashed lines in figure), it is actually found to only represent the asymptotic limit for large radii.

In order to explain the atomistic data we considered the QFM theory. According to this theory, based on Novozhilov stress criterion [6], the failure occurs when the average of the stress over a small region of length d_0 at the hole (crack) tip reaches the tensile strength of the plate without defect σ_{th}. Within this formalism d_0, named fracture quantum, is a measure of the minimum fracture advance and it is expected to be of the order of the lattice spacing. It is important to note that the QFM theory is not able to fix a value for such a quantity. Accordingly, in this framework we use such a fracture quantum as parameter to calibrate on atomistic results.

The best fit obtained for the three defects is represented by continuum line in Fig.1 (b), (c) and (d). The QFM theory well reproduces the atomistic data over all the investigated range and the best fits were obtained taking d_0=6.0Å, d_0=6.6 Å and d_0=7.9 Å respectively for the crack and for the cylindrical and spherical hole. For any given material d_0 depends on the geometry of the system and in particular on the dimensionality of the defects.

In conclusion it is possible by atomistic simulation to calculate the failure strength of nanosized defects. The atomistic results demonstrate that the liner elasticity theory is not valid at the nanoscale for very small defect while QFM can be successfully used to interpolate the atomistic data. According to the present study the fracture quantum introduced by QFM theory it is not a material parameter, rather it depends upon the geometry of the defect.

Acknowledgements

This work is funded by MIUR under project PON-CyberSar.
We warmly acknowledge useful discussion with Nicola Pugno (Politecnico di Torino, Italy) and Fabrizio Cleri (Universite de Lille, France).

References

[1] A. Mattoni, L.Colombo and F. Cleri, Phys. Rev. Lett. 95, 115501 (2005).
[2] N. M. Pugno and R. S. Ruoff, Phil. Mag. 84, 2829 (2004).
[3] J. Tersoff, Phys. Rev. B 39, 5566 (1989).
[4] A. Mattoni, M. Ippolito, L. Colombo, in preparation
[5] F. Cleri, Phys. Rev. B 65, 014107 (2002).
[6] V. Novozhilov, Prik. Mat. Mek. 33, 212 (1969).

Temperature and Strain Induced Microstructural Evolution of Nanocrystalline Silicon

Alessandro Mattoni[1], and Luciano Colombo[1,2,3]

[1]SLACS Laboratory (CNR-INFM)
[2]Dept. Physics, University of Cagliari, Cittadella Universitaria, 09042 (Italy)
[3]DEMOCRITOS National Simulation Center (CNR-INFM)

ABSTRACT

Nanocrystalline silicon is a biphasic material consisting of a dispersion of crystal seeds embedded into an amorphous matrix and it represents a promising multifunctional material at least for low cost photovoltaic applications. The improvements of optoelectronic properties requires a better control and modelling of the material nanomorphology. By means of atomistic simulations based on the EDIP potential we study the effect of the temperature on the nanocrystals growth within the amorphous matrix. The average crystallinity is calculated from the atomic trajectories and it is used to characterize the microstructure evolution.

1. Introduction

Nanocrystalline silicon (nc-Si) is considered as a promising candidate for low cost and high efficiency solar cells [1], having already reached top efficiencies around 11% comparable with those obtained by using stabilized amorphous silicon (a-Si). Nanocrystalline silicon consists basically of a dispersion of silicon nanocrystals (nc-Si) embedded into an amorphous matrix and it is interesting also for optoelectronic applications, since it mimics a dispersion of Si dots into an a-Si matrix possibly inducing quantum confinement effects. Despite such potential merits, the industrial application of nc-Si are limited by the possibility to proper tuning the nanomorphology of the material. Under this respect, there is real need of theoretical characterization of the microstructure of nc-Si/a-Si systems and its evolution under different thermal and stress conditions. Model potential atomistic simulations have been succesfully applied to study the recrystallization from liquid silicon[2] and from amorphous phase both in the pure[3] and boron doped silicon systems [4,5]. In the present paper, by means of molecular dynamics (MD) simulations based on the EDIP atomic force model[6] we generate nc-Si/a-Si models and we characterize their thermal microstructure evolution. We focus our work on textured nc-Si that is modeled by a set of crystalline fibers oriented along the same crystallographic axes, and embedded into an amorphous silicon matrix. According to preliminary experimental observation similar structures might occur during LEPECVD experiments[7].

2. Results

The starting point of the present simulation protocol was to generate an amorphous slab by quenching a liquid silicon sample down to room temperature. The slab dimensions along the x,y, and z cartesian axes were 2.71 nm, 27.11 nm, and 27.11 nm, respectively, and the system was periodically replicated. This corresponds to a total number of particles as large as 10^5

atoms. In order to simulate nanosecond-long annealings, we needed a particularly efficient aqnd scalable MD code[8]. A given number of parallel fibers were extracted from a silicon monocrystal and randomly inserted into the amorphous slab. The axes of the crystalline fibers were chosen along the [001] crystallographic direction and parallel to the x direction of the simulation cell. In the orthogonal y-z plane the fibers were rotated at random and eventually the configuration were relaxed by a damped dynamics minimization algorithm. A y-z plane view of part of the system is reported in Fig 1.

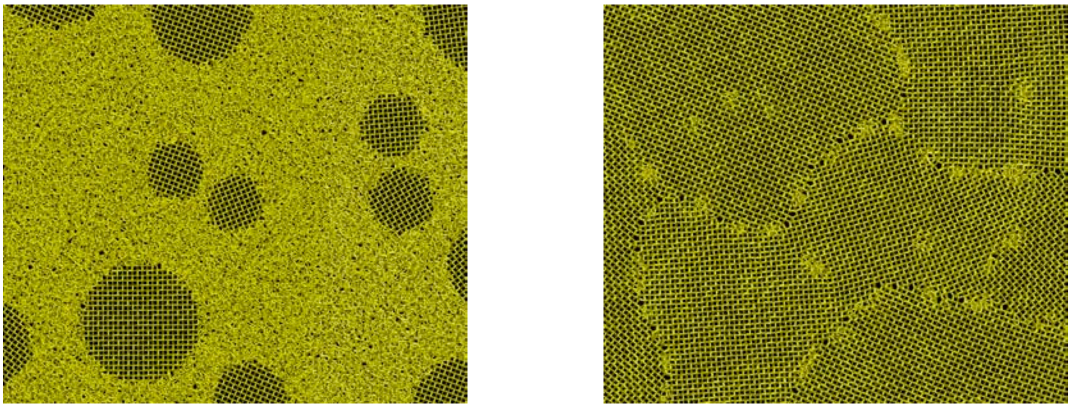

Figure 1- Left panel: Snapshot showing a model nc-Si system formed by inserting a random distribution of nm-sized fibres into an otherwise amorphous matrix. Right panel: A model nc-Si is obtained after 2ns annealing at T=1200K during which grains recrystallization is thermally activated. The residual amorphous layers correspond to thin intergranular regions as large as few atomic spacings.

The system was annealed at T=1200K in order to thermally activate the recrystallization. After 2ns long annealing an equilibrium configuration was obtained and it is reported in Fig 2. The amorphous matrix is dramatically reduced and now limited to just a thin region localized at the grain boudaries. At least qualitatively, present computational samples display intriguing structural similarities with LEPECVD real samples[7]. The dimension of the grains depends on the initial density of fibres, ranging within 4-15 nm. In order to better characterize the computed structures we calculated the structure factor:

$$\Theta = \left| \frac{1}{N} \sum_i e^{i\vec{k}\cdot R_i} \right| \tag{1}$$

where k is the vector $8\pi/a_0[1,0,0]$ parallel to the axes of the crystalline fibers (a_0 is the c-Si equilibrium lattice parameter). Such a choice corresponds to the Bragg condition in the x direction. The structure factor of a nc-Si/a-Si mixed phase (divided by that of perfect crystal at the same temperature, $\chi(T)=\Theta(T)/\Theta_c(T)$) is the crystallinity of the system, here defined as the ratio between the crystal-like to the total number of atoms. In the range of temperature 600-1400K, the normalization function $\Theta_c(T)$ is approximated by a linear function of the temperature. We are able in this way to calculate the crystallinity of the system during annealing at different temperatures (see Fig 2). At temperature below T=1100K the structural evolution is dominated by the growth of non-interacting grains. At higher temperature the growth is dominated by the competition between grains so that the crystallinity tends to an asymptotic limit (χ=0.985 at T=1200K). The enthalpy difference between the crystalline and a disordered silicon phase decreases with temperature. At T=1400K, according to the classical nucleation theory, only the largest grains survive and grow. As a result the crystallinity curve exhibits a non monothonic behavior. The resulting nc-Si structure contains large grains and turns out to have a slightly higher crystallinity.

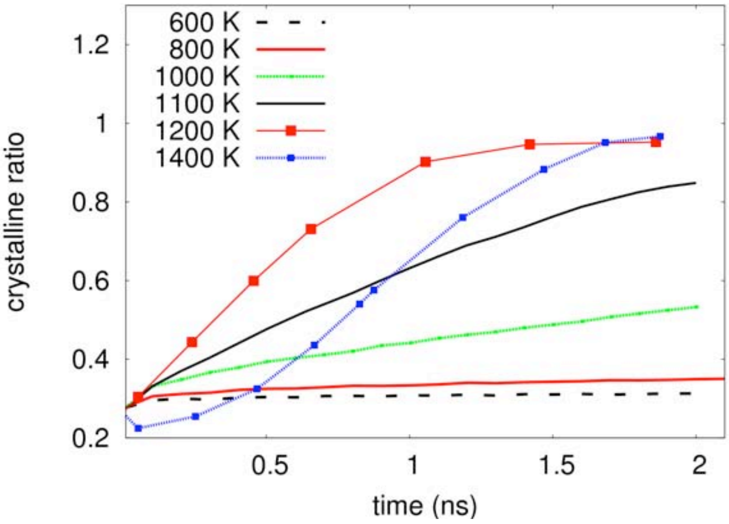

Figure 2: Evolution of the crystallinity of the nc-Si/a-Si model during annealing at temperatures in the range 600K-1400K.

3. Conclusions

Models for columnar nanocrystalline silicon have been generated by molecular dynamics simulations. By calculating the average structure factor we have been able to calculate the crystallinity of the sample during the annealing at different temperatures. Preliminary results (here not shown) seem to indicate that the growth of an isolated fiber follows an asymptotic power law with an exponent that depends on temperature[9]. At variance, in the case of a nc-Si system formed by a distribution of crystallites, the asymptotic growth is controlled by grains competition. The tentative conclusion is that the crystallinity exhibits an upper limit depending upon temperature.

Acknowledgements

This work is funded by EU-STREP “NANOPHOTO”.

References

[1] K. Bruhne, et al., Thin Solid Films 395, 163 (2001).
[2] L. Brambilla, et al., Appl. Phys. Lett. 77, 2337 (2000).
[3] N. Bernstein, et al., Phys. Rev B 61, 6696 (2000).
[4] A. Mattoni, and L. Colombo, Europhys. Lett. 62, 862 (2003).
[5] A. Mattoni, and L. Colombo, Phys. Rev. B 69, 045204 (2004).
[6] J. F. Justo, et al., Phys. Rev. B 58, 2539 (1998).
[7] M. Acciarri, et al., Mat. Sci. Eng. B, in press (2006).
[8] S. Meloni, et al., Comp. Phys. Comm. 169, 462 (2005).
[9] A. Mattoni, and L. Colombo, in preparation (2006).

Atomistic to continuum scale transition for crystalline materials – a comparative study of quasicontinuum approaches

Alexander Stukowski[1] , **Bernhard Eidel**[2]

[1]Dept. of Physics, Institute of Condensed Matter Physics,
Technical University Darmstadt, Hochschulstr. 8, 64289 Darmstadt, Germany
[2]Dept. of Civil Eng., IWMB, (`eidel@iwmb.tu-darmstadt.de`)
Technical University Darmstadt, Petersenstr. 12, 64287 Darmstadt, Germany

ABSTRACT

This contribution presents an extended analysis of a recent quasicontinuum (QC) approach (Knap and Ortiz, J. Mech. Phys. Solids, 49(9):1899–1923, 2001), where a fully nonlocal methodology exhibits a seamless transition from the atomistic to the continuum description of crystalline solids at zero temperature. We show that the cluster summation rule to compute the approximate forces at representative atoms without a direct link to energy potentials leads to nonconservative forces and to a nonsymmetric stiffness matrix. To overcome this drawback we propose the application of the cluster summation rule to the total potential energy, which is used to consistently derive the nodal forces and the stiffness matrix.

1 Introduction

The basic idea of the QC method, introduced in [1], is an adaptive coarsening of the atomistic description of the crystal lattice by the introduction of kinematic constraints borrowed from the finite element method; full atomistic resolution along with interatomic potentials is demanded in critical regions with a strong spatial variation of deformation, whereas in regions with weakly varying deformation fields, *representative atoms* are chosen to represent a large number of atoms by interpolation via shape-functions, see Fig. 1 for an application in nanoindentation. In [2] a new class of summation rules is formulated in which the atomic forces are sampled over clusters of atoms. At the center of each sampling cluster there is a representative atom corresponding to a FE mesh node. The sampled force is approximately computed for each representative atom and an equilibrium system of equations is set up and finally solved numerically.

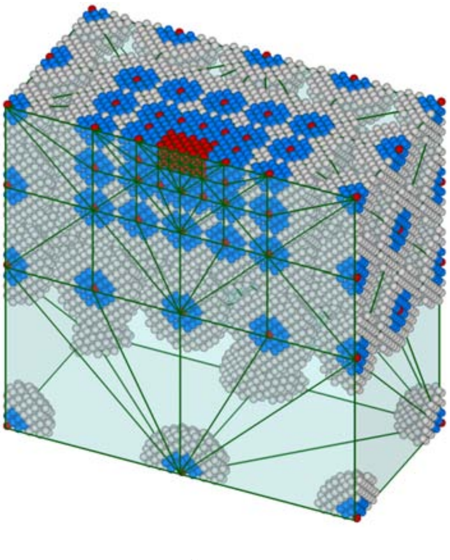

Figure 1: *Cross section through a test sample used for nanoindentation simulation. Representative atoms (red), cluster atoms (blue) and passive padding atoms (gray) up to the interaction cutoff radius are shown.*

We consider a crystal in d-dimensional space consisting of a set $\mathscr{L} \subset \mathbb{Z}^d$ of atoms, that are initially located on a Bravais lattice spanned by lattice vectors $\boldsymbol{a}_1, \ldots, \boldsymbol{a}_d$. Their coordinates in the initial configuration read $\boldsymbol{X}_{\boldsymbol{l}} = \sum_{i=1}^{d} l^{(i)} \boldsymbol{a}_i$, $\boldsymbol{l} \in \mathscr{L} \subset \mathbb{Z}^d$. The corresponding atomic coordinates in the current configuration are denoted by the vectors $\boldsymbol{x}_{\boldsymbol{l}}$. In order to considerably reduce the number of unknowns in the computation, some atoms $\mathscr{L}_h \subset \mathscr{L}$ are chosen to be representative atoms. Only these representative atoms keep their degrees of freedom whereas the positions of all other atoms $\overline{\mathscr{L}_h} = \mathscr{L} \backslash \mathscr{L}_h$ are defined by means of interpolation: $\boldsymbol{x_l} = \sum_{j \in \mathscr{L}_h} \boldsymbol{x_j} \varphi_{\boldsymbol{j}}(\boldsymbol{X_l})$, $\boldsymbol{l} \in \overline{\mathscr{L}_h}$. The application of the linear interpolation functions $\varphi_{\boldsymbol{j} \in \mathscr{L}_h}$ with $\sum_{\boldsymbol{j} \in \mathscr{L}_h} \varphi_{\boldsymbol{j}}(\boldsymbol{X_i}) = 1 \ \forall \ \boldsymbol{i} \in \mathscr{L}$ and $\varphi_{\boldsymbol{j}}(\boldsymbol{X_{j}}') = \delta_{\boldsymbol{jj'}} \ \forall \ \boldsymbol{j}, \boldsymbol{j}' \in \mathscr{L}_h$ requires the generation of a triangulation that connects the representative atoms.

2 Force based Cluster Summation Rule

Knap and Ortiz [2] have proposed a *cluster based summation rule* to approximately compute the force $\tilde{\boldsymbol{f}}_{\boldsymbol{a}}$ acting on a mesh node $\boldsymbol{a}$ without direct link to an energy functional:

$$\tilde{\boldsymbol{f}}_{\boldsymbol{a}} = \sum_{\boldsymbol{i} \in \mathscr{L}_h} n_{\boldsymbol{i}} \sum_{\boldsymbol{k} \in \mathcal{C}_{\boldsymbol{i}}} \boldsymbol{f_k} \varphi_{\boldsymbol{a}}(\boldsymbol{X_k}) \tag{1}$$

with $n_{\boldsymbol{i}}$ being the cluster weight, $\mathcal{C}_{\boldsymbol{i}}$ being the set of sampling atoms in the cluster associated with node $\boldsymbol{i}$ and $\boldsymbol{f_k}$ being the force acting on atom $\boldsymbol{k}$ which is computed using the selected interaction potential. If a simple pair-potential $V(r)$ is chosen, then the force expression has the format $\boldsymbol{f_k} = -\sum_{\boldsymbol{l} \in \mathscr{L}} V'(|\boldsymbol{r_{kl}}|) \frac{\boldsymbol{r_{kl}}}{|\boldsymbol{r_{kl}}|}$, where $\boldsymbol{r_{kl}} = \boldsymbol{x_k} - \boldsymbol{x_l}$ is the vector connecting atom $\boldsymbol{k}$ and atom $\boldsymbol{l}$. The global stiffness matrix $\mathbf{K} \in \mathbb{R}^{N_h d \times N_h d}$ (N_h = number of repatoms) is assembled from the subelements $\mathbf{K}_{\boldsymbol{ab}} \in \mathbb{R}^{d \times d}$:

$$\mathbf{K}_{\boldsymbol{ab}} = -\frac{\partial \tilde{\boldsymbol{f}}_{\boldsymbol{a}}}{\partial \boldsymbol{x_b}} = -\sum_{\boldsymbol{i} \in \mathscr{L}_h} n_{\boldsymbol{i}} \sum_{\boldsymbol{k} \in \mathcal{C}_{\boldsymbol{i}}} \frac{\partial \boldsymbol{f_k}}{\partial \boldsymbol{x_b}} \varphi_{\boldsymbol{a}}(\boldsymbol{X_k}) \qquad \text{with} \tag{2}$$

$$\frac{\partial \boldsymbol{f_k}}{\partial \boldsymbol{x_b}} = -\sum_{\boldsymbol{l} \in \mathscr{L}} [\varphi_{\boldsymbol{b}}(\boldsymbol{X_k}) - \varphi_{\boldsymbol{b}}(\boldsymbol{X_l})] \left[\frac{V'(|\boldsymbol{r_{kl}}|)}{|\boldsymbol{r_{kl}}|} \mathbb{I} + \left(\frac{V''(|\boldsymbol{r_{kl}}|)}{|\boldsymbol{r_{kl}}|^2} - \frac{V'(|\boldsymbol{r_{kl}}|)}{|\boldsymbol{r_{kl}}|^3} \right) \boldsymbol{r_{kl}} \otimes \boldsymbol{r_{kl}} \right]. \tag{3}$$

Please note that $\mathbf{K}$ is nonsymmetric which follows from the nodal forces $\tilde{\boldsymbol{f}}_{\boldsymbol{a}}$ being nonconservative. There is no total energy functional corresponding to the force function (1) even if the primary physical problem is of potential type.

Many popular optimization algorithms (like the CG-method) use the gradient of the function to quickly find its local minima. But almost all implementations of minimization algorithms need the value of the quantity itself that is to be minimized and which is not available here.

One could use root finding algorithms to directly solve for force equilibrium ($\tilde{\boldsymbol{f}}_{\boldsymbol{a}} = \boldsymbol{0} \ \forall \ \boldsymbol{a} \in \mathscr{L}_h$). But as these algorithms are tailored towards generic functions they do not exploit the directional information contained in the force function. Above all there may be no solution to the equilibrium system of equations at all.

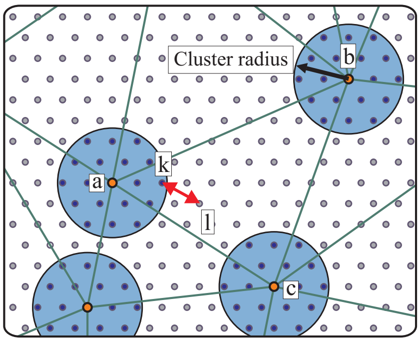

Figure 2: *Energy based cluster summation rule: The interaction energy of atoms* $\boldsymbol{k}$ *and* $\boldsymbol{l}$ *leads to a pair of forces that is distributed to the element nodes* $\boldsymbol{a}$, $\boldsymbol{b}$, *and* $\boldsymbol{c}$ *according to the barycentric coordinates of the inner atoms.*

3 Energy based Cluster Summation Rule

To overcome in some respect the discussed drawbacks of the approach in [2] we propose a framework, that uses an energy based summation rule instead of the force based one. The total potential energy of the system is approximately computed using a sampling technique like the one Knap and Ortiz use for the nodal forces.

Starting from lattice statics the exact total potential energy of the system is $E^{tot} = \sum_{\boldsymbol{k}\in\mathscr{L}} E_{\boldsymbol{k}}$, with $E_{\boldsymbol{k}}$ being the energy of the atom $\boldsymbol{k}$. Applying the cluster summation rule leads to the approximation

$$E^{tot} \approx \sum_{\boldsymbol{i}\in\mathscr{L}_h} n_{\boldsymbol{i}} \sum_{\boldsymbol{k}\in\mathcal{C}_{\boldsymbol{i}}} E_{\boldsymbol{k}}\,. \tag{4}$$

The equilibrium configurations of interest are the minimizers of E^{tot}, i.e. the solutions of the variational problem $\min_{\{\boldsymbol{x}_{\boldsymbol{a}}\}} E^{tot}$. The first derivative of the total potential energy with respect to the position of some node $\boldsymbol{a}$ reads:

$$-\tilde{\boldsymbol{f}}_{\boldsymbol{a}} = \frac{\partial E^{tot}}{\partial \boldsymbol{x}_{\boldsymbol{a}}} = \sum_{\boldsymbol{i}\in\mathscr{L}_h} n_{\boldsymbol{i}} \sum_{\boldsymbol{k}\in\mathcal{C}_{\boldsymbol{i}}} \left[\sum_{\boldsymbol{l}\in\mathscr{L}} \frac{1}{2} V'(|\boldsymbol{r}_{\boldsymbol{kl}}|)\frac{\boldsymbol{r}_{\boldsymbol{kl}}}{|\boldsymbol{r}_{\boldsymbol{kl}}|}\left[\varphi_{\boldsymbol{a}}(\boldsymbol{X}_{\boldsymbol{k}}) - \varphi_{\boldsymbol{a}}(\boldsymbol{X}_{\boldsymbol{l}})\right]\right]. \tag{5}$$

This consistent gradient function yields an additional term $-\varphi_{\boldsymbol{a}}(\boldsymbol{X}_{\boldsymbol{l}})$, cf. Fig. 2, and a factor 1/2 compared to the force formula (1). The corresponding stiffness matrix is

$$\mathbf{K}_{\boldsymbol{ab}} = \frac{\partial^2 E^{tot}}{\partial \boldsymbol{x}_{\boldsymbol{a}} \partial \boldsymbol{x}_{\boldsymbol{b}}} = \sum_{\boldsymbol{i}\in\mathscr{L}_h} n_{\boldsymbol{i}} \sum_{\boldsymbol{k}\in\mathcal{C}_{\boldsymbol{i}}} \sum_{\boldsymbol{l}\in\mathscr{L}} \frac{1}{2}\Big[\varphi_{\boldsymbol{a}}(\boldsymbol{X}_{\boldsymbol{k}}) - \varphi_{\boldsymbol{a}}(\boldsymbol{X}_{\boldsymbol{l}})\Big]\Big[\varphi_{\boldsymbol{b}}(\boldsymbol{X}_{\boldsymbol{k}}) - \varphi_{\boldsymbol{b}}(\boldsymbol{X}_{\boldsymbol{l}})\Big] \cdot \\ \left[\frac{V'(|\boldsymbol{r}_{\boldsymbol{kl}}|)}{|\boldsymbol{r}_{\boldsymbol{kl}}|}\mathbb{I} + \left(\frac{V''(|\boldsymbol{r}_{\boldsymbol{kl}}|)}{|\boldsymbol{r}_{\boldsymbol{kl}}|^2} - \frac{V'(|\boldsymbol{r}_{\boldsymbol{kl}}|)}{|\boldsymbol{r}_{\boldsymbol{kl}}|^3}\right)\boldsymbol{r}_{\boldsymbol{kl}} \otimes \boldsymbol{r}_{\boldsymbol{kl}}\right], \tag{6}$$

which strictly exhibits a symmetric form. Furthermore it can easily be shown that the approximate energy (4) and its gradient (5) match their lattice statics counterparts in the fully atomistic limit (i.e. $\mathscr{L}_h = \mathscr{L}$, $n_{\boldsymbol{i}} = 1$, $\mathcal{C}_{\boldsymbol{i}} = \{\boldsymbol{i}\}\ \forall\, \boldsymbol{i} \in \mathscr{L}_h$).

4 Summary

We have pointed out some drawbacks associated with the force based cluster summation rule described in [2]: (i) the existing approximation of the force functions renders them nonconservative; (ii) without direct link to an explicit potential function, standard optimization algorithms cannot be applied to find the minimizing configurations. The key new aspect in this contribution is, that the same cluster summation rule can advantageously be applied to compute an approximation of the exact total potential energy. From the sampled energy functional the nodal forces are consistently derived preserving their conservative nature and the corresponding symmetry of the global stiffness matrix.

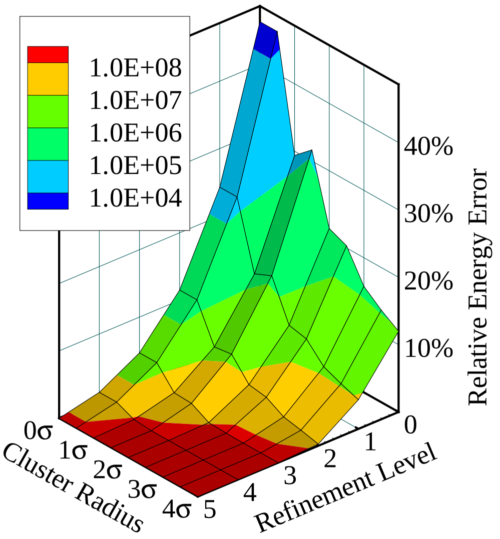

Figure 3: *Energy based cluster summation rule for a cubic block with* $32 \times 32 \times 32$ *fcc cells applying a Lennard-Jones potential: Relative error of the total potential energy compared to the lattice statics solution. Refinement level stands for the density of representative atoms. The colors indicate the computational complexity, that is the number of short-ranged interactions to compute.*

References

[1] E.B. Tadmor, M. Ortiz, and R. Phillips. *Quasicontinuum analysis of defects in solids.* Phil. Mag. A, 73:1529–1563, 1996.

[2] J. Knap and M. Ortiz. *An analysis of the quasicontinuum method.* J. Mech. Phys. Solids, 49(9):1899–1923, 2001.

An examination of local atomic deformation computed by means of a discrete gradient operator

Philip Gullett

Mississippi State University, 235M Walker Engineering, Box 9546, 39759 Mississippi State, United States of America

Among the challenges for hierarchical models is the need to provide a common measure of deformation between atomic scale simulations and the continuum framework. Deformation measures typical in molecular dynamics simulations such as centro-symmetry and the slip vector have proved useful for identifying lattice distortion and the formation of dislocation structures, but correlation in the context of hierarchical modeling is difficult because these measures are not utilized in the continuum framework. A recently introduced kinematical algorithm for the construction of strain tensors from atomistic simulation data by means of a discrete gradient operator has provided a powerful means for computing strain tensors suitable for use in large deformation molecular dynamics/statics simulations. In addition to the strain tensors, a discussion on the plastic spin, velocity gradient, and the distinguishing between the elastic and plastic strain tensors will be presented.

Multiscale Modelling of the Early Stage of Thin Film Deposition --- from ab initio to continuum

QIYANG HU[1], *Nasr M. Ghoniem*[2]

[1]*UCLA, Mathematical Science Bldg, #2000, University of California, 90095 Los Angeles, United States of America*
[2]*UCLA, Mechanical & Aerospace Engr. Dept, University of California, 90095 - 1597 Los Angeles, United States of America*

We investigate here the evolution of self-organized monolayer atomic clusters on atomically fat substrates during epitaxial deposition. Starting from the Bragg-Williams approach, we develop a continuum model in which both short-range and long-range interactions between ad-atoms are included in the free energy in the system. The short-range part of the free energy includes the entropy of mixing and interfacial energy which are in principle determined by ab initio calculations of atomistic interactions. Long-range contributions to the free energy account for interactions between deposited atom clusters mediated by the substrate, and are derived using the elastic theory of intrinsic surface stress. The current model bridges the atomistic and macroscopic scales through a derivation based on statistical physics. The length scale of natural self-organized structures is in the tens of nano-meters. Imposition of a substrate periodic strain feld by subsurface interfacial dislocations is shown to dramatically change the self-organized pattern and its length scale. Qualitative agreements between model predictions and experimental observations on self-organized Ge quantum dots on Si substrates are demonstrated.

Atomistic Simulations of Dislocation-Interface Interactions in the FCC/HCP Incoherent Systems

S. Hara, T. Kumagai, S. Izumi and S. Sakai

Department of Mechanical Engineering, The University of Tokyo, 7-3-1 Hongo, Bunkyo-ku, Tokyo, 113-8656 JAPAN, E-mail: hara.shotaro@fml.t.u-tokyo.ac.jp

ABSTRACT

We have employed molecular dynamics simulations in order to examine the slip resistance of the screw dislocation across coherent and incoherent interfaces in the Cu(111)/Co(0001) and Cu(111)/Ru(0001) bilayer systems. Simulations are performed at various applied strain conditions using newly developed potential parameters based on the generalized EAM functions. The results show that the dominant contribution to the slip resistance at these fcc/hcp interface is not the effect of the modulus mismatch but that of the adrupt core energy change at the interface.

1. Introduction

Epitaxial interfaces act as the source of the slip resistance. In particular, recent experiments suggested that the strength of metallic nanolayered composites is strongly related to the stress that a single dislocation needs to transmit the interface [1]. Previous continuum approach predicted that this interface barrier for slip is attributed to the several factors, such as elastic modulus mismatch (the Koehler effect), lattice mismatch (coherency stress or misfit dislocation effect), and core structure changes at the interface (unstable stacking faults energy mismatch or core spreading in the interface) [2,3]. However, the details of the slip resistance are not understood yet, since these factors depend basically on the atomistic structure [4,5].

In this paper, we study the atomistic details of the slip behavior in fcc/hcp metallic bilayer system, which has not been reported previously. We determine the effective barrier to the transmission of the screw dislocation across this interface.

2. Simulation Methodology

The interactions between atoms are described using the generalized EAM potentials [6]. In this study, to investigate Cu-Co and Cu-Ru bimaterial systems, we have developed new sets of parameters fitted to the properties of Co and Ru. Additionally, to examine the effect of the modulus mismatch, independent the other mismatches, Co_{coh} and Ru_{coh} parameters which predict the lattice constants identical to fcc Cu are also given. Thus, incoherent interfaces (with misfit dislocation) are reproduced using the Cu-Co and Cu-Ru potentials, while coherent interfaces (with no coherency stress) are predicted using Cu-Co_{coh} and Cu-Ru_{coh} potentials.

Fig. 1 shows the initial configuration of dislocation-interface interaction model. Initially, a fcc Cu crystal is placed above a hcp Co or Ru crystal, and the system is relaxed using energy minimizations. The *x*, *y* and *z* axes of the simulation cells are $[10\bar{1}]$, $[1\bar{2}1]$ and [111] direction for the fcc Cu lattice, and $[11\bar{2}0]$, $[\bar{1}100]$ and [0001] direction for the hcp Co or Ru lattice. The interface normal corresponds to the *z* direction. The dimensions of the cell are 10 nm × 35 nm × 20 nm, containing about 600000 atoms. A screw dislocation with the burgers vector ***b*** of (a/2) $<10\bar{1}>$ is introduced in the Cu crystal by displacing the atoms according to the elastic dislocation displacement fields. Periodic boundary conditions are applied along the dislocation line (*x* direction) and the atoms within the outermost four layers from the *y* and *z* faces are fixed. In order to push the screw dislocation toward the interface, a constant shear strain ε_{xy} is applied. The temperature of the system is kept constant at 0.1 K in all simulations. The dislocation motions are visualized by computing the atoms that do not have 12 first neighbors.

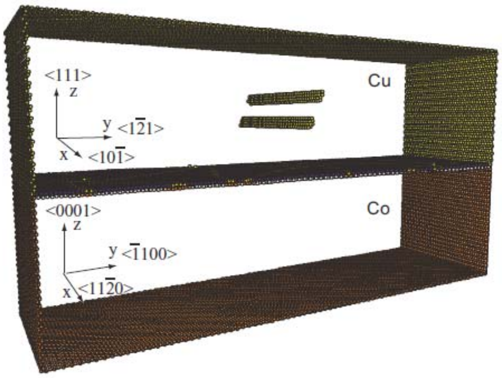

Fig. 1 : Illustration of the dislocation-interface interaction model in Cu-Co system.

3. Simulation Results

3.1 coherent interface systems

The simulation results are summarized in Table 1. A screw dislocation consisting of two Shockley partials is repelled at interface when applied shear strains are below 0.004 (Cu/Co) and 0.01 (Cu/Ru), since Cu is elastically softer material than Co or Ru. At applied strains of 0.007 (Cu/Co) and 0.015 (Cu/Ru), the two Shockley partials are constricted and then cross-slip onto the interface. From these results, we can estimate the Koehler stress due to the modulus mismatch to be about 200 MPa (Cu/Co) and 500 MPa (Cu/Ru) using the resolved shear stress acting on the glide plane in Cu. We also found that these values are in good agreement with those estimated from the continuum theory [2].

At the huge applied strains of 0.084 (Cu/Co) and 0.092 (Cu/Ru), the screw dilocation can transmit into the Co or Ru lattice, with the change in the slip plane orientation from the fcc {111} plane to the hcp $\{10\bar{1}0\}$ prism plane. The energy barrier required to shear the $\{10\bar{1}0\}$ prism plane is so high relative to that of the fcc {111} plane that this misorientation accompanies with the adrupt change in the core energy of the dislocation. As a result, our simulations predict that the effect of the core energy changes on the slip resistance is factor of one order higher than that of the modulus mismatch.

Table 1: Applied shear strain corresponding to the interaction mechanism.

	Cu/Co coherent	Cu/Co incoherent	Cu/Ru coherent	Cu/Ru incoherent
Transmission	0.084 ~	0.084~	0.092~	0.115~
Dissociation into interface	-	~0.082	-	~0.11
Cross-slip	0.007~0.082	-	0.015~0.09	-
Rebound at interface	~0.004	-	~0.01	-

3.2 incoherent interface systems

Fig. 2 shows the atomistic configurations of the glide dislocation moving toward the incoherent interfaces. In Fig. 2, only core atoms are shown. Our simulations show that the glide dislocation reacts with the misfit dislocations spontaneously. Even at the low applied stress, interface containing misfit dislocations attracts the glide dislocation. These results indicate that the misfit dislocations significantly reduce the modulus mismatch effect, since the interface can respond to the stress-field of the glide dislocation by sliding [4]. The other Shockley partials are emitted from the interface into the Cu layer. We find that the misfit dislocations provide the site of the heterogeneous dislocation nucleation.

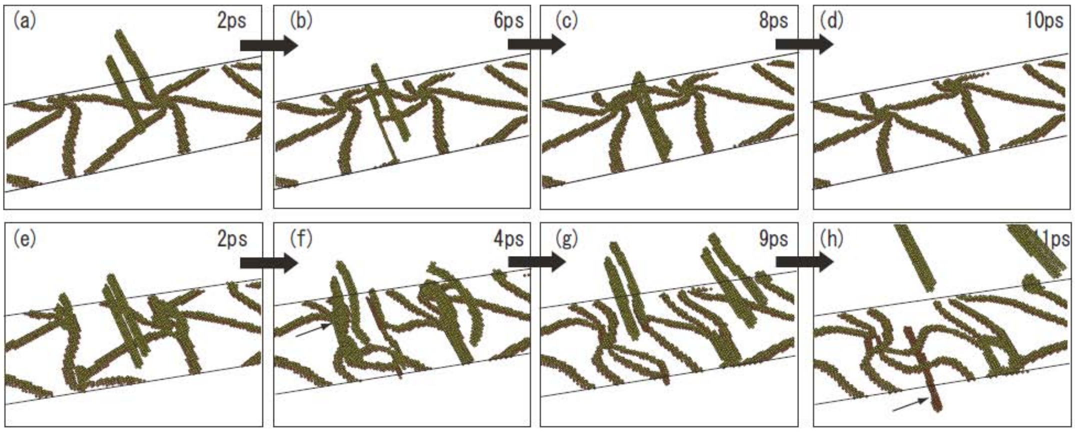

Figure 2: Atomistic configurations of the interaction process between the screw dislocation and the Cu/Co interface containing misfit dislocations. (a)-(d) Two Shockley partials are dissociated into the interface (ε_{xy} = 0.002), (e)-(h) After two Shockley partials are constricted at the interface, the screw dislocation transmits the interface and glides along hcp $\{10\bar{1}0\}$ prism plane. (ε_{xy} = 0.09).

Acknowledgements

The author (S. Hara) was supported through the 21st Century COE Program, "Mechanical Systems Innovation," by the Ministry of Education, Culture, Sports, Science and Technology.

References

[1] A. Misra, J. P. Hirth, R. G. Hoangland, Acta Mater 53, 4817 (2005).
[2] J. S. Koehler, Phys. Rev. B 2, 2 (1970).
[3] P. M. Anderson, Z. Li, Mater. Sci. Eng. A 319, 182 (2001).
[4] S. I. Rao, P. M. Hazzledine, Philo Mag A 80, 2011 (2000).
[5] R. G. Hoagland, R. J. Kurtz, C. H. Henager Jr., Scripta Mater 50, 775 (2004).
[6] X. W. Zhou, H. N. G. Wadley, R. A. Johnson, D. J. Larson, N. Tabat, A. Cerezo, A. K. Petford-Long, G. D. W. Smith, P. H. Clifton, R. L. Martens, T. F. Kelly, Acta Mater. 49, 4005 (2001)

Large-scale atomistic simulations of nanoindentation: Length-scale effects on hardness

Alexander Hartmaier

University Erlangen-Nuernberg, Institute of General Material Properties (WW1), Martensstrasse 5, 90158 Erlangen, Germany

Large-scale molecular dynamics simulations of nanoindentation have been performed to study the influence of different length scales on the contact pressure (hardness of the material). Typical numerical samples contained between 2 and 5 million atoms interacting with an embedded atom potential. The indenter was modeled essentially as a hard sphere with a purely repulsive potential. The indentation was performed in a displacement controlled fashion and at a constant finite temperature. The elastic branch of the load-indentation curves is consistent with the Hertzian contact theory. In the plastic branch of the indentation curve the hardness is found to decrease with indentation depth, whereas the average dislocation density in the plastic zone increases with indentation depth. Strain gradients and Taylor hardening hence cannot explain this size effect in hardness. The origin of the size effect seems to be rather that the indentation is performed into a perfect, dislocation-free single-crystal, where the first dislocations nucleate homogeneously at the theoretical shear strength. Thus the hardness at small indentation depths is high. At larger indentation depths further plastic deformation occurs at comparatively low stresses via multiplication of dislocations. Indentations into crystals with pre-existing defect microstructure (dislocation and grain boundaries) will be performed to test this reasoning.

The influence of electronic structure on a NEMS shuttle

C. Huldt, **J. M. Kinaret**

Department of Applied Physics, Chalmers University of Technology, S-412
96 Göteborg, Sweden; chuldt@fy.chalmers.se

ABSTRACT

The nanoelectromechanical shuttle consists of a double junction with a mobile central island. Above a certain voltage threshold, the strong coupling between electronic and mechanical degrees of freedom can enhance the current using the central island as an electron shuttle. In this work, we combine density functional theory (DFT) calculations with macroscopic dynamics simulations in order to examine the influence of the electronic structure on the IV-characteristics of a molecular shuttle.

1. Introduction

The nanoelectromechanical shuttle resembles a single electron transistor but incorporates mechanical motion of the central island. Previous studies have shown that the central island can absorb energy from a DC applied bias to a shuttling motion enhancing the current of the system [1]. Earlier theoretical works have covered several size regimes, but few have included a realistic discrete level structure of a molecular shuttle. This system requires multiscale modelling due to the combination of molecular dynamics and electronic transport.

The two main issues addressed in this work are the impact of the electronic structure and the interaction between the central island and leads. A microscopic analysis is performed on the electronic structure. Eigenvalues, forces and tunnel rates are derived from these calculations and used in a macroscopic dynamics module featuring classical motion of the central island. The work is a simplification of an earlier study [2] where also the change in the orbitals and eigenvalues with central island position were studied.

2. Method

We employ the adiabatic approximation *for the central island* to decouple the instantaneous electronic structure of the mobile molecule from the nuclear motion and use time-independent DFT to obtain the spectrum and the electronic orbitals. In the shuttling regime, the couplings between the mobile central island and the leads vary over an exponentially large range during the shuttling motion, equilibrium is not established and the adiabatic approximation cannot be applied to the system as a whole. We treat charge transfer between the central island and the leads as instantaneous tunneling events, with tunneling rates that are calculated using the electronic structure of central island. For computational efficiency, we choose a very simple system where the central island is one Cu atom between two jellium electrodes. However, the methods and trends should be applicable also to more complex systems.

In a previous study we carried out the electronic structure calculation for each position and charge state of the central island [2] using the DFT code DaCapo [3]. The computational cost of this approach was quite high despite the simplicity of the system, and prevented a systematic study of the transport properties at different bias voltages. In this study, we simplify the procedure and treat the influence of interactions with leads on the electronic structure of the central island perturbatively. The electronic orbitals of the shuttling molecule are approximated by those of a molecule in vacuum, while the energy spectrum varies with the island position which results in position dependent tunneling rates. The spectrum shift is given by a one-particle potential that describes the interaction between a (possibly charged) molecule and the metallic leads. We use a fit function introduced by Jones *et al.* [4] of the form

$$V_J(z) = -\frac{q^2}{16\pi\epsilon_0(z-z_0)}(1-e^{-\lambda(z-z0)}) \quad z \geq z_0 \tag{1}$$

to describe the potential of one electron outside a metal surface where λ and z_0 are fitting parameters to be determined. For the interaction with the induced charge from the remaining charges of the system we use the same damping term as in Eqn (1)

$$V_R(Z) = -\frac{q^2}{4\pi\epsilon_0}\left(\frac{Q_v(1-e^{-\lambda(Z-z_0)})}{2(Z-z_0)} - (Q_e-1)\int d\mathbf{r}\frac{1-e^{-\lambda z}}{\mid \mathbf{Z}-\mathbf{r}\mid}\frac{1}{(2\pi\sigma^2)^{3/2}}e^{-(\mathbf{Z}-\mathbf{r})^2/2\sigma^2}\right) \tag{2}$$

where the second term takes into account the spatial distribution of electrons. Here, Q_e and Q_v are the number of valence electrons and pseudopotential charge respectively and Z is the position of the atom core. The forces on the system are derived from the system energy related to the equations above and a short-range repulsion derived from a Born-Mayer potential.

Charge transfer rates are calculated with the transfer Hamiltonian method [5]. Transition rates are calculated for two positions of the island, which determines the constants in an exponential ansatz for the specific transition rate. The derived functions for the forces and transition rates are used as parameters in a dynamics module. The motion of the central island is classic with the force term from above and a dissipative force term based on phonon emission to the leads. The transition rates are employed for dynamic Monte Carlo calculations that determine time points for charge state transitions.

3. Results

The island spectrum obtained by the perturbative approach agrees well with the results of the previous study in which the spectrum was calculated for each island position [2]. Deviations are seen at positions closest to the leads as can be expected due to the orbital deformation observed previously [2].

The strong dependence of the spectrum on island position and total charge, Q, results in a complicated Coulomb-blockade-type behavior in a qualitative agreement with earlier shuttle studies. However, the spectrum of the island leads to some deviations from the phenomenological Coulomb blockade picture — for instance, it results in an asymmetry in involved charge states: transitions to negative island charges are energetically allowed only for bias voltages above 4V. The system can still shuttle as long as $\overline{\dot{z}Q} > 0$ along one direction of the shuttle motion.

The onset of shuttling depends somewhat on the initial conditions. If the starting setup for the island is neutral and stationary in the middle of the gap, the shuttling will start first when an electron tunnel off. For small bias voltages the island is physisorbed near one of the leads and shuttling does not occur. For voltages that exceed a threshold voltage, which for the system studied here lies between 1V and 2V, a stable shuttling regime is quickly established. For bias voltages between 2V and 3V, only charge states $Q = 0$e and $Q = 1$e are dynamically active, even though transitions to $Q = 2$e are energetically possible. Thus only one electron is transferred per period. The current-voltage characteristics can be seen in Fig. (1).

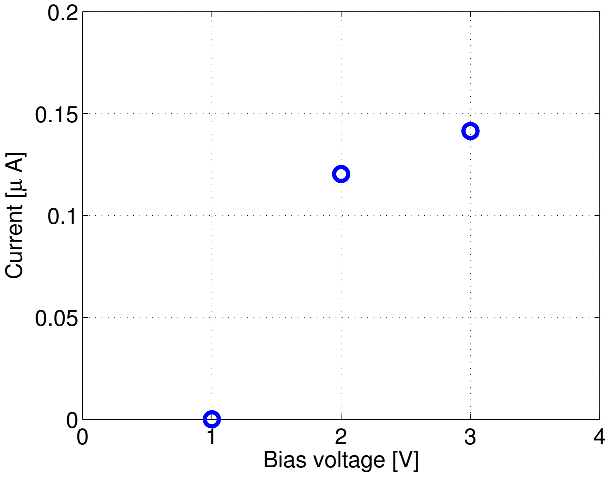

Figure 1: The current-voltage characteristics for our shuttle model. The threshold voltage for entering the shuttling regime is between 1V and 2V.

The complexity of the energy spectra creates unexpected characteristics. Close to the negative lead an electron tunnels on, off, and on again giving a small boost in forces toward the other lead. For the previous model, this sequence of events happened occasionally [2], in this study it is the default behavior. These differences in properties are due to small changes in the energy spectra for positions near the leads. However, when the system enters the shuttling regime, the motion and current seem to be very predictable.

In the end, the simplified model gives satisfying results as compared with the previous study. However, both studies show that the close-range behavior near the leads demand a very careful treatment due to rapidly changing orbitals, energy spectra and forces, which are all important for the shuttling behavior.

Acknowledgements

This work was supported in part by the European Community FP6 funding through the CANEL project, contract no. FP6-2004-IST-003673.

References

[1] R.I. Shekhter *et al.*, J. Phys.: Condens. Matter, **15**, R441 (2003).
[2] C. Huldt and J.M. Kinaret, cond-mat/0606086 (2006).
[3] www.fysik.dtu.dk
[4] R. O. Jones *et al.*, Phys. Rev. B, **29**, 6474 (1984).
[5] J. Bardeen, Phys. Rev. Lett., **6**, 57 (1961).

Development and Application of Hybrid Fast-Coarse-Grained-Particle/Molecular-Dynamics Simulation Method

Takahiro Igarashi[1], Shuji Ogata[2,3] and Takashi Tsukada[1]

[1]Research Group for Corrosion Damage Mechanism, Nuclear Science and Energy Directorate, Japan Atomic Energy Agency, igarashi.takahiro@jaea.go.jp;
[2]Graduate School of Engineering, Nagoya Institute of Technology;
[3]CREST, Japan Science and Technology Agency

ABSTRACT

A novel hybrid continuum-atomistic approach for accurate simulation of a large-scale nano-structured system is proposed. In the approach, a target system is partitioned into the continuum and atomistic regions in which the continuum region gives the boundary condition to the atomistic one. The total computation cost may be reduced significantly without scarifying the physical accuracy. We adopt the fast-coarse-grained particle method (FCGP) for the continuum description, which we develop by modifying the coarse-graining method proposed originally by Rudd and Broughton [Phys. Rev. B 58, R5893 (1998)] to be applicable directly to large-scale systems. The FCGP method is suited to its hybridization with an atomistic simulation method such as the classical molecular dynamics (MD) method since the inter-particle interaction reduces automatically to the original inter-atomic one near the particle-atom boundary if we decrease the degree of coarsening near the boundary. The FCGP and MD methods are hybridized with introduction of the buffer atoms at the boundary. The hybrid FCGP-MD simulation scheme is applied successfully to various nano-structured systems. We discuss the advantages of the present hybrid method from the viewpoints of physical accuracy and calculation cost.

1. Introduction

Various processes in materials, such as stress corrosion cracking, involve chemical reaction of constituent atoms and impurity atoms. In order to obtain the fundamental mechanisms of such processes, it is efficient to consider atomistic discussion. Such microscopic phenomena can be investigated with the atomistic simulation method[1]. However, even with a recent high-performance computer, direct atomistic treatment of the nano-device is impractical. Therefore, to theoretically analyze and design useful devices with nano-scale structures, we need to hybridize the continuum and atomistic simulation methods. In such a concurrent hybridization approach, the target system is partitioned into regions and various calculation methods such as the electronic structure calculation, the classical atomistic calculation, and the continuum method, are applied appropriately to the regions.

In this paper, we aim at the development and application of the hybrid continuum-atomistic simulation scheme: (1) We modify a coarse-graining method to formulate the fast coarse-grained particle method appropriate to large-scale simulation. Various numerical results obtained by the present method are compared with that obtained by full-atom calculations, to find reasonable agreement and shorter computation times in the present method. Through such comparisons, we clarify the physical meaning of the inter-particle interaction energy in the present method. (2) We propose a simple scheme to hybridize concurrently the present method with an atomistic one. (3) An application of the hybrid simulation scheme is demonstrated.

2. Fast Coarse-Grained Particle (FCGP) Method

In the coarse-graining method developed originally by Rudd and Broughton [2], virtual particles are distributed in the system and the inter-particle interaction is calculated through the constrained statistical average of the atomic Hamiltonian over the atomic phonons at the classical limit. The method has several worthy features. To note but a few, at the same coarse-graining level, the method has a higher accuracy than the finite element method since it includes finite-temperature effects from the first principles. The method is also suited to its hybridization with an atomistic method since the inter-particle interaction reduces automatically to the original inter-atomic one with the phonon approximation at the lowest-level of the coarse-graining.

On the other hand, the coarse-graining method has drawbacks. Since the process of coarse-graining contains the inverse calculation of the dynamical matrix of the total atomistic system, the $O\left(N_{\mathrm{atom}}^{3}\right)$ operations are required with the total number of atoms N_{atom}. Also, since the coarse-grained Hamiltonian is a function of displacements of particles from their equilibrium positions, the Hamiltonian may not be used directly for a moving or deformed system.

To overcome, we formulate the fast coarse-grained particle (FCGP) method by modifying the coarse-graining method: (1) We consider a small super-cell to calculate the inter-particle interactions, which are used extensively for the inter-particle interactions at other regions of the target system. It corresponds to introducing the cutoff wavelength to the atomistic phonons. (2) We rewrite the inter-particle interaction formula to that of the inter-particle separation vectors by exploiting the sum rule of the dynamical matrix. (3) We modify the inter-particle interaction formula to make it rotationally invariant. The inter-particle interaction energy E_{FCGP} in the FCGP method is thereby written as

$$E_{\mathrm{FCGP}} = -\frac{1}{2}\sum_{(i,j)}^{\mathrm{pairs}}\sum_{r,s}^{\mathrm{axes}}\left(R'_{(i,j),r} - R^{(0)}_{(i,j),r}\right)K_{(i,r),(j,s)}\left(R'_{(i,j),s} - R^{(0)}_{(i,j),s}\right), \tag{1}$$

where subscripts *i,j,...* and *r,s,...* represent the labels of the particles and Cartesian axes, respectively. The $R'_{(i,j),r} \equiv \sum_{s}^{\mathrm{axes}} Q_{r,s}^{(i,j)} R_{(i,j),s}$ is the inter-particle separation vector seen in the rotated frame with the matrix $Q_{r,s}^{(i,j)}$ which rotates the pair of particles-*i* and *j*. The $R_{(i,j),r} \equiv X_{(j,r)} - X_{(i,r)}$ is the *r*-element of inter-particle separation vector with the *r*-element of absolute position of particle-*i* $X_{(i,r)}$. The $R^{(0)}_{(i,j),r}$ is the original value of $R_{(i,j),r}$. The $K_{(i,r),(j,s)}$ is the element of stiffness matrix of the FCGP system and obtained as $\mathbf{K} = \left(\mathbf{f}\mathbf{D}^{-1}\mathbf{f}^{\mathrm{T}}\right)^{-1}$, where **D** is the dynamical matrix for the inter-atomic interaction potential used in the molecular dynamics (MD) of atoms and **f** corresponds to the weight of each atom on a particles in the coarse-graining procedure.

3. Hybridization of FCGP and MD

We hybridize concurrently the FCGP and MD methods. Since the FCGP Hamiltonian reduces automatically to the atomic one with the harmonic approximation at the lowest coarse-graining level, there is no difficulty in hybridizing. We adopt the modular approach with the buffered-cluster method [3]. For a FCGP system that includes multiple regions with different coarse-graining levels, a super-cell is considered for each coarse-grained region to get the stiffness and mass matrices.

As a demonstration, we consider the propagation of density waves in a hybridized system composed originally of Ar atoms; the total system assumes a thin board in shape with size (*x*,*y*,*z*)~(110Å,28Å,8Å). As shown in Fig. 1, about 25% of the total system from the right-end is the atomistic region, and about 50% from the left-end is the coarse-grained region. In between the regions, the lowest-level coarse-grained region (*i.e.*, each atom corresponds to each particles) is set. In the simulation run, we hit the right-end of the system at time zero by a hard-core atom with mass 1 a.u. and initial velocity 0.4Å/fs. In the right panels of Fig. 1, we depict the displacements of atoms/particles in the total system at 4ps, 6 ps, and 8 ps after the hitting, which are compared with the full-atom simulation results in the left panels. No artificial behavior is observed in the hybridized system through comparison with the full-atom result. We may suppose that that the present hybridization scheme has sufficient accuracy to be applicable to various nanoscale systems.

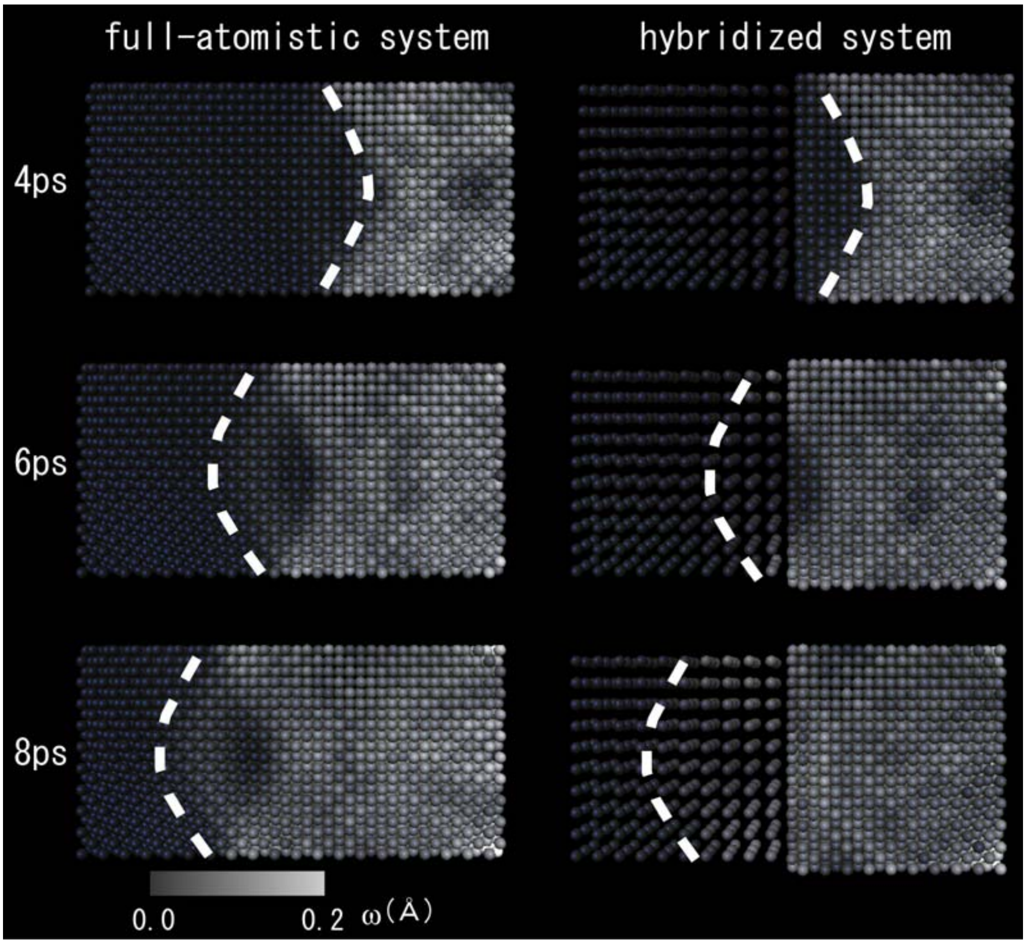

Figure 1. (Left) the displacements of atoms in the full-atom system at 4 ps, 6 ps, and 8ps after hitting the right-end at time 0. (Right) same as (left) but in the hybridized system. The dashed curves represent the front of density waves.

4. Summary

In this paper, we have proposed a novel coarse-graining method called the FCGP method that is applicable directly to large-scale systems. The hybrid FCGP-MD simulation scheme has been formulated. As a demonstration, the propagation behavior of density wave in the hybrid system of a thin-board has been investigated. We thereby have obtained the results that are in good agreement with that in the corresponding full-atom results.

Acknowledgements

The authors acknowledge ACT-JST and Grant-in-Aid for Scientific Research of the Ministry of Education, Science, Sports, and Culture of Japan (No. 16605005). T.I. was supported in part by Grant-in-Aid for the 21th Century COE (Nagoya University).

References

[1] A. Nakano, M.E. Bachlechner, P. Branicio, T.J. Campbell, I. Ebbsjö, R.K. Kalia, A. Madhukar, S. Ogata, A. Omeltchenko, J.P. Rino, F. Shimojo, P. Walsh, and P. Vashishta, Large Scale atomistic modeling of nanoelectronic structures, IEEE Trans. Electr. Dev. 47, 1804 (2000).
[2] R.E. Rudd and J.Q. Broughton, Coarse-grained molecular dynamics and the atomic limit of finite elements, Phys. Rev. B 58, R5893 (1998).
[3] S. Ogata, Buffered-cluster method for hybridization of density-functional theory and classical molecular dynamics: Application to stress-dependent reaction of H_2O on nanostructured Si, Phys. Rev. B 72, 45348 (2005).

Influence of Impurity Atoms on the Rate of Solid Phase Epitaxy: Molecular Dynamics Study

Satoshi Izumi[1], Katsunari Murai, Shotaro Hara, Tomohisa Kumagai, and Shinsuke Sakai

[1]Department of Mechanical Engineering, The University of Tokyo, 7-3-1 Hongo, Bunkyo-ku, Tokyo, JAPAN 113-8656, izumi@fml.t.u-tokyo.ac.jp

ABSTRACT

In this study, we investigated the effect of arsenic atoms on the rate of Si SPE by using molecular dynamics simulation. In the case of non-doped Si, activation energy of SPE is found to be 2.1 eV±0.5eV, which shows good agreement with the experimental result (2.7 eV). It is also found that the energy barrier of crystallization in a/c interface amounts to be about 0.6eV, which corresponds to defect migration process. It indicates other processes such as defect formation also control the SPE process. The SPE rate increases by 2 times for 3 at% As doping and 100 times for 5 at% As doping and an activation energy remains to be constant. The increase in SPE rate would be enhanced by defect formation process in amorphous silicon, which reflects the increase in self-diffusion of silicon atoms caused by active As atoms.

1. Introduction

Solid phase epitaxy (SPE) of Si is one of the most fundamental processes in semiconductor fabrication techniques. Many experimental studies have been carried out for understanding the growth mechanism. However microscopic mechanism is not well understood. In this study, we investigated the effect of arsenic atoms on the rate of Si SPE by using molecular dynamics simulation.

2. Analysis Method

2.1. SPE simulation of non-doped silicon

For Si-Si interaction, Tersoff potential [1], which can describe amorphous silicon well, is employed. Here, a-Si/c-Si(001) interface is modeled as shown in Fig. 1. Amorphous silicon is well-relaxed through 10 ns annealing at 1600 K. Periodic boundary conditions are applied to all xyz directions. The system is annealed at constant volume and constant temperature conditions. In order to clarify the effect of temperature on the SPE rate, simulations at various temperatures ranging from 1500 K to 2300 K are carried out.
In order to detect the crystallized region, bond-angle deviation is employed as is proposed by our previous report [2].

2.2. SPE simulation of As-doped silicon

For As-As interaction, potential parameters proposed by Smith [3] are employed. For Si-As interaction, averaging rules proposed by Tersoff and verified by Nakamura [4] is applied. As concentrations of 2, 3, and 5 at % are employed so as to see the dependence of impurity concentration on SPE rate.

3. Result

3.1. SPE simulation of pure silicon

The dependence of SPE rate on temperature is shown in Fig. 2. The results are averaged over 3 samples. As can be seen, SPE rate shows thermal activation process. Its activation energies amount to 2.1eV±0.5eV at low temperature region and 0.7eV±0.2eV at high-temperature region, which show good agreement with experimental results (2.7 eV and 0.7-1.1 eV, respectively). It also shows smooth transition from low to high temperature region. It is noted that a melting point of the Tersoff amorphous silicon is about 1900 K. Therefore, the epitaxy above 1900 K must be called as liquid phase epitaxy (LPE).
From nudged elastic band analysis, it is found that the energy barrier of crystallization in a/c interface amounts to be about 0.6eV. Since that barrier is close to that of LPE, it might correspond to defect migration energy in a/c interface. It also indicates that other processes such as defect formation also control the SPE process.

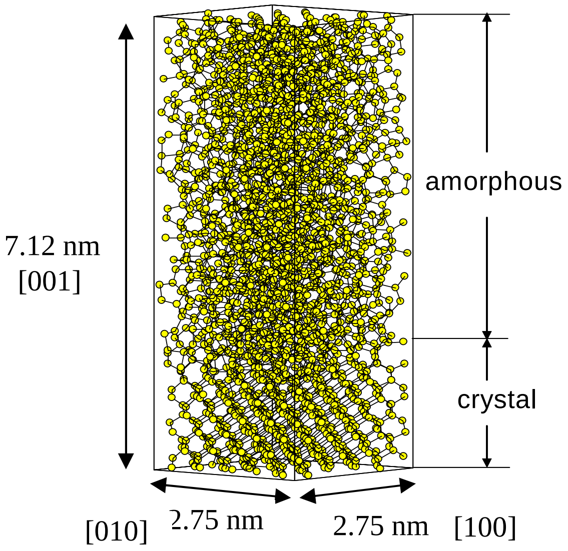

Figure1. Schematic view of a/c interface model

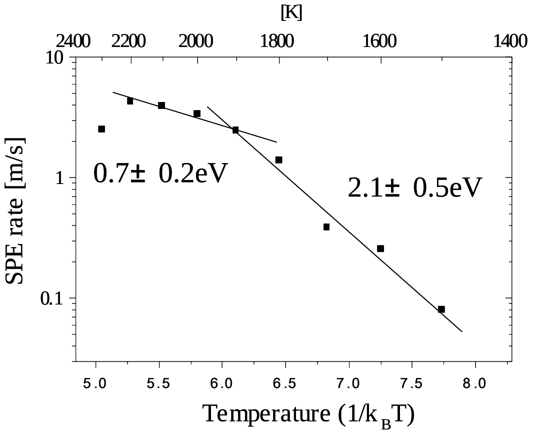

Figure.2 Dependence of SPE rate on temperature (average of three samples)

3.2. SPE simulation of As-doped silicon

SPE rate of As-doped silicon is shown in Fig. 3. The SPE rate increases by 2 times for 3 at% As doping and 100 times for 5 at% As doping and an activation energy remains to be constant. At each doped concentration, the deviation from the Arrhenius plot can be observed at high temperature region. Especially, SPE rate decreases in case of 5 at% above 1300K.

4. Discussion

Fig. 4 shows the dependence of self-diffusion constant of silicon atoms on temperature under various As concentration. It can be seen that self-diffusion is significantly enhanced by As doping. Therefore, the increase in SPE rate would be enhanced by the defect formation process caused by active As atoms in amorphous silicon.

At high temperature region, self-diffusion constant of As doped silicon reaches that of undoped amorphous silicon at its melting point. Therefore, transition from SPE to LPE would induce the deviation from the Arrhenius plot. Moreover, in case of 5 at% over 1300 K, the self-diffusion of doped silicon exceeds that of undoped crystal silicon at its melting point. As a result, the competition between crystallization and melting appears in a/c interface. That would induce the decrease in SPE rate.

In Csepregi’s experiment [5], SPE rate is enhanced by about 10 times at 0.5 at% doping. That quantitative deviation might be caused by the accuracy in interatomic potentials, e.g. the accuracy in reproduction of activation energy.

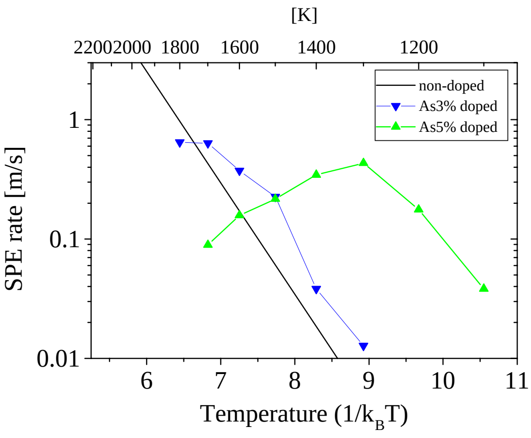

Figure.3 Dependence of SPE rate on temperature under various As-doping concentrations

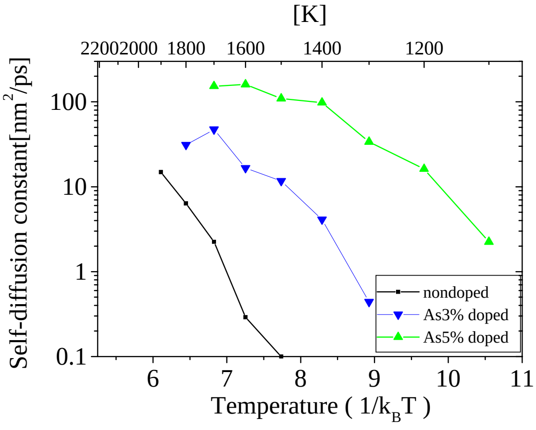

Figure.4 Dependence of self-diffusion constants of silicon atoms on temperature under various As concentration

5. References

[1] J.Tersoff, Phys. Rev. B39, 5566 (1989).
[2] S. Izumi, S. Hara, T. Kumagai, S. Sakai, Comp. Mat. Sci. 31, 258 (2004), 279 (2004).
[3] R. Smith, Nucl. Instr. and Meth.in Phys. Res. B 67, 335 (1992).
[4] M. Nakamura, H. Fujioka, K. Ono, M. Takeuchi, T. Mitsui, M. Oshima, J. Crystal Growth 209, 232 (2000).
[5] L. Csepregi, E.F. Kennedy, T.J. Gallagher, J.W. Mayer and T.W. Sigmon, J.Appl. Phys.48, 4234 (1977).

Mechanical Properties and Defect Structures of Nanoscale Materials by AB Initio Molecular Dynamics and Temperature Lattice Green's Function Methods

K. Masuda-Jindo[1], Vu Van Hung[2], N. T. Hoa[2] and M. Menon[3]

[1] Department of Materials Science and Engineering,
Tokyo Institute of Technology, Nagatsuta, Midori-ku, Yokohama 226-8503, Japan
[2] Hanoi National Pedagogic University, km8 Hanoi-Sontay Highway, Hanoi, Vietnam
[3] Department of Physics and Astronomy, University of Kentucky, Lexington, Kentucky 40506, U.S.A.

ABSTRACT

The nucleation and propagation processes of dislocations and cracks in nanoscale materials are studied using the ab initio constraint molecular dynamics (c-MD) method and the lattice Green’s Function method. We investigate the strength and fracture behaviors of carbon related nanoscale materials, especially the graphen sheets and carbon nanotubes (CNT) in comparison with those of BN nanotubes and Si, SiC nanowires. The temperature dependence of linear elastic parameters, nonlinear elastic instabilities, thermal lattice expansion and fracture behaviors are studied in detail.

1. Introduction

Recently, there has been a great interest in the study of nanoscale materials since they provide us a wide variety of academic problems as well as the technological applications [1,2]. CNT's have been thus identified as one of the most promising building blocks for future development of functional nanostructures. Now, it has been observed that the introduction of lattice defects and mechanical deformation influence quite significantly on the electronical properties of nanoscale materials. The purpose of the present paper is to investigate the strength and fracture behaviors of nanoscale materials using the ab initio tight-binding molecular dynamics method and the temperature Lattice Green's function method [3]. We calculate the atomic configurations and strength properties of nanomaterials using the new version of the molecular dynamics method, constraint molecular dynamics (c-MD) method, on the basis of the analysis by the Lattice Green's function theory.

We shall also study the thermodynamic and electronic properties of nanoscale materials including the temperature dependence of lattice spacing and the resulting changes in the interatomic force constants.

2. PRINCIPLE OF CALCULATIONS

For treating mechanical properties of nanoscale materials we will use the ab initio tight-binding molecular dynamics methods [7,8], which have been very successful in the calculations of various chemical and physical properties of nanoscale materials. In the present article, we also use the constraint MD method combined with the lattice Green’s function (LGF) approach to study the initiation of microcracks in the nanoscale materials, like graphene sheets, nanographites and nanotubes. In the treatment of LGF, we generalize the conventional LGF theory to take into account the temperature effects by including the temperature dependence of force constant matrices and non-linear cohesive forces.

In the LGF treatments, the so-called bond annihilation operations play an important roles in the crack initiation and opening processes of the "double" ended cracks. In the use of the mathematical terminology, the bond annihilation operators correspond to the "perturbation potential" V in the Dyson equation:

$$G = G_0 + G_0 V G, \tag{1}$$

where G_0 and G represent the unperturbed and perturbed Green's functions, respectively. We will combine the concepts of the conventional LGF method with the numerical analysis by the molecular dynamics method to get the "equilibrium" crack geometries under the external loadings.

3. RESULTS AND DISCUSSIONS

The calculated thermal expansion coefficients and Young’s moduli of CNTs are shown in Fig.1, as a function of the temperature. One sees in Fig.1 that the thermal expansions and elastic properties depend strongly on the type of CNT. It is interesting in Fig.1 that the Young’s moduli of CNT containing dislocations (characterized by 5/7 defects), dot-dashed lines, are smaller than those containing no dislocations and SW defects. In Fig.1c, we also present the specific heats C_v at constant volume of CNTs, as a function of the temperature. The calculated C_v values of CNTs are given in unit of the Boltzmann constant k_B, and compared with those of the bulk materials. One can see in Fig.1c that the calculated specific heats C_v (k_B) depend sensitively on the type of CNTs, except for the (6,6) CNT, having very similar temperature dependence to the diamond cubic crystal.

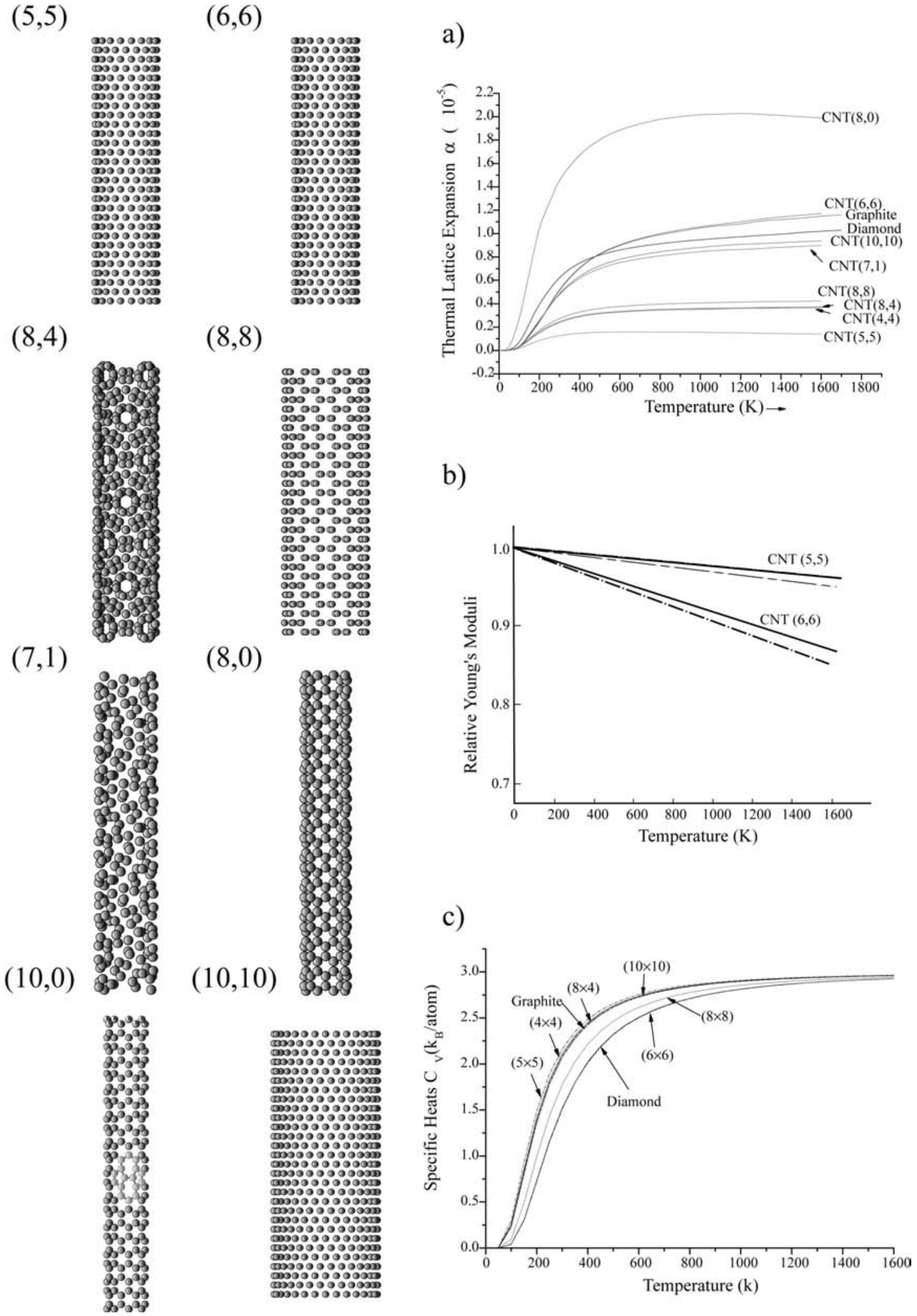

Fig.1 Thermal lattice expansion coefficient α, specific heats and the Young's moduli of CNTs.

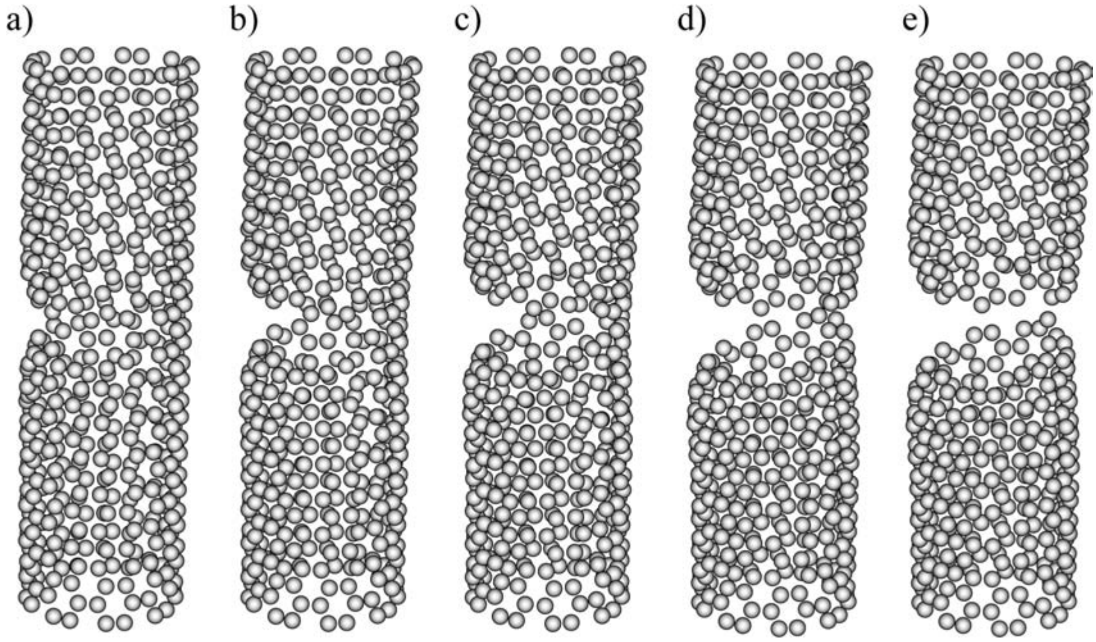

Fig.2 Nucleation and propagation of microcracks and the resulting fracture of (10,10) carbon nanotubes.

We have studied using c-MD method, the initiation and propagation of the micro-cracks in the CNTs originated from the SW defects. The atomic configurations of the CNTs including SW defects, i.e., 5/7/8/8/7/5 type defects are shown in Fig.2. In Fig.2, we present the atomistic configurations of the double ended cracks initiated from SW defects (5/7/8/8/7/5 type) in (10,10) CNT, slightly higher than the critical tensile strain. One can see that the double ended cracks is clearly trapped in the "lattice" of (10,10) CNT. In Fig.2, we also present the crack propagations and fracture of (10,10) CNT, calculated under the mode I tensile loadings considerably higher than the critical ("Grifith") strain of $\varepsilon_c \sim 0.12$. Here, we present the atomic configurations of the (10,10) CNTs, including the double ended cracks, initiated from the 5/7/8/8/7/5 type of SW defects. The sufficiently high external loadings are applied to the CNT, and one can observe the CNTs are broken into two pieces, after the sufficient MD simulations.

Finally, we have calculated the atomic configurations of the double ended cracks in the cleavage plane of the 2D graphen sheets, under applied tensile stresses. In this calculation, we have assumed that the certain bonds across the cleavage plane are broken at the initial stage of MD relaxation processes. After the sufficient MD simulations, however, no assumptions on the bond breakings are made for the whole crystallites. This is a spirit of our constraint MD scheme. Using such MD procedure, one can get the stable equilibrium cracks in the crystallites, which are essentially the similar results as those obtained by the analytic LGF method. As in the infinite three dimensional crystals, the double ended cracks are trapped in the small crystallites at certain mode I loadings. However, upon the increase of the mode I loading to some extent, the micro cracks do extend, by one atomic distance, to the next stable positions.

In Fig.3, we present the atomic configurations of the double ended cracks in the graphen sheets, slightly higher than the critical "Grifith" tensile loadings. One sees in Fig.3 that the double ended cracks propagate to both surfaces of the graphens and the "specimen" separates into two speices. The "strain energies" are monitored for every 10 MD steps. The strain energies of graphen sheets including the cleavage crack are reduced rapidly at the initials stage of the MD processes. Here, it is important to note that the surface excess energies γ due to the cleaved surface in the crystallites are approximately constant during the initial stage of the c-MD calculations, even when the crack opening displacements are nearly zero, since the "bond annihilation" operations are active from the begging of the calculations. This is one of the advantages of the c-MD approach in the analysis of crack problems. From the middle to the final stages of c-MD simulations, the reduction of strain energies corresponds to the changes in the elastic and surface energies.

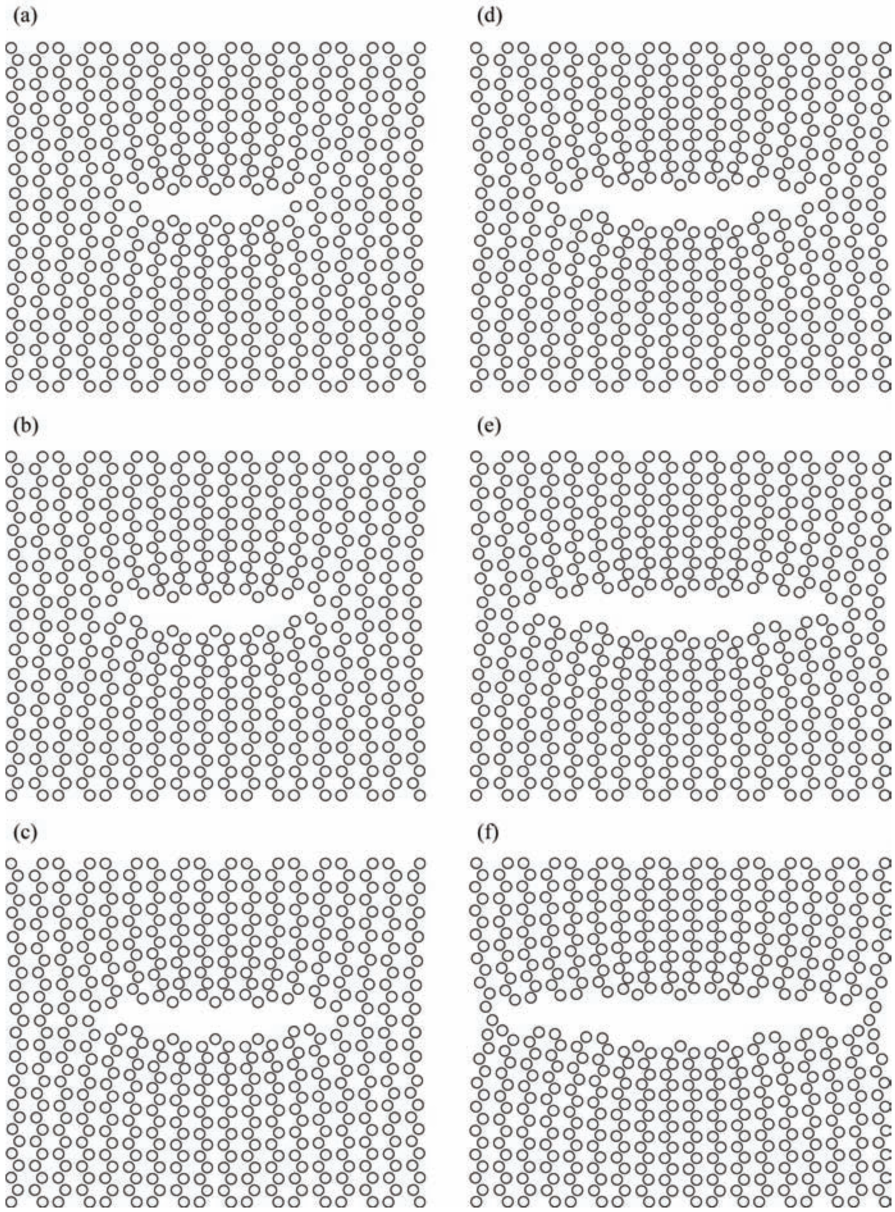

Fig.2 Crack extension events (a)~(f) in graphen sheets.

REFERENCES

1. S. Iijima, Nature **354** (1991) 56.
2. K. Masuda-Jindo and R. Kikuchi, Int. J. of Nanoscience, **1**, (2002) 357-371.
3. K. Masuda-Jindo, Vu Van Hung and M. Menon, Int. J. Fracture, **125** (2006) 1-18.
4. K. Masuda-Jindo, Vu Van Hung and Pham Dinh Tam, Phys. Rev. **B67** (2003) 094301.
5. K. Masuda-Jindo, S. R. Nishitani and Vu Van Hung, Phys. Rev. **B70** (2004) 184122.
6. K. Masuda-Jindo, Vu Van Hung and M. Menon, phys. stat. sol.**(c)2**, No.6 (2005) 1781.
7. Vu Van Hung, K. Masuda-Jindo and Pham Thi Minh Hanh, J. Phys. Condens. Matter **18** (2006) 283.

Multiscale computational strategy through coupling

Marco Kalweit[1], D. Drikakis[1]

[1]Fluid Mechanics and Computational Science Group, Cranfield Universiy, School of Engineering, Department of Aerospace, MK43 0AL, Cranfield, United Kingdom

The development of multiscale computational strategies are of interest due to the wide range of applications relating to micro and nanotechnology. Even though every one agrees that any material (fluid or solid) is a collection of molecules, the continuum approximation is still sufficiently accurate to describe a number of physical circumstances. However, as the spatial scales become smaller, accuracy on the basis of the continuum approximation can be compromised. Molecular dynamics (MD) and its variants can then be used as an alternative (see [1] for a recent review), but then one is concerned with the associated computing requirements to solve a problem. Even using the most powerful massively parallel computations [2] cannot address in great detail all the processes and phenomena occurring above nano-scales.

The simultaneous use of continuum and molecular methods in studying problems featuring multiple scales can be useful in a variety of ways: (i) MD can model systems with time-and spatial scales that are orders of magnitude below the continuum approximation. They can, therefore, provide information in regimes in which continuum approximations are not valid any more. (ii) Depending on the application problem, continuum methods may still provide accurate simulations for time scales on the order of 5m and 5sec. Therefore, in a variable scale environment there is no reason to resort to expensive particle methods throughout the computational domain. (iii) In geometrical configurations in which the separation of length scales is obvious, coupling of continuum and molecular strategies is the best way forward. (iv) All equilibrium properties such as pressure and internal energy are essentially averages of microscopic interactions. These averages are embedded in the calculation of the transport coefficients, which in turn are required in the simulations at continuum level. (v) MD simulations require density, pressure, and temperature values as initial and boundary conditions to proceed with the computations. The continuum simulations can provide this data. Effectively, one can create a dynamic feedback between microscopic and macroscopic scales that is general and that can be applied to a wide variety of problems.

The aim of this paper is to present a computational strategy that is based on the geometrical coupling of continuum and molecular simulation methods. We use computational fluid dynamics (CFD) methods to describe the continuum motion of a fluid material and molecular dynamics methods to describe the molecular nature of solid or liquid material. Geometrical coupling is obtained through a hybrid solution interface (HSI), as shown in Figure 1). This provides a meso scale modelling strategy, which is essentially based on the transfer of computational data between CFD and MD. The coupling strategy is general and applicable in connection with finite element methods as well.

The HIS contains an overlapping region between CFD and MD. Within this region particles will be supplied, aiming at relaxing the boundary conditions in a way that continuity of the mass and momentum fluxes is obtained. The coupling strategy comprises several steps including: supply of particles in the continuum region that are averaged in space and time. This achieves continuity of mass flux as well as providing the velocity boundary conditions for the hydrodynamics simulation.

(ii) In the vicinity of the HSI, an artificial force field, acting in the direction normal to the boundary, is applied to the outermost particles, with the aim of relaxing primitive continuum variables at the interfaces, e.g., density in the vicinity of the HIS and terminating the spatial extent of the MD region. (iii) The continuity of the momentum flux is obtained by achieving continuity of the stresses at the HSI, which poses a computational challenge because the MD model does not use a constitutive equation of the stress but explicitly calculates it, taking into account the momentum flux of molecules across a surface element as well as the forces between molecules on the sides of the surface elements.

The meso scale modelling strategy is validated against benchmark cases for which analytical solutions are available. Results pertinent to more complex problems are also presented demonstrating the potential of method.

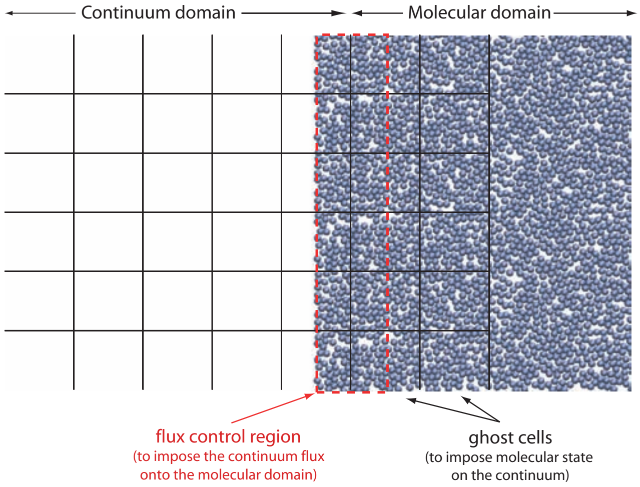

Figure1: Illustration of the hybrid solution interface between continuum and molecular domains

References

[1] D. Drikakis and M. Kalweit. Computational Modelling of Flow and Mass Transport Processes in Nanotechnology, to be published in, Handbook of Theoretical and Computational Nanotechnology, (eds. M. Rieth, W. Schommers), American Scientifc Publishers, 2006.

[2] K. Kadau, T.C. Germann, and P.S. Lomdahl, Large-ScaleMolecular-Dynamics Simulation of 19 Billion particles, Int. J. Mod. Phys. C, 15, 193, 2004

Collision Dynamics of Nanoparticles

Marco Kalweit[1], *D. Drikakis*[1]

[1]*Fluid Mechanics and Computational Science Group, Cranfield Universiy, School of Engineering, Department of Aerospace, MK43 0AL, Cranfield, United Kingdom*

Particles collisions are important for a broad range of processes including growth and aggregation of particles in technical sprays; surface treatment and coating; sintering during which bulk material is generated through inter particle collisions, where the properties of the material depend strongly on the shape of the coalescence or agglomerated articles; growth, handling and utilisation of atomic and molecular clusters, particularly as applied in cluster beams, where the growth of clusters is driven by monomer addition and cluster coalescence. Previously experimental [1,2,3] and numerical investigations [4,5,6] have been performed aiming to derive analytical prediction models for macroscopic droplets. At nanoscale, the atomic structure of the particles becomes important, since the particles consist of a few hundred or thousand of atoms. At present, these scales are not directly accessible by experiments, hence, numerical simulations become even more important. Quantum mechanical methods such as the density functional theory (DFT) would give the most accurate results, but they are computationally very expensive and can only be applied to small clusters. Molecular dynamics (MD) methods based on phenomenological potential functions to model interatomic interactions, have turned out to be an excellent tool for conducting numerical experiments at small scales. Continuum methods would reduce the computational efort even further, but they are not valid in the nanoscale range. A limited number of numerical investigations based on molecular dynamics methods have been performed in relation to collision of nanoparticles [7,8,9]. These studies aimed to identify the collision modes as well as to examine the applicability of macroscale models to nanoparticles. It was shown that even though macroscopic models are applicable to certain collision modes, further investigation is required to cover a broader range of scales. In this paper, an investigation of collision dynamics of nanoparticles for a broad range of impact factors and collision speeds is presented (Figure1). The investigation is based on molecular dynamics simulations in conjunction with the Lennard-Jones interaction potential thus making the results applicable for a broad range of material properties. Identifcation criteria are used to classify the collision dynamics into diferent collision modes and submodes. Detailed analysis of the collision processes reveals the existence of coalescence and stretching separation modes, which are further classifed according to their dynamics into sticking; slide-and-locking; droplet; normal stretching separation; stretching separation with satellite droplets; and shearing-ofmodes. Qualitative and quantitative comparisons with previous molecular dynamic studies and analytical prediction models derived for macroscopic droplet collisions, are also discussed.The investigation reveals that the refexive separation mode, which has been observed in macroscopic droplet collisions, does not occur for nanoparticles consisting of 10,000 (or less) atoms.

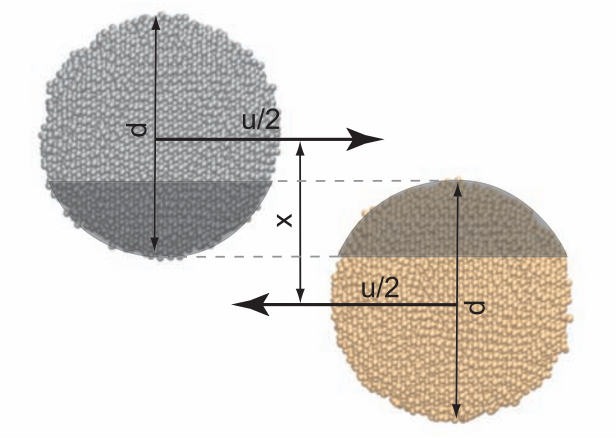

Figure1: Initial setup for the binary collision of two nanoparticles, where d is the particle diameter, X/d is the impact factor and u is the impact speed.

References

[1] Ashgriz, N. & POO, J.Y.1990 Coalescence and separation in binary collision of liquid drops. J. Fluid Mech. 221, 183204.

[2] Qian, J. & Law, C.K. 1997 Regimes of coalescence and separation in droplet collision. J. Fluid Mech. 331, 5980.

[3] Brenn, G., Valkovska, D. & Danov, K.D. 2001 The formation of satellite droplets by unstable binary drop collisions. Physics of Fluids 13, 24632477.

[4] Schelke, M. & Frohn, A.1995 Three-dimensional lattice boltzmann simulations of binary collisions between equal droplets. J. Aerosol Sci. 26, 145146.

[5] Pan, Y. & Suga, K. 2005 Numerical simulation of binary liquid droplet collision. Physics of Fluids 17, 082105082119.

[6] Mele1n, Y. & Sigalotti, L. D. G. 2005 Coalescence of colliding van der waals liquiddrops. Int. J. Heat Mass Transfer 48, 40414061.

[7] M. Kalweit & D. Drikakis, 2004 Molecular Dynamics of Colliding Nanoclusters, Journal of Computational and Theoretical Nanoscience, 4, 367-377.

[8] Ming, L. , Markovic, N. , Svanberg, M. & Petterson, J. B. C. 1997 Collision dynamics of large argon clusters .J .Phys. Chem. A 101, 40114018.

[9] Svanberg, M., Ming, L., Markovic, N. & Pettersson, J. B. C. 1998 Molecular dynamics simulations of binary collisions between water clusters. J. Chem. Phys.108, 58885897.

Dislocation Core Properties Near Cu/Ni Interface: A Hybrid Atomistic-Continuum Study

Mutasem Shehadeh[1], Gang Lu[1], Sauvik Banerjee[2], Nickolas Kioussis[1] and Nasr Ghoniem[3]

[1]Department of Physics and Astronomy, California State University, Northridge, CA 91330-8268(mutasem@csun.edu, gang.lu.35@csun.edu, nick.kioussis@csun.edu)
[2]Engineering Technology Department, Saint Louis University, Saint Louis, MO 63103, (sbanerje@slu.edu)
[3]Department of Mechanical and Aerospace Engineering, University of California, Los Angeles, CA 90095

ABSTRACT

The strengthening mechanisms in bimetallic Cu/Ni thin layers are investigated using a hybrid approach that links the parametric dislocation dynamics-based on Peierls-Nabarro (PN) method-with ab initio calculations. The model takes into account all three components of atomic displacements of the dislocation and utilizes the entire generalized stacking fault energy surface (GSFS) to capture the essential features of dislocation core structure. The hybrid model shows that the dislocation dissociates into partials in both Cu and Ni, and the dislocation core is squeezed near the interface facilitating the spreading process, and leaving an interfacial ledge.

1 Introduction

In recent years, there has been considerable interest in the mechanical and structural properties of metallic multilayer systems, which display remarkably high mechanical strength and hardness comparable to their theoretical strength [1]. The dramatic enhancement of multilayer strength has been generally attributed to the following factors: the mismatch in the elastic properties which results in image forces on the dislocation, the mismatch in the GSFS between incoming and outgoing planes which plays a major role in determining the core properties of the dislocation, the mismatch in the lattice parameters that leads to the generation of coherency stress across the interface, and the GSFS of the interface which may suppress or enhance the spreading of the dislocation core from the glide plane to the interface. Continuum elasticity models [2,3]and molecular dynamics simulations (MD)[4,5] have been used extensively to investigate the mechanical response of multilayerd materials. However, the elasticity models cannot describe the image forces accurately as it diverges in the vicinity of the dislocation core. In order to overcome this difficulty, an arbitrary cut-off radius, r_0, is generally introduced but its actual value is highly uncertain. Consequently, important quantities, such as the critical stress required to make the dislocation cross the interface, are not accurately determined unless r_0 is “calibrated” with atomistic calculations. On the other hand, MD simulations suffer from the lack of reliable empirical potentials for treating interatomic interactions across the interface [6], especially when one considers new materials for which empirical interatomic potentials are not available. We have developed an extension of the PN model which integrates the atomistic nature from ab initio electronic structure calculations to study the core properties of a pure screw dislocation as it moves from Cu to Ni.

2 PN Model for the Cu/Ni Interface

In this approach, the full dislocation is represented by a set of N fractional Volterra dislocations with fractional Burgers vector db=b/N. In the case of a pure screw dislocation a sufficient amount of edge components is added by introducing N/2 positive and N/2 negative fractional edges. The equilibrium structure of the dislocation core is obtained by seeking the equilibrium configuration of these fractional dislocations. Physically, this corresponds to balancing the elastic force and the lattice restoring force derived from the ab initio determined GSFS across the glide plane. In general, the total force on a fractional dislocation has contributions from the externally applied stress, the stresses exerted from other fractional dislocations located in Cu, on the interface, and in Ni, the lattice restoring force derived from the GSFS, and finally the coherency stress. The equilibrium position of each fractional dislocation is computed according to:

$$F_i^T = B\frac{dx_i}{dt} \tag{1}$$

where B is a drag coefficient to update the position x_i of the dislocation at each time step.

3 Results and Discussion

The ab initio-determined GSFS projected along the $[121]$ direction for the pure Cu and Ni and along the [001] direction for the Cu/Ni interface are shown in Fig 1. The first energy maximum encountered along the $[121]$ direction for the Cu and Ni is the unstable stacking fault energy which represents the lowest energy barrier to nucleate a dislocation from a crack tip. The local minimum on the other hand, corresponds to the intrinsic stacking fault energies. The GSFS of the interface on the other hand is symmetric with no saddle point suggesting that the full dislocation on the interface does not dissociate. Fig. 2 shows the equilibrium edge and screw displacement and the corresponding Burgers vector density ρ(x) of the dislocation for two values of applied stress. The edge and screw Burgers vector density are defined by $\rho_e(x) = du_e/dx, \text{and}\, \rho_s(x) = du_s/dx$. The screw dislocation, originally placed in the soft material (x>0) is pushed towards the Cu/Ni interface. For relatively low values of applied stress (around 2.0 GPa), the dislocation core in Cu dissociates into two partials bounding a stacking fault with a separation distance of about 7b. As the external stress increases, the dislocation approaches the interface but remains dissociated. However; the dislocation core structure has changed significantly. First, the dislocation Burgers vector density accumulates on the leading partial at the expense of the trailing partial. Second, the dislocation core constricts steadily and the two partials overlap significantly. Note, that the maximum value of the screw component of the displacement in Cu is 2.4 Å, while the Burgers vector of Cu is 2.6 Å. This reduction of Burgers vector is a result of the energetically favorable spreading of the core onto the interface. Our results suggest that the dislocation spreading process proceeds via the following mechanism: When the leading fractional dislocation reaches the vicinity of the interface it spreads on it, if it is energetically favorable. As the external stress is increased, the trailing fractional dislocations follow and spread onto the interface. The spreading process continues until the interface can no longer accommodate additional slip. At the critical value of the applied stress, once the leading dislocation is transmitted to the Ni crystal, the remaining ones follow.

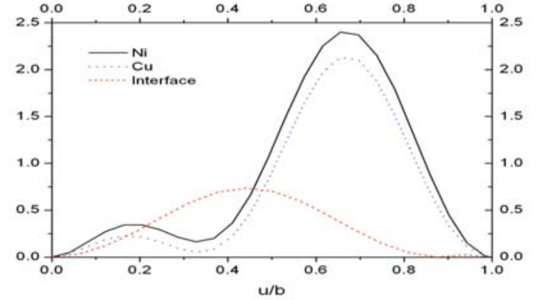

Figure 1: Projections of the ab initio GSFS for Ni and Cu and the interface.

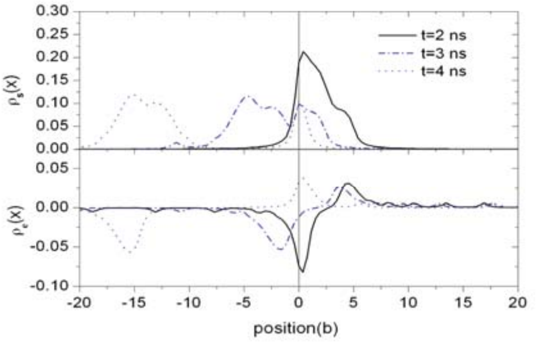

Figure 3: Dynamic evolution of the dislocation burgers vector density during the threading process at the critical transmission stress of 3.35 GPa.

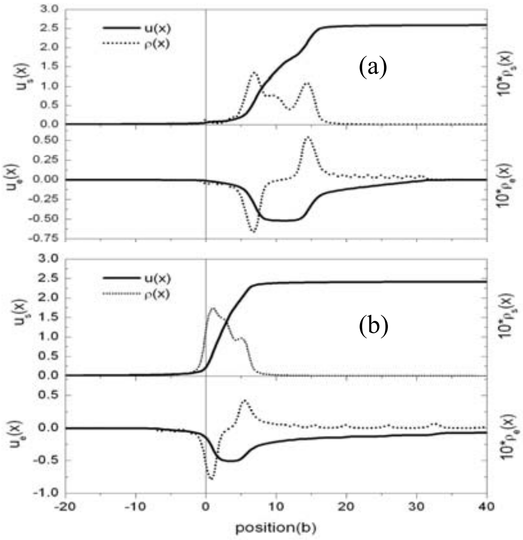

Figure 2: The displacement u(x) and density ρ(x) profiles for the dislocation as it moves from Cu towards Ni (a) 2.0 GPa, (b) 2.8 GPa. The continuous (dotted) curves denote the screw or the edge displacements (densities).

In Fig. 3 we show the time evolution of the Burgers vector density profiles $\rho_s(x)$ and $\rho_e(x)$ of the dislocation when the applied stress has reached its critical value of 3.35 GPa. At the initial stage of the dislocation threading process, most of the fractional dislocations are localized in the vicinity of the interface in the Cu host. As the fractional dislocations relax, they get transmitted through the interface towards the Ni host till all of them pass. Note that after the dislocation gets transmitted, the density profile shows the formation of two partials with a separation distance of about 6b. The peak in the density profile at x=0 indicates the formation of a ledge on the interface, in agreement with MD simulations for edge or mixed dislocations for the Cu/Ni interface [5].

References

[1] A. Misra, J.P. Hirth and H. Kung, Phil. Mag. *A*, **82,** 2935 (2002).
[2] X. Han and N. M. Ghoniem, Phil. Mag, **85,** 1205 (2005).
[3] A. K. Head, Proc.Phys.Soc.LXVI, **9-B,** 793 (1952).
[4] R. G. Hoagland, T. E. Mitchell, J. P. Hirth, and H. Kung,. Phil. Mag, **82,** 643 (2002).
[5] I. Rao, and P. M. Hazzledine, Phil. Mag A, **80,** 2011 (2000).
[6] G. Schoeck, Acta Materialia, **49** 1179 (2001).

Study of the Grain Size Dependence of Plasticity in Thin Films using Discrete Dislocation Plasticity

R. Kumar[1], **L. Nicola**[2], **V.S. Deshpande**[3], **A. Needleman**[2], **E. Van der Giessen**[1]

[1]**University of Groningen, Dept. of Applied Physics, Nyenborgh 4, 9747 AG Groningen, The Netherlands;** [2]**Brown University, Division of Engineering, Providence, RI 02912, USA;** [3]**Cambridge University, Dept. of Engineering, Trumpington Street, Cambridge CB2 1PZ, UK.**

ABSTRACT

Two-dimensional discrete dislocation plasticity simulations are carried out for polycrystalline freestanding thin films subjected to uniaxial tension. Plastic flow is modeled by tracking explicitely the nucleation, glide, pinning of dislocation at obstacles and dislocation annihilation. Grain boundaries are assumed to act as impenetrable barriers to dislocations.

1. Introduction

In bulk metals, the Hall–Petch relation correlates yield strength to grain size. As specimens get thinner to the scale of micrometres, strength also becomes a function of specimen size. The two size effects, i.e. due to grain size and specimen size, are interrelated but in a yet unknown way. The recent development of experimental testing methods on thin films is key to understanding this in a quantitative manner [1, 2].

As a supplement, we here present numerical simulations of two-dimensional discrete dislocation plasticity in polycrystalline thin films under tension. The ratio of film thickness and grain size is varied to consider the range from bulk Hall–Petch behaviour, as studied in [3], down to thin films with only one or two grains across the thickness [2].

2. Model and simulation method

The model we adopt is similar to that described in [2] and in [4]. Films of thickness h are considered that consist of rectangular grains of the same height d and the same aspect ratio, Figure 1. Moreover, the films are taken to be periodic in their microstructure so that only a periodic cell of width $2L$ needs to be analyzed. We specify the cell width by fixing the grain aspect ratio and the number of grains across the film thickness. The top and bottom faces, $x_2 = 0, h$, are traction free and tension is imposed via periodic boundary conditions at $x_1 = 0$ and $x_1 = 2L$ with a superimposed displacement jump $2U$. Thus, the applied strain is $\varepsilon = U/L$ and the overall tensile stress is denoted by σ.

All grains are elastically isotropic and have three potentially active slip systems, Figure 1. When the number of grains across the thickness is large, the specimen behaves as a bulk material, while a single crystal response is obtained by having only a single grain covering the specimen. In the initial state, the grains are assumed to be stress and dislocation-free, but to contain a given distribution of Frank-Read sources and point obstacles. The sources generate dislocation dipoles once the resolved shear stress on them is larger than their critical strength for a given time span. The obstacles pin dislocations as long as the Peach-Koehler force does not exceed the obstacle strength. Dislocations glide is taken to be completely drag controlled. Dislocations can annihilate and leave the specimen through its free surfaces. Grain boundaries are taken to act as infinitely strong obstacles for dislocation motion.

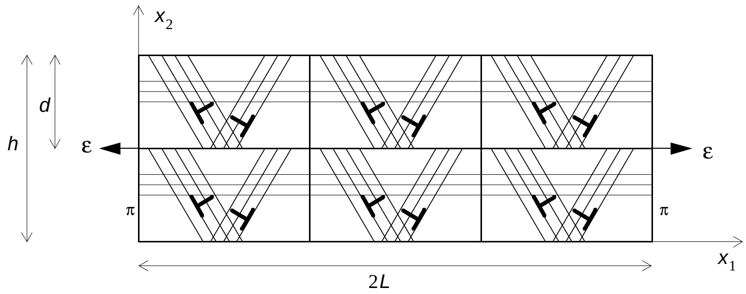

Figure 1: Sketch of the uniaxial tension boundary value problem analyzed. The symbols π identify the periodic boundaries. In this schematic all grains have the same orientation, but in the computations the grain orientations are random.

The geometrical length scales in the problem are: thickness h, grain size d and grain aspect ratio. The relevant material length scales are: the average source spacing, $1/\sqrt{\rho_{\mathrm{nuc}}}$, and the average obstacle spacing, $1/\sqrt{\rho_{\mathrm{obs}}}$, where ρ_{nuc} and ρ_{obs} are the source density and obstacle density, respectively. The length of the Burgers vector $b = 0.25\,\mathrm{nm}$ and the spacing between active slip planes, $200b$, are too small compared to the other length scales to be significant.

3. Results

The simulation results of a polycrystalline film of finite size depend on the distribution of sources and obstacles per grain but also on the grain orientations. For the infinitely long films studied here, it is therefore important to establish the minimum unit cell width which gives cell-width independent results for a given film thickness. To this end, computations have been performed for one layer films, $h = d$, comprising various numbers of grains with the same aspect ratio but different grain orientations. For each cell width, multiple realizations are analyzed. Figure 2 shows the predicted yield strength, $\bar{\sigma}$, versus the number of grains. We found that the scatter in yield strength is higher than 25% when there are four or fewer grains across the cell width. Above about eight grains per cell there is still some scatter (which requires multiple realizations to be done for meaningful results) but the average value is independent of cell width, if the film thickness is $0.5\,\mu$m or larger. Figure 2 also confirms that the yield strength

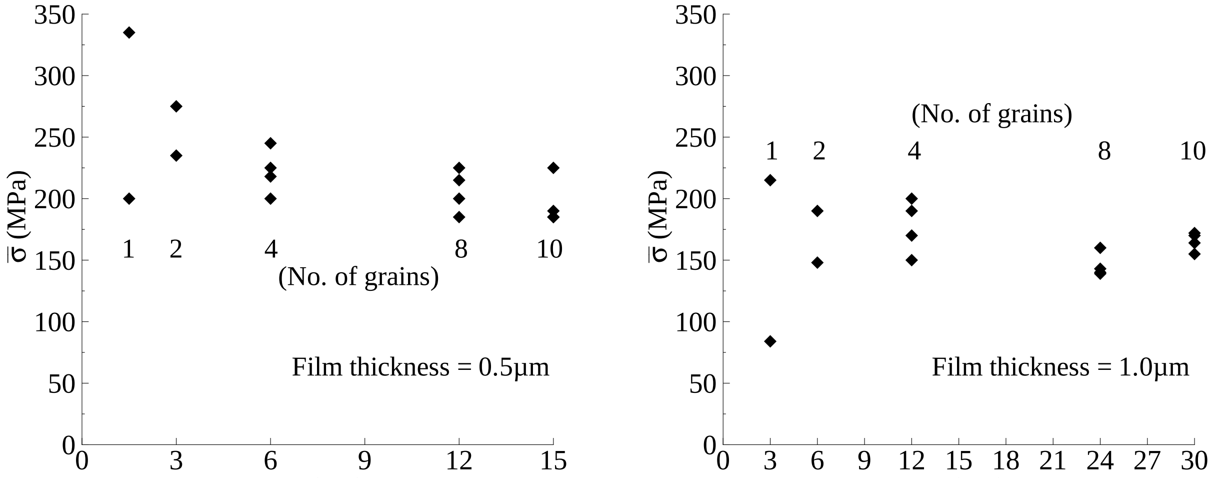

Figure 2: Yield strength $\bar{\sigma}$ versus cell length for one layer films comprising different numbers of grains, with (a) $h = 0.5\,\mu$m and (b) $h = 1\,\mu$m. The grain aspect ratio is 3.

increases with decreasing film thickness, which has been attributed in [2] to the role of the grain boundaries.

Figure 3 shows stress-strain curves obtained for one layer and two layer films of the same thickness, i.e. $h = 2\,\mu$m. We observe a decrease in strength in the two layer film compared to the one layer film. One possibility is that the decrease is due to the activation of sources in one layer caused by the stress field of dislocation piled up in the other layer against the interface between the two, which is consistent with the explanation of the Hall–Petch effect in bulk polycrystals in [3]. However, the dislocation density in the two films during loading is very similar. Moreover, since the films in Fig. 3 differ in source distribution and slip plane orientation, the difference observed in the stress–strain response could depend on the particular realizations chosen. Additional simulations need to be performed in order to reach a better understanding of the governing mechanism.

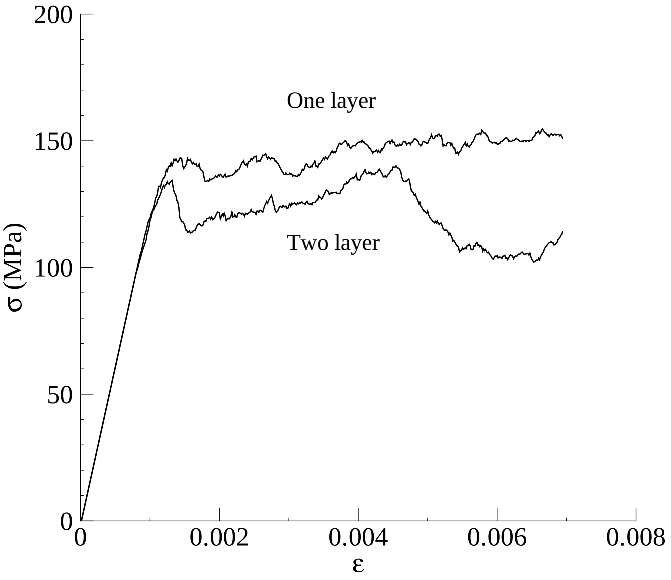

Figure 3: Overall stress-strain curves for a one layer ($h = d$) and a two layer ($h = 2d$) film. Both films have thickness $h = 2\,\mu$m and the unit cell contains eight grains.

References

[1] H.D. Espinosa, B.C. Prorok, and B. Peng, J. Mech. Phys. Solids, **52**, 667 (2004).

[2] L. Nicola, Y. Xiang, J.J. Vlassak, E. Van der Giessen, and A. Needleman, J. Mech. Phys. Solids, in print (2006).

[3] D.S. Balint, V.S. Deshpande, A. Needleman, and E. Van der Giessen, Mat. Sci. Eng. A, **400-401**, 186 (2005).

[4] D.S. Balint, V.S. Deshpande, A. Needleman, and E. Van der Giessen, Modelling Sim. Mat. Sci. Engin., **14**, 409 (2006).

SIZE EFFECT IN THE FLOW STRESS OF SINGLE-CRYSTAL MICROBEAMS DURING BENDING: A DISLOCATION DYNAMICS STUDY

Javier LLorca [1], *Ignacio Romero* [2], *Javier Segurado* [2]

[1] *Polytechnic University of Madrid, E. T. S. de Ingenieros de Caminos, Ciudad Universitaria, 28040 Madrid, Spain*
[2] *Department of Materials Science & Computational Mechanics Group, Polytechnic University of Madrid, E. T. S. de Ingenieros de Caminos., 28040 Madrid, Spain*

Ultra-thin beams have been widely used in micro-electro-mechanical systems (MEMS), sensors and actuators. The thickness of these beams ranges typically from submicrons to ten microns. Within this range, metallic materials display strong size effects. For example, Stolken and Evans (1998) observed a significant increase in plastic work hardening as the beam thickness decreased from 50 to 12.5 µm in the microbend tests of Ni. More recently, Motz et al. [2] found an increase in the flow stress from 300 MPa to 1 GPa in Cu single crystals as beam size decreased from 7.5 to 1.0 µm. In order to elucidate the origin and features of this size effect in the flow stress, the bending of a cantilever microbeam in plane strain was analyzed using discrete dislocation plasticity, following the framework developed by Needleman and Van der Giessen [3]. At each stage of loading, superposition is used to represent the solution in terms of the infinite medium solution for the discrete dislocations and a complementary problem to enforce the boundary conditions, which is obtained from a finite element simulation. The influence of the mechanical (boundary conditions, loading type) and microstructural factors (crystal orientation, slip systems available, etc.) on the size effect was analyzed, and the results in terms of load-deflection curves, dislocation structures and slip band formation are discussed for beams of different depth, providing a rationale to understand the size effect on the flow stress during bending of cantilever microbeams.

[1] J.S. Stolken and A.G. Evans, A microbend test method for measuring the plasticity length scale. Acta Mater. 46 (1998), pp. 5109–5115.

[2] C. Motz, T. Schöberl and R. Pippan, Mechanical properties of micro-sized copper bending beams machined by the focused ion beam technique, Acta Mater. 53 (2005) 4269–4279.

[3] E. Van der Giessen and A. Needleman, Discrete dislocation plasticity: a simple planar model. Model. Simul. Mater. Sci. Eng. 3 (1995) 689–735.

A Micromechanical Study of the Effect of Grain Size and Strain Rate on the Yield Strength of Nanostructured Materials

Ricardo A. Lebensohn[1], **Eduardo M. Bringa**[2] **and Alfredo Caro**[2]

[1]**Materials Science and Technology Division, MS G755, Los Alamos National Laboratory, MS 755, NM 87545, USA (lebenso@lanl.gov).**
[2]**Computational Material Sciences, P.O. Box 808, L-367, Lawrence Livermore National Laboratory, CA 94550, USA (ebringa@llnl.gov, caro2@llnl.gov).**

ABSTRACT

We present a micromechanical approach based on Fast Fourier Transforms to study the role played by dislocation glide and grain boundary (GB) accommodation in the determination of the plastic behavior of nanostructured materials. Under quasiestatic conditions, assuming diffusion-controlled mechanisms at GB, the model predicts a strain-rate sensitivity increase in nanocrystalline samples with respect to the coarse-grained material of the same order as in recently published experiments.

1. Introduction

The yield strength of polycrystalline materials depends strongly on their grain size. For aggregates with grains in the micron range and above, the yield stress increases inversely with the square root of the grain size. At these grain sizes, the highly disordered GB regions represent only a negligible volume fraction of the material. On the contrary, when the grain dimensions approach nanometer sizes, the volume fraction of GBs become significant and the GB regions start to play an active role in accommodating deformation (e.g. [1]). Given the highly disordered character of the GB regions, the microscopic mechanisms associated with GB activity are intrinsically different from the ones associated with plastic deformation by dislocation motion that takes place in the bulk of the grains. A sound constitutive equation of GB deformation would not involve directionality, as it is indeed the case of the usual constitutive description of crystal plasticity. Also, due to the short range of the interactions involved in GB accommodation, the stress required to activate this mechanism should be essentially independent of the grain size of the aggregate [2]. Furthermore, the constitutive equations that describe dislocation glide in the bulk of the grains and accommodation at GBs will have, in general, different sensitivities to temperature and strain rate. A constitutive micromechanical model incorporating such sensitivities would be able to capture the interplay and competition between bulk and GB mechanisms for a particular topology of these nanostructured aggregates. Such a model could be used as a predictive tool to obtain the mechanical behavior of the aggregate, and its sensitivity to different deformation conditions and/or microstructural changes.

2- Model

In this work we report a new micromechanical formulation to study the effect of grain size, pressure and strain rate on the yield strength of fcc nanocrystalline materials. The proposed model is a full-field approximation that takes into account the actual topology of the aggregate consisting in bulk crystalline regions surrounded by a GB percolating phase. Both regions co-deform plastically according the following constitutive behaviors: a) for grain interiors: crystal viscoplasticity, with Hall-Petch grain size dependence; b) for grain boundaries: isotropic viscoplasticity with flow stress independent of grain size. The length-scale of the problem is given by the GB thickness, taken to be 1 nm. A very efficient approach based on the Fast Fourier Transform (FFT) algorithm is used to solve the mechanical problem (e.g. [3]). This FFT-based solution of a unit cell problem for a representative volume element (RVE) gives the local mechanical fields that develop inside heterogeneous materials in great detail. Periodic boundary conditions, required for this type of spectral approximation, are sufficient for the kind of parametric study that we want to perform. In the present case, the unit cell represents an aggregate of single crystal grains with prescribed orientations, surrounded by outer layers of percolating grain boundary regions. The particular orientation of each single crystal determines different anisotropic plastic properties from grain to grain, while, due to its intrinsic disordered character, the GBs are assumed to have a homogeneous isotropic behavior throughout the interconnected “GB phase”. A 3-D implementation of the FFT-based method requires to discretize a cubic unit cell using a regular grid of NxNxN Fourier points (FPs). In this work we adopted N=128, resulting in 2097152 discretization points. Each FP belongs either to a grain interior, or to the GB phase. The dimensions of such Fourier grid are large enough such that each grain and the GB phase are represented by a large number of Fourier points. The length-scale associated with the RVE is determined by the GB thickness, taken to be 1 nm. In order to study the effect of grain size without interference of other microstructural characteristics (like crystallographic texture, or any particular orientation correlation between neighbor grains) four self-similar RVEs were generated of grain sizes 29, 15, 7 and 5 nm (for details, see [4]).

The local constitutive equation for a Fourier point $\mathbf{x}$ belonging to a grain interior is given by the following power law for single crystal viscoplasticity:

$$\dot{\boldsymbol{\varepsilon}}(\mathbf{x}) = \dot{\gamma}_o \sum_s \boldsymbol{\mu}^s(\mathbf{x}) \left(\frac{\left|\boldsymbol{\mu}^s(\mathbf{x}) : \boldsymbol{\sigma}(\mathbf{x})\right|}{\tau_o^s} \right)^{n_{GI}} \times \mathrm{sign}\left[\boldsymbol{\mu}^s(\mathbf{x}) : \boldsymbol{\sigma}(\mathbf{x})\right] \qquad (1)$$

where $\dot{\boldsymbol{\varepsilon}}(\mathbf{x})$ and $\boldsymbol{\sigma}(\mathbf{x})$ are the local strain rate and stress tensors; $\boldsymbol{\mu}^s(\mathbf{x})$, $\dot{\gamma}^s(\mathbf{x})$, $\tau^s(\mathbf{x})$ and τ_o^s are, respectively, the orientation-dependent Schmid tensor, the shear rate, the resolved shear stress, and a reference shear stress, of slip system (s). The pre-factor $\dot{\gamma}_o$ is a reference shear rate, and n_{GI} is an exponent, which can be associated with the inverse of the rate-sensitivity of the coarse-grained material. The local constitutive behavior for a Fourier point $\mathbf{x}$ belonging GB phase is here assumed to be given by the following J_2-isotropic power law for nonlinear isotropic materials:

$$\dot{\boldsymbol{\varepsilon}}(\mathbf{x}) = \frac{3\dot{\varepsilon}_o}{2\sigma_{eq}(\mathbf{x})}\left(\frac{\sigma_{eq}(\mathbf{x})}{\sigma_o}\right)^{n_{GB}} \boldsymbol{\sigma}(\mathbf{x}) \qquad (2)$$

where $\sigma_{eq}(\mathbf{x})$ and σ_o are the von Mises equivalent of the stress and a reference equivalent stress, respectively, $\dot{\varepsilon}_o$ is a reference strain rate, and n_{GB} is an exponent, which can be identified as the inverse of the rate-sensitivity associated with the deformation mechanisms of GB accommodation. For the grain-size dependent value of τ_o^s and the grain-size independent value of σ_o, we followed the work of Bringa et al [5] and references therein (see [4] for details). Moreover, we adopted $n_{GI} = 50$ and $n_{GB} = 1$. This value of n_{GI} corresponds to a rate-sensitivity of the coarse-grained (CG) material $m_{CG} = 1/n_{GI} = 0.02$. The latter is compatible with warm deformation of fcc materials (e.g. m=0.025 for CG Al deformed at 250 °C [6]).

3- Results

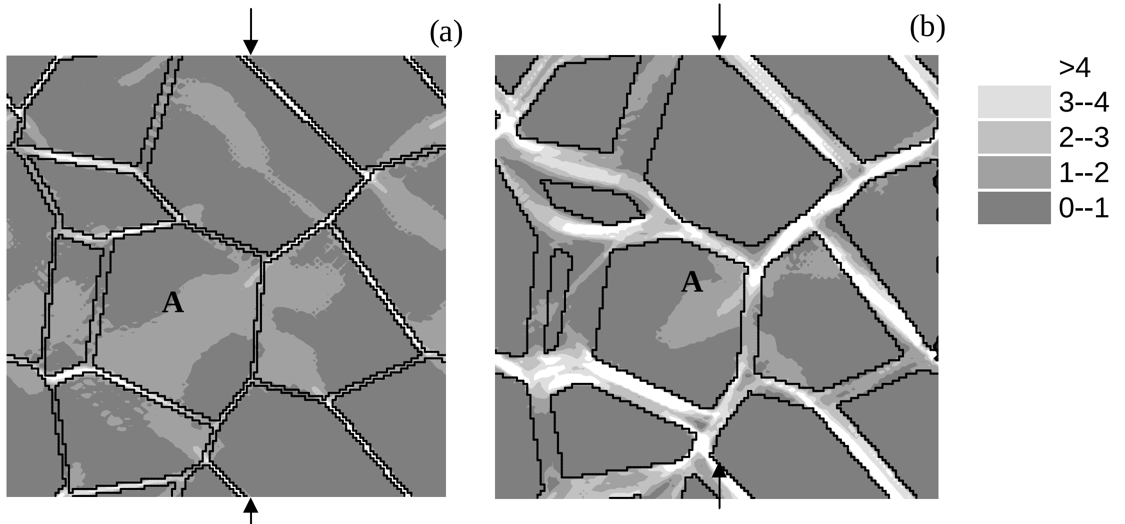

Figure 1: Predicted 2-D section maps (YZ plane at X=64) of local von Mises equivalent strains, relative to the applied macroscopic von Mises equivalent strain, for axisymmetric compression along the z-axis, for RVEs with grain sizes: a) 29 nm and b) 7 nm.

Fig. 1 shows the 2-D section maps of local von Mises equivalent strain for two (29 and 7 nm) of the four self-similar RVEs considered, relative to the applied macroscopic von Mises equivalent strain, for the case of nanocrystalline Cu deformed in quasiestatic axisymmetric compression along the z-axis. The main observation is that the strain is concentrated at GBs, reaching 10 times the macroscopic strain, while significant portions of the grain interiors undergo local strains which are less than the applied macrostrain. Another interesting observation is that the grains that deform the most are not necessarily the softest but the ones best located to link favorable oriented GBs (e.g. grain "A").

Fig. 2a shows the relative activities (strain partition) in the grain interiors and the GB phase, along with the corresponding volume fractions, as a function of grain size.

Consistent with the results of Fig. 1, the relative activity at GB exceeds the corresponding GB volume fraction. This trend is more marked as the grain size decreases. At 5 nm, the grain interiors contribute only with 10% to the overall strain, while they still represent almost half of the volume.

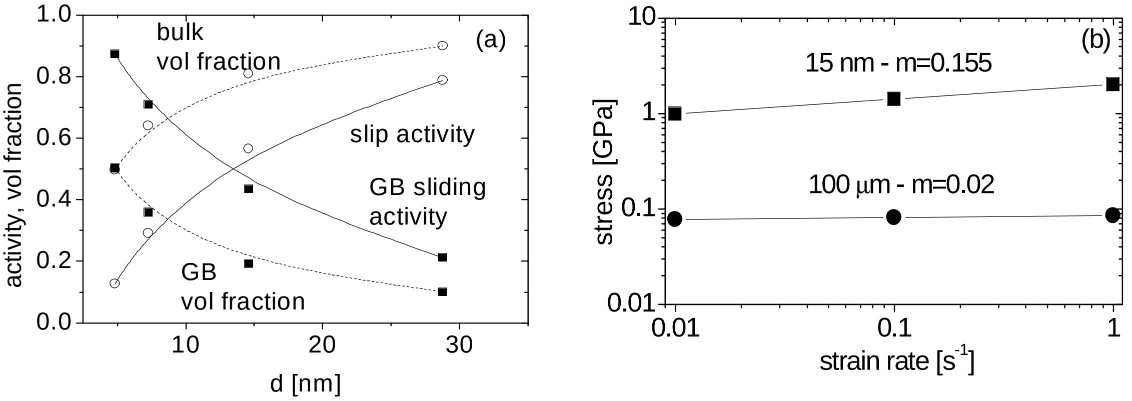

Figure 2: a) Strain and volume fraction partition as a function of grain size. b) Predicted log-log plot of yield strength vs. strain rate for the 15 nm grain and the CG material.

Fig. 2b shows the yield strength variations in the strain rate range 10^{-2}-10^{0} s^{-1}, for axisymmetric compression, as predicted for the 15 nm RVE. For comparison, we have included the strain-rate dependence of the coarse-grained material (100 µm). The resulting effective strain-rate sensitivity of the 15 nm material is m=0.155 (representing roughly an eight-fold increase with respect to the CG value of 0.02). This increase is comparable with the seven-fold increase with respect to the coarse-grained rate-sensitivity value reported by Lu et al [7] for the case of Cu containing nano-sized twins of ~20 nm width, deformed at room temperature and also with the ten-fold increase reported by May et al. [6] in ECAP-deformed Al with grain size of ~300 nm deformed at 250 °C.

References

1- Van Swygenhoven H, Spaczer M, Caro A, Farkas D. "Competing plastic deformation mechanisms in nanophase metals". Phys Rev B **60**, 22 (1999).

2- Jiang B, Weng GJ. "A generalized self-consistent polycrystal model for the yield strength of nanocrystalline materials". J Mech Phys Solids **52**, 1125 (2004)

3- Lebensohn RA, "N-site modelling of a 3D viscoplastic polycrystal using Fast Fourier Transform". Acta mater **49**, 2723 (2001).

4- Lebensohn RA, Bringa EM, Caro A. "A viscoplastic micromechanical model for the yield strength of nanocrystalline materials". Acta mater, submitted

5- Bringa EM, Caro A, Wang YM et al. " Ultrahigh strength in nanocrystalline materials under shock loading". Science **309**, 1938 (2005).

6- May J, Höppel HW, Göken M. "Strain rate sensitivity of ultrafine-grained aluminium processedby severe plastic deformation". Scripta Mater **53**, 189 (2005).

7- Lu L, Li SX, Lu K. " An abnormal strain rate effect on tensile behavior in nanocrystalline copper". Scripta Mater **45**, 1163 (2001).

Kinetics and thermodynamics of pressure-induced phase transitions in semiconductor nanoparticles

Nicola Marzari

Massachusetts Institute of Technology, 13-5066 DMSE, 77 Massachusetts Ave, 02139 Cambridge, United States of America

A novel electronic-enthalpy functional is introduced to study finite systems under pressure from first-principles. The external field P acts directly on the electronic structure of the quantum fragment via the minimization of the functional E + PV_q, where E is the total energy and V_q the ``quantum volume'' enclosed by a charge-density isosurface. The load is properly transferred to the ions thanks to the Hellmann-Feynman theorem, and the whole system follows constant-pressure relaxations or dynamics.

Using this framework, we were able to study the thermodynamics and kinetics of solid-solid phase transformations for carbon, silicon, and germanium nanoparticles undergoing hydrostatic shock compression. Significant differences are found in the plastic response of the nanoparticles and in the nucleation pathways, all strongly dependent on size, materials' choice, and the presence of ligands. The plastic transformation of silicon and germanium nanoparticles into metastable amorphous phases highlights the importance of kinetics over thermodynamics, and hints at the possibility of designing impact-absorbing composite materials based on collapsible nanoparticle components.

Last, the definition of the quantum volume leads to the equally natural definition of the quantum surface for a nanostructure, allowing thus to study tension effects in such diverse systems as confined electron bubbles, solvated species, and liquid droplets.

Non Planar Core and Dynamic Emission of Dislocation Loops in fcc Crystals

Dan Mordehai[1,3], **Guy Makov**[2] **and Itzhak Kelson**[1]

[1]School of Physics and Astronomy, The Raymond and Beverly Sackler Faculty of Exact Sciences, Tel Aviv University, Tel Aviv 69978, Israel
[2]Department of Physics, NRCN, PO. Box 9001, Beer Sheva, Israel
[3]Service de Recherches de Métallurgie Physique, CEA/Saclay, 91191 Gif-sur-Yvette, France

ABSTRACT

Plastic deformation at high strain rates occurs in systems such as shocked metals. The mechanisms that control the deformation remain unknown due to the difficulty of performing experimental metallurgical observations during the deformation. One of the key questions is what is the generation mechanism of shock-induced dislocation? Using molecular dynamics calculations we have studied screw dislocations in Cu (fcc) single crystals at high strain rates. In our calculations we have observed that under a stress of about 1 GPa the cores of the partial dislocations are no longer planar on the slip plane, but spread on to the cross-slip plane. Moreover, if the stress is increased further, partial dislocations are emitted dynamically on to the cross-slip plane, creating a stacking fault between them. The dislocation emission results in stacking faults along the secondary plane, which shear the crystal in this direction. These two phenomena, the non-planar core and the dynamic emission of dislocations, are discussed in the anisotropic elasticity theory framework.

1. Introduction

It is well known that dislocations play a significant role in plasticity of metals, and in particular at high strain rate deformations, such as shock waves etc. While, at relatively low stresses, the dynamic properties of dislocations are well established, both experimentally and theoretically, at high stresses the dynamic properties of high velocity dislocations are not well known. Experimental study of high velocity dislocations in metals, under high strain deformations, is performed *ex post facto*, and only little is known about the mobility and the structure of high velocity dislocations *while gliding*. In addition, at high strain rates, such as in shock-waves, these dislocation sources fail to explain the rapid increase in the mobile dislocation density, and the nature of dislocations generation mechanism is unknown.

The behavior of high velocity dislocations was addressed theoretically at the atomistic level. Gumbsch et. al. used molecular dynamics (MD) in order to study the mobility of an edge dislocation in W single crystal at high velocities ([1]). By introducing the dislocation with an initial velocity into the computational cell they were able to achieve sub- trans- and supersonic velocities. In the subsonic regime they did not observe dislocations with velocity above 70% the shear wave velocity C_t. About the same saturation velocity for subsonic edge dislocations was obtained by Rodney et. al. in Ref. [2] for Ni. Several transonic dislocations in Ref. [1] made a transition from transonic to subsonic during the calculation. They reported that the width of the transonic dislocation decreases as it became subsonic. Since all the reported subsonic dislocations were approximately gliding at the same velocity, there was no indication of the dependence of the dislocation width on the velocity in the subsonic regime. In [3] Marian et. al. studied screw dislocation motion in bcc iron at high strain rates using MD. They observed that at the intermediate velocity range the dislocation motion changes from kink-pair motion to a rough motion, with debris left behind. At even higher velocities,

the dislocation stops abruptly and emits twin plates. These simulations provided another insight of the microstructure formation in shocked materials.
In this work we study the role of screw dislocations at high strain rate deformations in fcc Cu, using MD calculations. Three different stress regimes, that characterize the dislocation motion, are identified. At low gliding stresses, with respect to the ideal shear strength, we obtained the classical picture of screw dislocation glide in fcc. Surprisingly, at higher stresses, in which the gliding velocity was about half the shear wave velocity, the dislocation drag force increases in an order of magnitude, and the dislocation core structure becomes non planar. At even higher stresses, but still less than the ideal shear strength, the dislocation glides at a velocity close to the shear wave velocity, and nucleates dislocation loops on to the cross-slip plane. We believe that this nucleation mechanism is dominant in plastic deformation at these stresses.

2. The Calculation Method

The atomistic method we use is a constant stress and temperature Molecular Dynamics (NσT-MD), based on the Parrinello and Rahman stress control method and the Nose-Hoover thermostat. The atomic interaction is described using a tight-binding second-moment approximation effective potential (TB-SMA). In [4] we found that this potential yields comparable comparison with experiments for the elastic constants dependence on temperature and pressure and for the stacking fault energy. A screw dislocation dipole structure was introduced by imposing initial displacements of the atoms, determined from the isotropic elastic strain around a screw dislocation. Each screw dislocation was introduced as a dissociated dislocation with a stacking fault ribbon and the system was equilibrated. The number of neighboring atoms inside a radius of the 3rd nearest neighbor distance is used to calculate the partial dislocation positions.

3. The Mobility and the Dissociation Width of a Screw Dislocation

When shear stress, which initiate dislocation glide, is applied to the system, the dislocations accelerate up to a terminal velocity. This velocity is stress and temperature dependent, and two different velocity regimes were identified: below and above half the shear wave velocity C_t. Below half C_t, the drag force increased linearly with velocity with a temperature dependent drag coefficient. The values for the drag coefficient were calculated in Ref. [4] and were found to be between 10 μPa·sec to 35 μPa·sec at the temperature range of 10K-300K. At the range of velocities above half C_t we observed a significant increase in the drag coefficient, and it is an order of magnitude higher than in the first velocity regime, i.e. an order of hundreds of μPa·sec, with a weak dependency on the temperature.

The dissociation width in the MD calculations undergoes dynamic changes in time. In the first velocity regime the dissociation width fluctuates. At intermediate velocities, corresponding to the transition between the first and second velocity regimes, the amplitude of these fluctuations dissipates quickly. As we increase the velocity further, the oscillations cease, and instead the dissociation width becomes unstable and increases throughout the time period of our calculations. Moreover, the average width is velocity dependent, within the velocity regime in which the dissociation width is stable, as presented in Fig. 1. One can see from these results that in the first velocity regime the dissociation width decreases with velocity down to 25% of its static value at a velocity of about $0.55C_t$. Beyond this velocity, in the second velocity regime, the dissociation width increases significantly with velocity and becomes unstable at velocities above $0.67\ C_t$, which corresponds to a stress of about 1 GPa.
The dissociation width of the non-gliding dislocation may be evaluated using elasticity theory from the balance between the forces acting on each partial dislocation: the stacking fault

energy, the interaction between the *gliding* partial dislocations, the drag force and an external force. However, if one assumes that the drag coefficients of both the trailing and leading partial dislocations are identical, the elastic model yields the results presented in Fig. 1 as 'Model I'. These results deviate from the MD results in the second velocity regime (Ref. [5]). When it is assumed that the drag coefficients differ in the second velocity regime, the model, denoted as ‘Model II’, fits the MD results. In order to understand the different drag coefficients, we examine in greater detail the dislocation structure in the MD at the unstable regime.

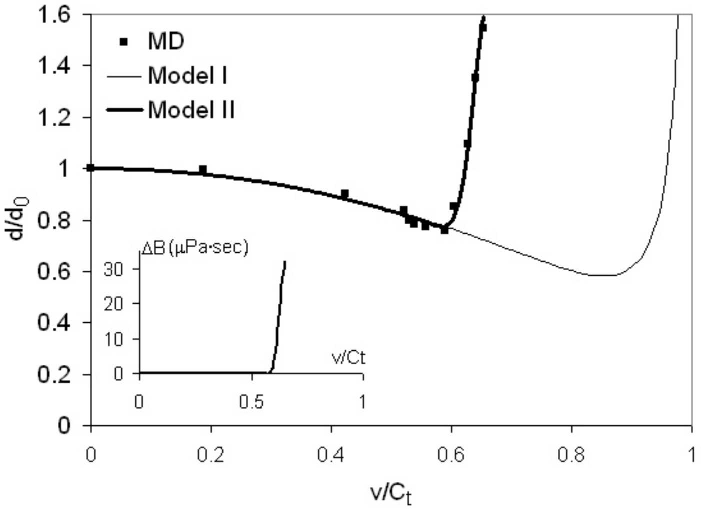

Figure 1. The dissociation width, normalized by the non-stressed dissociation width d_0, as a function of the velocity, normalized by the shear wave velocity - MD results and Elastic-Continuum models. The difference between the drag coefficients of partial dislocations in model II is shown in the in-set.

4. Non-Planar Structure of the Trailing Partial Dislocation

For an applied stress of 1.5 GPa, which results in a terminal velocity of $0.7C_t$, the trailing dislocation spreads onto the cross-slip plane and becomes non-planar (Fig. 2). The dislocation spreads onto the half plane that creates an acute angle with the stacking fault (SF). We did not observe similar behaviour for the leading partial. When we reversed the stress direction, the gliding direction was reversed also, and the partial dislocations switched roles. As in the previous case the trailing partial spreads onto the cross-slip plane, forming always an acute angle with the SF, leading us to the conclusion this is an intrinsic property of the dissociated dislocations. In addition, the structure is dependent on the internal stresses in the system, such as the interaction with the second dislocation at the dipole.

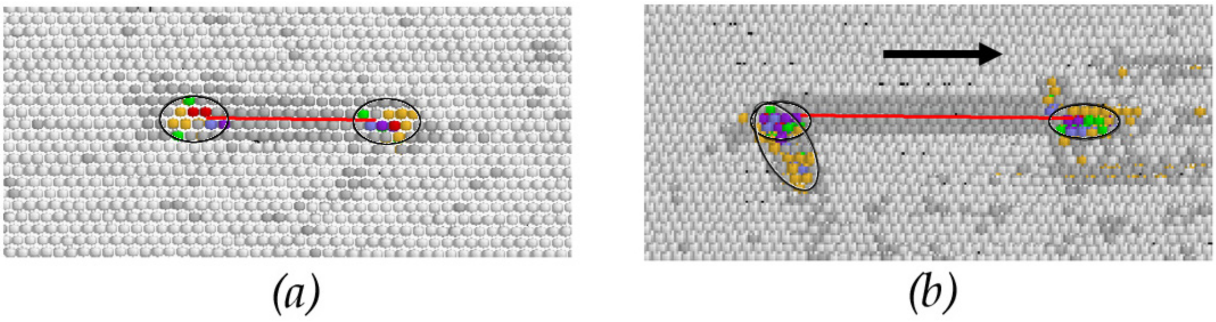

Figure 2. The core structure of (a) non-stressed dislocation (b) under a gliding stress of 1.5 GPa. The core structure of the partial dislocations is marked with ellipses. The red (dark gray) line and the arrows indicate the SF surface and the gliding direction, respectively.

5. Dynamic Emission of Dislocation Loops

When the stress is increased up to 4 GPa the dislocation accelerates up to a velocity very close to the shear wave velocity (about 97% the shear wave velocity). When the trailing partial dislocations of both dislocations in the dipole configuration approach their closest distance, the atoms in part of the bulk between the partial dislocations are misplaced from their fcc lattice positions, and immediately form stacking faults on the cross-slip of plane, bounded by two partial dislocations, i.e. dislocation loops. The area in which the nucleation occurs is correlated with the direction of the core spread onto the cross-slip plane, implying that these phenomena may be related.

After the nucleation the original dislocations remain unchanged. Under the influence of the applied stress, the original dislocations continue to glide on their slip planes, and the new generated dislocation loops grows, increasing the SF ribbon between them.

A closer examination of the atom displacement near the high velocity dislocations reveals a large displacement which is related to the anisotropic elastic field about a gliding dislocation. While in the stationary case the displacement field perpendicular to the glide plane about the dislocation is negligible, about a high-velocity dislocation it is of an order of the lattice constant. Moreover, this displacement is inhomogeneous, with maximal amplitude in an area close to the trailing partial dislocation, from the side that creates an acute angle with the SF.

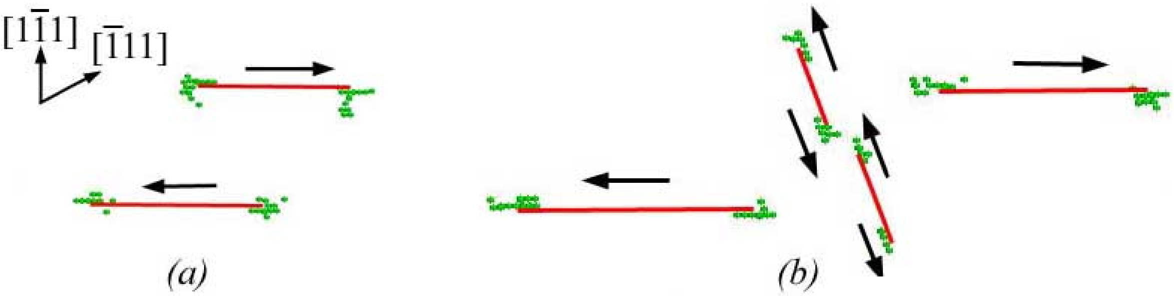

Figure 3. The nucleation process. Only the atoms in the partial dislocation cores are highlighted. SF is indicated with red line. (a) The dislocations glide before the nucleation (b) Two pairs of partial dislocations, separated by a SF, are created.

6. Summary

We suggest that both phenomena, the dynamic non-planar core structure and the dynamic emission of faulted loops, are intrinsic property of a high-velocity dissociated screw dislocation, which arises from the interaction force between the gliding partial dislocations. When the dislocation velocity is 70% the shear-wave velocity the amplitude of this non-usual displacement is larger than in the stationary case, but not large enough to nucleate a stacking fault. Instead it translates the atoms on the cross-slip plane near the trailing partial dislocation, and spreads the core onto both planes.

References

[1] P. Gumbsch and H. Gao, *Dislocations Faster than the Speed of Sound*, Science **283**, 965 (1999).

[2] D. Rodney and G. Martin, *Dislocation pinning by glissile interstitial loops in a nickel crystal: A molecular-dynamics study***,** Phys. Rev. B **61**, 8714 (2000).

[3] M. Jaime, W. Cai and V.V. Bulatov, *Dynamic transitions from smooth to rough to twinning in dislocation motion*, Nature Materials **3**, 158–163 (2004).

[4] D. Mordehai, Y. Ashkenazy, I. Kelson and G. Makov, *Dynamic properties of screw dislocations in Cu: A molecular dynamics study*, Phys. Rev. B **67**, 024112 (2003).

[5] D. Mordehai, G. Makov and I. Kelson, *Non Planar Core and Dynamical Behavior of Screw Dislocations in Copper at High Velocities*, Phys. Rev. B (accepted).

Atomistic simulations of dislocation–grain-boundary interactions in tungsten

Matous Mrovec[1,2], **Yuanfeng Cheng**[2], **Christian Elsässer**[1,2] **and Peter Gumbsch**[1,2]

[1]**Fraunhofer-Institut für Werkstoffmechanik, Wöhlerstrasse 11, 79108 Freiburg, Germany;**
email: matous.mrovec@iwm.fhg.de;
[2]**Institut für Zuverlässigkeit von Bauteilen und Systemen, Universität Karlsruhe (TH),**
Kaiserstrasse 12, 76131 Karlsruhe, Germany

ABSTRACT

Mechanical properties of polycrystalline materials are greatly influenced by the motion of dislocations and their interaction with grain boundaries. While isolated dislocations and grain boundaries can be treated nowadays with high accuracy by electronic-structure methods, simulations of mutual interactions between such extended defects are still beyond the reach of these methods because of too high computational demands. In order to describe processes of such complexity one has to cross the bridge between the electronic-structure calculations and atomistic simulations by coarse-graining the electronic degrees of freedom into many-body interatomic potentials. In our study we investigated several cases of dislocation-grain boundary interactions in the body-centered cubic (bcc) transition metal tungsten using a bond-order potential (BOP). The BOP is based on the tight-binding theory and therefore able to describe correctly directional covalent bonds which are crucial for the cohesion and structure of bcc transition metals. We will present results of BOP simulations for the interaction between both edge and screw dislocations and a variety of symmetric tilt grain boundaries, and discuss the relation between atomic-level phenomena and macroscopic crystal plasticity.

1. Introduction

When a polycrystalline metal undergoes plastic deformation, a large number of lattice dislocations impinge on grain boundaries (GBs) and interact with them. It has been observed experimentally that the interactions can result in impediment, transmission, absorption and reemission, or even reflection of dislocation [1-3]. Unfortunately, little information is available about details of these processes at the atomic scale.

In this work we investigate dislocation–grain-boundary interactions in bcc transition metal tungsten by atomistic simulations. Tungsten was chosen as our model material because of its peculiar mechanical behavior which is controlled to a great extent by the structure and properties of extended defects, namely dislocation cores and GBs. Depending on external conditions such as temperature, strain rate, or load orientation this transition metal can deform plastically by slip, by deformation twinning or it can fracture by predominantly intergranular cleavage. Behavior of dislocations, structures of GBs, and details of mutual interactions between these extended defects at the atomic scale are therefore of great interest since they may provide valuable information about conditions under which the competing deformation mechanisms will occur.

2. Simulation methods

The atomistic simulations were carried out using two distinct models of interatomic interactions - the empirical Finnis-Sinclair (FS) potential [4] and the bond-order potential (BOP) [5]. FS is a central-force scheme which has been used extensively in atomistic studies of extended defects in metals because of its simplicity and computational efficiency. Nevertheless, is is unable to describe properly the directional covalent bonds which are primarily responsible for the cohesion in bcc transition metals. In order to validate FS results we therefore repeated the simulations with the BOP model, which is based on the real-space parameterized tight-binding (TB) method and provides implicitly a correct description of angular character of bonding originating from d-electrons. An important advantage of the BOP scheme for simulations of extended defects and their interactions is that unlike classical TB models it scales linearly with the size of system since the diagonalization of the Hamiltonian matrix is replaced by direct calculation of the bond order in real space.

The computational procedure was the same in all simulations. In the first step, a GB was created in the center of a simulation cell, and its structure was fully relaxed to its ground state configuration. In this study two symmetric tilt GBs with a common $[\bar{1}10]$ tilt axis were chosen as model GBs since it is well known that large plastic deformation of bcc metals (e.g. during wire drawing) leads to a strong preferential <110> texture. The two investigated boundaries, namely $\Sigma3(11\bar{2})$ and $\Sigma3(111)$, are two representative cases of low and high energy GBs with energies of about 0.7 and 2.0 J/m^2, respectively.

After static relaxation of the GB structure a perfect screw dislocation with a 1/2[111] Burgers vector was introduced in the left grain apart from the $\Sigma3(11\bar{2})$ GB, while a perfect edge dislocation with the same Burgers vector was placed in the left grain of the $\Sigma3(111)$ GB. The dislocation line directions in both simulation blocks thus lie parallel to the GB plane. This setup, shown schematically in Fig. 1, allows for application of periodic boundary conditions along the dislocation line which reduces the size of the simulated system. Fixed boundary conditions were applied to the outermost layers in the other two directions.

With the dislocations present the blocks were again fully relaxed. During the relaxation the positions of the dislocation cores remained at their initial elastic centers. It should be noted that tungsten is almost elastically isotropic and that incompatibily stresses at GBs are therefore negligible. Consequently, there are no long-range elastic forces on a dislocation near a GB.

In the final step, a homogeneous shear strain was imposed on the simulation blocks, corresponding to a shear stress as prescribed by anisotropic elasticity theory. The shear stress was applied in the direction of the Burgers vector in such a way that the dislocations were forced to move towards the GBs. The shear strain was gradually increased in small increments and the block was fully relaxed after each step so that the simulations were done effectively at 0 K.

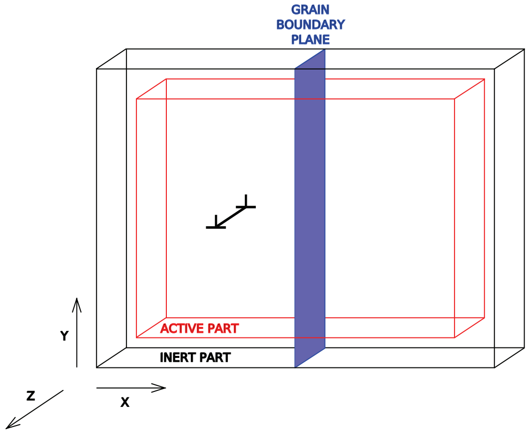

Figure 1. A schematic picture of the simulation block.

3. Results and Discussion

The configurations investigated in this work present rather special cases of dislocation-GB interactions. The dislocation line in both simulations was parallel to the GB plane, and the maximum resolved shear stress (MRSS) plane on which the dislocation was forced to glide was always the $(\bar{1}10)$ plane perpendicular to the GB plane. This glide plane continues undisturbed through the GB into the other grain. Both simulations therefore represent cases where both the Burgers vectors and the slip planes are common to both grains. It has been generally expected [6] that in this case the GB should not act as an obstacle to slip propagation because no residual GB dislocation are necessary to compensate for a change of the slip system.

In the BOP simulation of the interaction between the ½[111] screw dislocation and the $\Sigma3(11\bar{2})$ GB the dislocation started to move towards the boundary plane at an applied shear stress of 1.8% of the C_{44} shear modulus. This stress is the same as the critical resolved shear stress (CRSS) on a {110} plane for the screw dislocation in the bulk crystal, and the simulation confirms that the GB does not influence the CRSS.

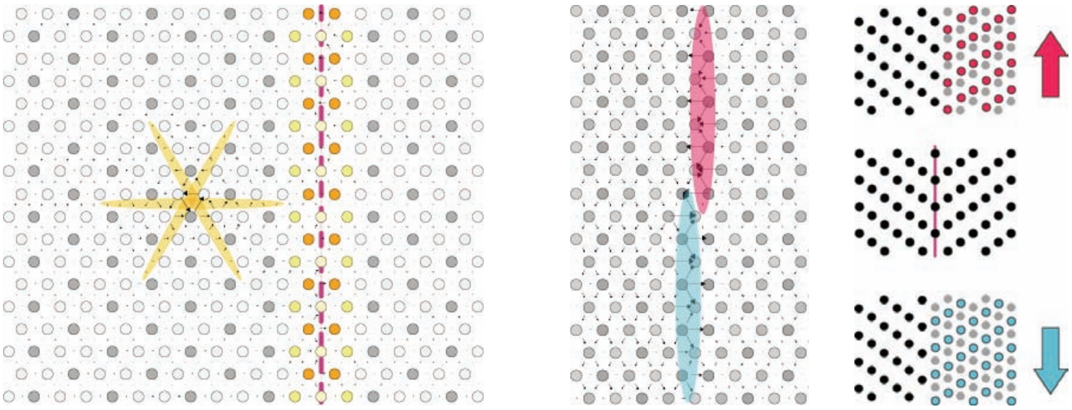

(a) (b)

Figure 2. Interaction between the ½[111] screw dislocation and the the $\Sigma3(11\bar{2})$ GB. (a) the initial configuration in a [111] projection; (b) the final configuration of BOP simulation in a [111] (left) and $[\bar{1}10]$ (right) projection, showing a step at the GB created by emission of two twinning dislocations in opposite directions.

When the screw dislocation reaches the GB it is absorbed and immediately dissociates into three partial dislocations with the Burgers vector of 1/6[111]. These dislocations are also known as twinning dislocations which propagate the deformation twin [7]. After the dissociation, two of the twinning dislocations glide in opposite directions on two neighboring $(11\bar{2})$ planes as shown in Fig. 2. As a result the GB above the glide plane shifts to the right while below the glide plane it shifts to the left, and a step is formed at the location of interaction. A third dislocation with the 1/6[111] Burgers vector is sessile and remains at the interface step. Both FS and BOP results are consistent and give similar results even though the core structure of the screw dislocation and the GB energy are not reproduced correctly by FS.

In the case of the interaction between the ½[111] edge dislocation and the $\Sigma3(111)$ GB the simulations with FS and BOP potentials give qualitatively different results (see Fig. 3). In the BOP simulation the dislocation is again blocked by the GB and stays embedded in the boundary even when the shear stress is increased up to 6% of C_{44}. The same GB in the FS calculations presents a much weaker obstacle for the dislocation. As is seen in Fig. 3(c), the incoming edge dislocation triggers the nucleation of a series of partial dislocations which follow the movement of the leading slip dislocation and effectively destroy the GB. The nucleated partial dislocations are again dislocations with the 1/6[111] Burgers vector which change the stacking of the (111) planes and restore thus the bulk structure of the left grain. This result is an obvious artifact of the FS potential, resulting from a propensity of the potential to twinning and an underestimation of the $\Sigma3(11\overline{2})$ GB energy.

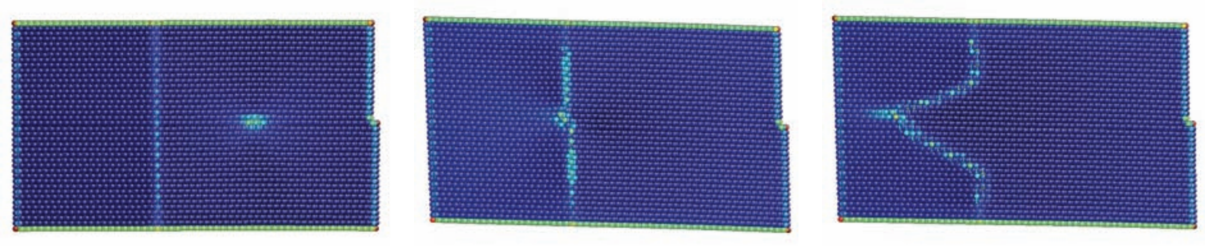

(a) (b) (c)

Figure 3. The $[11\overline{2}]$ projection of the interaction between the ½[111] edge dislocation and the $\Sigma3(111)$ GB. (a) the initial configuration; (b) and (c) the final configurations of BOP and FS simulations, respectively.

In summary, our simulations show that the investigated twin GBs are effective barriers to the motion of slip dislocations. The twoGBs can thus provide sites for dislocation pileups as well as for fracture nucleation. Local interaction with the boundary can effectively pin the dislocation but it is the GB structure and energetics which determines the outcome of the dislocation-GB interaction even for the simplest configurations with a common slip system in both grains. Our results indicate that a simple geometric criterion suggested in Ref. [1] is therefore not generally valid, and further calculations are necessary to verify its applicability.

Acknowledgements

Financial support from the European Commission through the Marie-Curie research and training network SizeDepEn (MRTN-CT-2003-504634) and from the German Science Foundation (DFG, Gu 367/25) is gratefully acknowledged.

References

[1] Z. Shen, R. Wagoner, W. Clark, *Dislocation and grain boundary interactions in metals*, Acta Met. **36** (1988) 3231.
[2] M. Polcarova, J. Gemperlova, J. Bradler, A. Jacques, A. George, L. Priester, *In-situ observation of plastic deformation of Fe-Si bicrystals by white-beam synchroton radiation topology*, Phil. Mag. A **78** (1998) 105.
[3] A. Gemperle, J. Gemperlova, N. Zarubova, *Interaction of slip dislocations with grain boundaries in body-centered cubic crystals*, Mat. Sci. Eng. A **387-389** (2004) 46.
[4] G. J. Ackland, R. Thetford, *An improved N-body semi-empirical model for bcc transition metals*, Phil. Mag. A **56** (1987) 15.
[5] D. G. Pettifor, *New many-body potentials for the bond order*, Phys. Rev. Lett. 63 (1989) 2480; M. Mrovec, D. Nguyen-Manh, V. Vitek, D. G. Pettifor, *Bond-order potential for molybdenum: Application to dislocation behaviour*, Phys. Rev. B **69** (2004) 094115.
[6] J. P. Hirth and J. Lothe, Theory of Dislocations, Wiley-Interscience, New York (1982).
[7] J. W. Christian, *Deformation twinning*, Prog. Mater. Sci. **39** (1995) 1.

A CONSTITUTIVE MODEL FOR GLASSY POLYMERS WITH SHEAR TRANSFORMATION ZONES PLASTICITY AND REPTATION-BASED VISCOELASTICITY

Svetoslav Nikolov [1], *Dierk Raabe* [1], *Franz Roters* [1]

[1] *Max-Planck-Institut für Eisenforchung, Max-Planck-Strasse 1, 40237 Düsseldorf, Germany*

We propose a micromechanical model for glassy polymers with newly developed constitutive relations for the viscoelastic and the viscoplastic flow rates. Viscoplasticity is modelled via a modified version of the Shear Transformation Zones (STZ) theory for amorphous glasses. The dynamics of plastic transformations is given by Eiring-type thermally activated rates. The evolution of the viscoplastic flow is described by two internal state variables, namely, the density of the shear transformation zones and a dimensionless back stress due to change in entropy from stress-induced net orientation of ellipsoidal STZ. For the viscoelastic flow rate, we consider the reptation of free chain ends where the other end of the reptating strands is fixed by an entanglement or by a crosslink. The resulting flow rule is different from similar developments previously proposed in the literature. The model predictions are compared to uniaxial compression experiments for different glassy polymers. The influence of the density of STZ on aging, annealing and mechanical rejuvenation effects is discussed.

Energetics of bending carbon nanotube

Shigenobu Ogata

Osaka Univeristy, 2-1 Yamada-oka, Suita-shi, 565-0871 Osaka, Japan

Energetics of bending single walled carbon nanotube is analyzed using minimum energy path calculation with a bond order potential. The calculation shows that plastic deformation by defect nucleation and motion is thermodynamically favorable above a threshold "yield curvature" and kinetically feasible above 1500K, which agrees with recent experimental observations by Nakayama. The yield curvature, which depends on nanotube diameter D, guarantees that carbon nanotube always deforms elastically below this curvature without any plastic deformation. We numerically estimated the yield curvature as a function of D, and find that the diameter dependency can be explained by a simple theoretical analysis of energy balance based on dislocation theory between defective (plastic) and non-defective (elastic) bending states, which predicts the yield curvature roughly proportional to 1/D. Finally we construct a deformation mechanism map of single walled carbon nanotubes as function of temperature and bending curvature.

Hybrid Density-Functional-Theory/Molecular-Dynamics/Fast-Coarse-Grained-Particle Simulation Schemes for Reaction Processes at Nano-interfaces

Shuji Ogata,[1,2] **Takahiro Igarashi,**[3] **Takahisa Kouno,**[1,2] **Ryo Kobayashi**[1,2]
and Hiroki Iida[1]

[1]**Graduate School of Engineering, Nagoya Institute of Technology, ogata@nitech.ac.jp;**
[2]**CREST, Japan Science and Technology Agency;**
[3]**Nuclear Science and Energy Directorate, Japan Atomic Energy Agency**

ABSTRACT

Motivated by increasing demand to perform atomistic simulation of nano-interfaces in realistic sizes, we have been developing the hybrid simulation schemes by concurrently combining the electronic-density-functional-theory (DFT), the molecular dynamics (MD), and the fast coarse-grained particle (FCGP) methods. In the hybrid DFT-MD scheme, multiple DFT regions each of which is composed of a relatively small number of atoms, are embedded in a system of classical MD atoms. The FCGP region forms the overall structure of the total system and gives the boundary condition to the MD region in the hybrid MD-FCGP scheme. The FCGP method, in which each particle represents a group of the atoms, is well suited to its connection with the MD method. For robust coupling of the DFT and MD regions with a reasonable mechanical accuracy, the buffered cluster method is proposed, which requires no link-atoms and is applicable to a wide range of materials and settings. During the hybrid DFT-MD simulation run, sizes and number of the DFT regions change adaptively to trace the chemical reactions. The hybrid simulation schemes are successfully applied to various interesting processes including chemisorption of water molecules on stressed Si-surfaces and oxygen transfer in a Si substrate.

1. Methodology

One of the principal characteristics of nano-systems is the mutual coupling of length-scales that span many orders. An efficient computer simulation approach to treat such an inherently multiscaled system, is to hybridize concurrently different simulation methods for different scales [1]. In the hybrid approach, a simulation system is partitioned in real space to regions, and various calculation methods such as the electronic structure calculation, the classical atomistic method, and the coarse-graining method, are applied appropriately to the regions. The atomistic simulation is crucial to analyze and advance the performance of the nano-systems. Considering these, we have been developing two different hybridization schemes based on the molecular dynamics (MD) method. In one scheme, we improve the physical accuracy of the MD method by combining it with the density-functional theory (DFT). In the other scheme, we combine the MD method with the fast coarse-grained particle method (FCGP) that we have developed recently to coarse-grain an atomistic region, for efficient treatment of large-scale systems.

1.1 Coupling MD with DFT

The link-atom method has been widely used to combine the MD and DFT regions in a hybrid system [2-4]. However, we find that the link-atom method is fairly sensitive to selection of the DFT region. We therefore propose a novel hybridization scheme, called the buffered cluster method [5]. In the method, the following Hamiltonian determine the dynamics of all atoms:

$$H = H_{\mathrm{MD}}^{\mathrm{system}}(\vec{R}_{\mathrm{all}}, d\vec{R}_{\mathrm{all}}/dt) + \sum_{\mathrm{cluster}}(E_{\mathrm{DFT}}^{\mathrm{cluster}} - E_{\mathrm{MD}}^{\mathrm{cluster}}). \qquad (1)$$

Here $\vec{R}_{\mathrm{all}}$ represents the set of all atoms. All the atoms in the total system are grouped into MD and DFT atoms. The positions of the MD and DFT atoms are denoted as $\{\vec{r}_{\mathrm{MD}}\}$ and $\{\vec{r}_{\mathrm{DFT}}\}$, respectively. The $H_{\mathrm{MD}}^{\mathrm{system}}$ in Eq. 1 is the MD Hamiltonian of the total system. The last two terms on the right hand side of Eq. 1 represent the quantum correction by the DFT to the MD potential energy of the DFT region. The atomic-cluster terms in the right hand side of Eq. 1 are functions of $\{\vec{r}_{\mathrm{DFT}}\}$ only:

$$E_{\mathrm{DFT}}^{\mathrm{cluster}} = E_{\mathrm{DFT}}^{\mathrm{cluster}}(\{\vec{r}_{\mathrm{DFT}}\}) \text{ and } E_{\mathrm{MD}}^{\mathrm{cluster}} = E_{\mathrm{MD}}^{\mathrm{cluster}}(\{\vec{r}_{\mathrm{DFT}}\}). \qquad (2)$$

Additional atoms are placed on the surfaces of the DFT cluster in both DFT and MD calculations to buffer possible boundary effects. The positions of those buffer atoms in the MD calculation are determined dynamically to minimize the potential energy of the cluster. The positions of the buffer atoms in the DFT calculation are determined using that of the buffer atoms obtained in the MD cluster calculations. The accuracy of the buffered cluster method is investigated though various kinds of analyses for hybrid Si crystals including the uniformity of bond lengths and the recoil forces between the DFT and MD atoms, the sensitivity of the minimum-energy structure on the Fermi level shift, and the uniformity of degrees of Si-Si bonding in the DFT region through Mulliken's overlap populations. We then find that the buffered cluster method can be safely used for any selection of the DFT region, and that it is applicable not only to a covalent system of Si but also to an ionic system of alumina.

1.2 Coupling MD with FCGP

A coarse-graining method has been proposed [6] for a crystalline system of atoms at finite temperatures, to describe the propagation of long-wavelength waves at low computation costs. In the method virtual particles that distribute in the system are introduced. Each particle relates to a group of constituting atoms, and the inter-particle interaction is obtained through the partition function of the atomic Hamiltonian in the harmonic approximation with constraint relating to such relations. Though the method has attractive features such as its natural incorporation of atomic phonons and its potential suitableness to connection to an atomistic simulation method, the original formulation limits its application to simple periodic systems without surfaces and deformations. We therefore modify the method applicable to realistic systems in various shapes under various stress conditions at lower computation costs, to propose the fast coarse-grained particle (FCGP) method. The physical meaning of the interaction energy in the FCGP method is clarified by comparison with the corresponding energies in full-atom calculations. The FCGP method is applied to realistic systems in various shapes with substantial deformations. The FCGP method predicts the distribution of internal stress and the propagation behavior of density variation, in good agreement with that observed in the original system of atoms.

The FCGP method is hybridized concurrently with the MD method for the atomistic description, in which the FCGP method gives the dynamic boundary conditions to the MD region. Assuming the lowest degree of coarse-graining (that is, no coarse-graining) to the MD region, the total Hamiltonian for the hybrid system is written in a modular form as

$$\begin{aligned} H_{\mathrm{hybrid}} &= H_{\mathrm{FCGP}}(\{\mathbf{r}_{\mathrm{all}},\mathbf{p}_{\mathrm{all}}\}) \\ &+ \sum_{\mathrm{cluster}} \left[H_{\mathrm{MD}}^{\mathrm{cluster}}(\{\mathbf{r}_{\mathrm{MD}},\mathbf{p}_{\mathrm{MD}}\},\{\mathbf{r_b},\mathbf{p_b}\}) - H_{\mathrm{FCGP}}^{\mathrm{cluster}}(\{\mathbf{r}_{\mathrm{MD}},\mathbf{p}_{\mathrm{MD}}\},\{\mathbf{r_b},\mathbf{p_b}\}) \right], \end{aligned} \tag{3}$$

where $H_{\mathrm{MD}}^{\mathrm{cluster}}$ and $H_{\mathrm{FCGP}}^{\mathrm{cluster}}$ are the MD and FCGP Hamiltomians, respectively, for the MD region $\{\mathbf{r}_{\mathrm{MD}},\mathbf{p}_{\mathrm{MD}}\}$ with the buffer atoms $\{\mathbf{r_b},\mathbf{p_b}\}$. The degree of mechanical coupling of the FCGP and MD regions is assessed through the internal deformation analyses and the wave propagation simulation, to find reasonable accuracies.

2. Applications

In continuing development of the hybrid DFT-MD simulation scheme, we have applied it to various kinds of significant engineering processes [5,7,8] including (i) dissociation reactions of water molecules on stressed Si, (ii) crack propagation of α-alumina, and (iii) atomic scale friction of saturated Si-tips incorporating a water droplet. The hybrid MD-FCGP simulation scheme is applied to structural analyses of α-Fe material. As an example, we mention in the following about the hybrid DFT-MD simulation of implantation of oxygen atoms to a Si substrate.

2.1 Implantation of oxygen to silicon: adaptive, dynamic selection of DFT region in hybrid DFT-MD scheme

We apply the hybrid DFT-MD simulation scheme to migration processes of implanted oxygen atoms in crystalline Si, which will be exploited to create an ultra-thin SIMOX (Separation by Implanted Oxygen) structure in future. SIMOX has recently been utilized to fabricate a micro-structure consisting of a thin layer of Si separated from the bulk Si substrate by a thin layer of SiO_2. Further advancement of SIMOX technology to fabricate nano-meter scaled silicon-on-insulator structures in future, requires understanding the effects of the initial velocity and the incident position of the implanted O atoms on their migration and oxidation processes.

We firstly prepare Si(100) Si-Si dimer surface with the dangling bonds fully saturated by H atoms. In the run, an O atom is placed initially above the middle of the two nearest-neighbor Si-Si dimers by 0.3nm. The O atom has the initial velocity of 0.05nm/fs normal to the surface; the kinetic energy of the O atom corresponds to 240eV, which is much smaller than the usual experimental values of $10^{2\text{-}3}$keV. Controlling the migration of the O atom at such a small kinetic energy will be necessary to fabricate an ultra-thin oxide layer. The thinner the insulator layer the larger the transistor density in ULSI. Figure 1 depicts time evolution of the atomic positions and the DFT region (depicted with the light atoms). We find the O atom moves normal (<100> direction), to the surface initially, and then hits a Si atom at about 10fs. After that, the O atom moves toward <111> direction. As seen in Fig. 1, the QM region expands adaptively during the simulation run to include neighboring Si atoms of the O atom; the algorithm to expand the DFT region is applied every 10 steps.

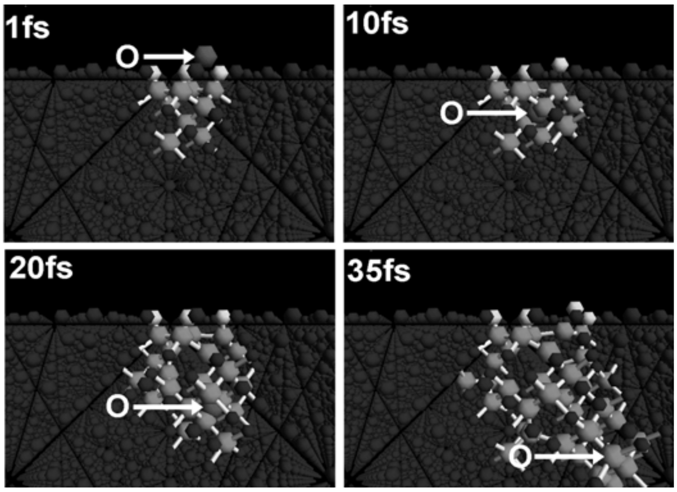

Fig. 1: Snapshots in the hybrid DFT-MD simulation of implanted O in Si.

3. Concluding Remarks

Present concurrent hybridization schemes are well suited to running in Grid computation environments. In fact, the simulation of implantation of oxygen in Sec. 2 had been performed successfully on a Japan-US large-scale Grid composed of about 700CPU's.

Various studies are in progress to advance the capability of the hybrid simulation schemes, which include concurrent hybridization of the FCGP and the lattice-Boltzmann methods for simulation of a supercritical fluid in an elastic wall.

References

[1] G. Lu and E. Kaxiras, Overview of multiscale simulation of materials, in *Handbook of theoretical and computational nanotechnology*, Vol. X, edited by R. Rieth dn W. Schommers (Am. Sci. Pub., N.Y. 2005), chap. 22.

[2] M. Eichinger and P. Tavan, A hybrid method for solutes in complex solvents: density functional theory combined with empirical force fields, J. Chem. Phys. 110, 10452 (1999).

[3] S. Ogata, E. Lidorikis, F. Shimojo, A. Nakano, P. Vashishta, and R.K. Kalia, Hybrid finite-element/molecular-dynamics/electronic-density-functional approach to materials simulations on parallel computers, Comp. Phys. Comm. 138, 143 (2001).

[4] S. Ogata, F. Shimojo, R.K. Kalia, A. Nakano, and P. Vashishta, Hybrid quantum mechanical/molecular dynamics simulations for parallel computers: density functional theory on real-space multigrids, Comp. Phys. Comm. 149, 30 (2002).

[5] S. Ogata, Buffered-cluster method for hybridization of density-functional theory and classical molecular dynamics: Application to stress-dependent reaction of H_2O on nanostructured Si, Phys. Rev. B 72, 45348 (2005).

[6] R.E. Rudd and J.Q. Broughton, Coarse-grained molecular dynamics and the atomic limit of finite elements, Phys. Rev. B 58, R5893 (1998).

[7] S. Ogata, F. Shimojo, and A. Nakano, P. Vashishta, and R.K. Kalia, Environment effects of H_2O on fracture initiation in Si: a hybrid electronic-density-functional/molecular-dynamics study, J. Appl. Phys. 95, 5316 (2004).

[8] S. Ogata and R. Belkada, A Hybrid electronic-density-functional/molecular-dynamics simulation scheme for multiscale simulation of materials on parallel computers: application to silicon and alumina, Comp. Mat. Sci. 30, 189 (2004).

Intensive octahedral slip as the origin of cleavage in iridium single crystals

Peter Panfilov[1], *Mikhail Yu. Gutkin*[2]

[1] *Urals State University, Institute of Physics and Applied Mathemetics, Lenin ave., 51, 620083 Ekaterinburg, Russia*
[2] *Institute of Problems of Mechanical Engineering, Russian Academy of Sciences, Bolshoj 61, Vasil. Ostrov, 199178 St. Petersburg, Russia*

The words “plasticity“ and “brittleness“ traditionally sound as antonyms. However, sometimes a solid may exhibit both the high plasticity and a tendency to brittle fracture. Single crystalline iridium is a rare example that absolutely meets this surrealistic combination of deformation phenomena, when its giant plasticity prior the cleavage fracture is carried through the octahedral slip of <110> dislocations on the easy slip stage. It seems that this circumstance could open new prospects for a description of plastic deformation in FCC-metallic materials within the theory of dislocations. The experimental basis is discussed which may be used for development of theoretical models and computer simulations aimed at understanding the fundamental physical mechanisms responsible for the ductile-brittle transition in refractory FCC metals.

Research is partially supported by the Russian Foundation for Basic Research (grant # 04-03-32073).

An atomistic-continuum multiscale approach towards technological realization of carbon nanotube actuators

Lars Pastewka

Fraunhofer Institute for Mechanics of Materials IWM, Wöhlerstr. 11, 79108 Freiburg, Germany

Since their discovery in 1992, carbon nanotubes have been proposed for a wealth of applications. Among these is the use of nanotubes as actuators as discovered in 1999 by Baughman et al [1]. Baughman immersed nanotubes into a liquid electrolyte and discovered expansion of the tubes upon charging. In order to realize a device using this effect a solid electrolyte will be most likely mandatory. Knowledge about the efficiency of nanotube-electrolyte coupling with respect to actuation is however very limited.

Here, we present a multiscale approach for modelling force transfer from the tubes to the embedding matrix. This is achieved by incorporating the effect of bond length stretching of individual tubes into the empirical Tersoff potential [2]. The parameters of the potential are gauged using density functional based tight-binding calculations [3] within the self-consistent charge level of theory [4]. Furthermore, these tubes are embedded into a matrix which is described by a smoothed particle (SPH) discretization [5] of the continuum equations of elasticity. This gives an effective medium without the need to model the microscopic details explicitly. For the tube-matrix coupling, a van-der-Waals interaction is used, which is possible because of the particle nature of the smoothed particle discretization. This does naturally lead to a single Hamiltonian multiscale approach which incorporates the stiffness of the tube and the matrix, as well as the force transfer from tube to matrix correctly.

Using this model stress-strain relations are extracted using sample nanotube-electrolyte setups.

References

[1] R. H. Baughman et al., Science 284, 1340 (1999)

[2] J. Tersoff, Phys. Rev. B 37, 6991 (1988); J. Tersoff, Phys. Rev. Lett. 61, 2879 (1988)

[3] D. Porezag et al., Phys. Rev. B 51, 12947 (1995)

[4] M. Elstner et al., Phys. Rev. B 58, 7260 (1998)

[5] J. J. Monaghan, Annu. Rev. Astron. Astrophys. 30, 543 (1992); J. J. Monaghan, Rep. Prog. Phys. 68, 1703 (2005)

Nanomechanics: New experiments in atom resolved AFM and nanoimprint lithography

John Pethica

CRANN, Trinity College, D2, Dublin, Ireland

This talk will describe two new experimental areas of nano-mechanics, in both of which modelling plays a key role. We have developed a small (<0.05nm) amplitude method of sensing force gradients for AFM, using a specialised laser interferometer. Recent improvements in signal to noise now enable routine recording of force gradient and tunnel current simultaneously, at atomic resolution within a single image. Results for Si(111), TiO_2(110) and Cu(100) surfaces will be shown. Simultaneous imaging allows differences between force contours and tunnel current contours to be seen directly, without any uncertainty of lateral registry and tip position. This enables extraction of topographic contour effects, giving clear demonstration of the types and origins of forces involved. For oxides, the polarity of the tip can be determined directly from the registry (anion vs cation) between force and current, giving a potentially powerful new atomic resolution charge sensing method.

Imprint lithography, the formation of patterns by mechanical stamping, has nanometre resolution, high throughput and low cost. We have used nanoindentation methods to understand the limitations of normal loading, which are due to elastic strains. We show that a small amplitude shear oscillation provides a remarkable increase in mass transport, preserves full nm fidelity and has important scaling advantages. Finite element modelling clarifies the novel inelastic pumping mechanism involved, and the surprising relative insensitivity to interfacial friction conditions.

A simple model to understand the cleavage of diamond from the bond breaking

Pablo Pou[1,2], *Ruben Perez*[2], *Peter Gumbsch*[1,3]

[1]*IZBS, Universität Karlsruhe (TH), Kaiserstraße 12, 76131 Karlsruhe, Germany*
[2]*Departamento de Fısica Teórica de la Materia Condensada, UAM, 28049 Madrid, Spain*
[3]*Fraunhofer-Institut fuer Werkstoffmechanik IWM, Woehlerstr. 11, 79108 Freiburg, Germany*

First principles simulations provide the basis for the critical assessment of the different mechanisms proposed to explain the highly selective preference of diamond to fracture in the {111} set of planes. The Griffith criterion, $G \geq 2\gamma$, is a necessary condition for fracture and implies that crystal lattice planes with low surface energies are energetically favored as cleavages planes. However this criterium is not enough to explain the diamond case. We have shown that all the different mechanisms proposed so far to explain the highly selective fracture of diamond in the {111} set of planes (including surface energy considerations, surface reconstructions, growth defects and hydrogen contamination) can be discarded on the basis of first principles simulations. Crack tip stability calculations for different crack orientations in the (111) and (110) planes suggest that cleavage in diamond is controlled by energy barriers to bond breaking that lead to lattice trapping of the crack. Our calculations for crack tip stability show the absence of significant lattice trapping barriers, signalled by a continuous bond breaking process without pronounced structural relaxations, in all propagation directions in the (111) plane. In contrast, the large lattice trapping and the anisotropic behavior with respect to crack propagation in different directions in the (110) plane results on average in a higher fracture toughness. The different propensity to lattice trapping is well reproduced by differences in the cohesive force function to separate two rigid slabs along their surface normals. A simple model that focuses on the accurate determination of the bond force non-linearity is then proposed as an alternative to full fracture simulations to characterize the lattice trapping, and thus, the fracture behavior of materials.

3D dislocation dynamics simulations of micron-sized FCC Ni crystals

Satish Rao

UES Inc., 4401 Dayton-Xenia Road, 45432, Dayton, USA

A parallel 3-D dislocation dynamics code, PARADIS, developed at Lawrence Livermore National Laboratory, is used to predict the stress-strain behavior of micron sized crystals of FCC Ni at ambient temperature. The simulations are performed using both constant strain rate and pseudo – constant strain rate loading conditions, which allows the deforming crystal to exceed the prescribed rate under constant stress conditions. The strain levels achieved in the simulations ranges from 0.1 – 1%, and free surface boundary conditions are used. Significant features of the simulated stress-strain curves include: periodic strain bursts, load drops, and a significant hardening with decreasing sample size. These results are shown to be in fairly good agreement with previously published experimental results. Mobile dislocations and their interactions with forest dislocations are analyzed at different points along the stress-strain curves. It is shown that 'surface mediated source hardening' as well as 'junction debris' formation contributes significantly to hardening of the stress-strain curves at smaller sample sizes.

Instability Analyses of Nanogrid Structures with Quasicontinuum Beam Model

Hiro Tanaka[1], **Yoji Shibutani**[1,2]

[1]**Department of Mechanical Engineering,**
Osaka University, Osaka 565-0871, Japan,
E-mail:tanaka@comec.mech.eng.osaka-u.ac.jp
[2]**Center for Atomic and Molecular Technologies,**
Osaka University, Osaka 565-0871, Japan,
E-mail:sibutani@mech.eng.osaka-u.ac.jp

ABSTRACT

Inelastic responses of nanostructured materials such as organic nanogrids largely depend on their structural specificity and nonlocal effect based on the molecular bond. In the present paper, we propose the simple quasicontinuum modeling constructed by a beam element which can deals with the geometric and the material nonlinearities. Applying this to inelastic deformation problems of hexagonal and square grid structures by actuating a single member inside grids, the deformation manner is quite different each other. The size dependence of the whole model and the nonlocal effect to the instability of the grid structures are discussed.

1. Introduction

In recent years, various nanostructured materials such as organic nanogrids [1] have been developed by the state of the art material design that exploits the self-organizing technique. These are very interesting as the functional materials whose internal structures are built up from molecules. Thus, their mechanical behaviors of the nanogrid structures are highly dependent on nonlinear motion of microscopic internal structures. When analyzing the finite deformation of such nanomaterials for future design, an appropriate modeling which can represent the nonlinear molecular bond and the mutual interaction beyond the certain range is necessary. Typical geometric feature of the nanogrid materials is to consist of the beam members sustaining tension, bending and torsion. In the present paper, the beam element model with the quasicontinuum constitutive relation is proposed respecting the following three aspects;

(1) the strain observed in the member is still infinitesimal as undergoing finite displacement,
(2) the constitutive equation is nonlinear and determined by molecular configuration, and
(3) structural instability and post-buckling behaviors are crucial.

To demonstrate the deformation by the quasicontinuum beam model, we analyze two types of hexagonal and square grid structures under self-equilibrium internal actuation force. The actuation proceeds by extending the rest length of the actuated beam, which is here called single member actuation [2]. The single member actuation loading is related to the regional deformation by piezo actuators and is linked to the mechanism of the internal thermal expansion. We discuss the size dependence of the whole model and the nonlocal effect to the instability of the grid structures.

2. Quasicontinuum Beam Model

To describe the finite deformation of the nanogrids, a total-Lagrangian displacement based finite element beam model is formulated by using rotational pseudovector, Rodrigues parameter and Eulerian angles in the finite displacement field [3,4]. The Eulerian angles are used for easy geometrical description of the given model [4]. Also, we assume many-body force field of coarse-grained potential energy consisting of $\Phi_2(x_r)$, $\Phi_3(x_\theta)$ and $\Phi_4(x_\psi)$, where x_r, x_θ and x_ψ are distance, rotation angle and torsion angle to the interparticle arrangement, respectively. The constitutive relationship $\boldsymbol{K}(\boldsymbol{x})$ represented by internal variable $\boldsymbol{x}=\{x_r, x_\theta, x_\psi\}$ is, thus, derived from equivalence of each potential energy and each strain energy of linear elasticity [5] stored into the beam member which primarily deforms in bending or stretching manner. Therefore, stiffness equation is:

$$\boldsymbol{F} = \boldsymbol{T}_0(\boldsymbol{d})\boldsymbol{K}(\boldsymbol{x})\boldsymbol{T}_0^{\mathrm{T}}(\boldsymbol{d})\boldsymbol{r}(\boldsymbol{d}),$$

where $\boldsymbol{F}$ is the external force, $\boldsymbol{T}_0(\boldsymbol{d})$ the coordinate transform matrix and $\boldsymbol{r}(\boldsymbol{d})$ the node relative displacement as a function of displacement vector $\boldsymbol{d}$ using Eulerian angles. Hence, tangent stiffness matrix can be written as

$$\begin{aligned}\Delta\boldsymbol{F} &= \left\{\frac{\partial \boldsymbol{T}_0}{\partial \boldsymbol{d}}\boldsymbol{K}\boldsymbol{T}_0^{\mathrm{T}}\boldsymbol{r} + \boldsymbol{T}_0\boldsymbol{K}\frac{\partial \boldsymbol{T}_0^{\mathrm{T}}}{\partial \boldsymbol{d}}\boldsymbol{r} + \boldsymbol{T}_0\boldsymbol{K}\boldsymbol{T}_0^{\mathrm{T}}\frac{\partial \boldsymbol{r}}{\partial \boldsymbol{d}}\right\}\Delta\boldsymbol{d} + \boldsymbol{T}_0\frac{\partial \boldsymbol{K}}{\partial \boldsymbol{x}}\boldsymbol{T}_0^{\mathrm{T}}\boldsymbol{r}, \\ &= \left(\bar{\boldsymbol{K}}_{gn} + \bar{\boldsymbol{K}}_{mn}\right)\Delta\bar{\boldsymbol{d}},\end{aligned}$$

where $\Delta\bar{\boldsymbol{d}}$ is the incremental displacement vector represented by rotational angles about three axes of rectangular Cartesian coordinates. This equation shows the nonlinear information about gradient tensor $\bar{\boldsymbol{K}}_{gn}$ corresponding to geometrical nonlinearity and $\bar{\boldsymbol{K}}_{mn}$ corresponding to material nonlinearity determined by the potential function with internal variable $\boldsymbol{x}$. By resolving this tangent stiffness equation with the arc-length method, we can analyze finite deformation problem of grid structures under the prescribed boundary condition.

3. Results and Discussions

We analyzed two types of grid structures under actuation of the centered member whose one node is fixed to avoid the rigid motion, as shown in Fig.1. The hexagonal grid locally deforms in the bending dominated manner, while the square grid does not entirely behave in the bending-dominated and is not localized in one spot. Moreover, when increasing the applied actuation, a compressive buckling has occurred in the members aligned in the actuated direction. Fig.2 (a) shows dimensionless load-displacement curves with the conventional continuum model and the quasicontinuum model (QCM) under single member actuation for square grids with various sizes. The downward arrows in Fig.2 denote the buckling points. The vertical axis of $(f_{\mathrm{total}} - f_{\mathrm{SMA}})\,/\,EA$ indicates the resistance of the surrounding members to the actuated member of f_{SMA}. In the continuum model, it is confirmed that all of the post-buckling curves after the downward arrows coincide independent to the model size. The reason is that the post-buckling behavior is localized in a certain region, whose size is equivalent to the 9×8 Units model, as shown in Fig.2 (b). The other finding is that the grid structures with the nonlocal effect represented by QCM yield the earlier compressive buckling than the continuum solution. The nonlocal effect is strongly dependent to the local geometric change rather than the continuum solution respecting the global deformation. Thus, the descent of the member stiffness derives the earlier commencement of the buckling apart from the same response at the initial deformation stage.

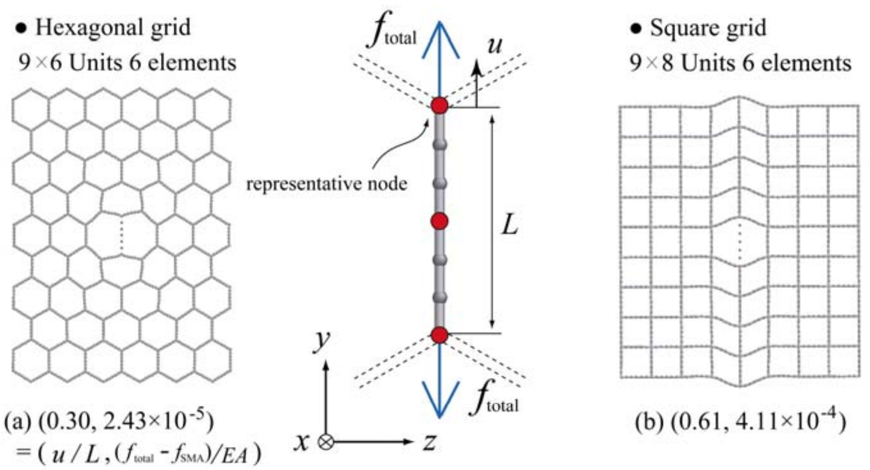

Fig.1 Single member actuation model and the shape of the hexagonal or square grids after a single rod (shown dashed) is actuated. The stiffness of an element is determined by the potential function of geometrical arrangement of representative nodes.

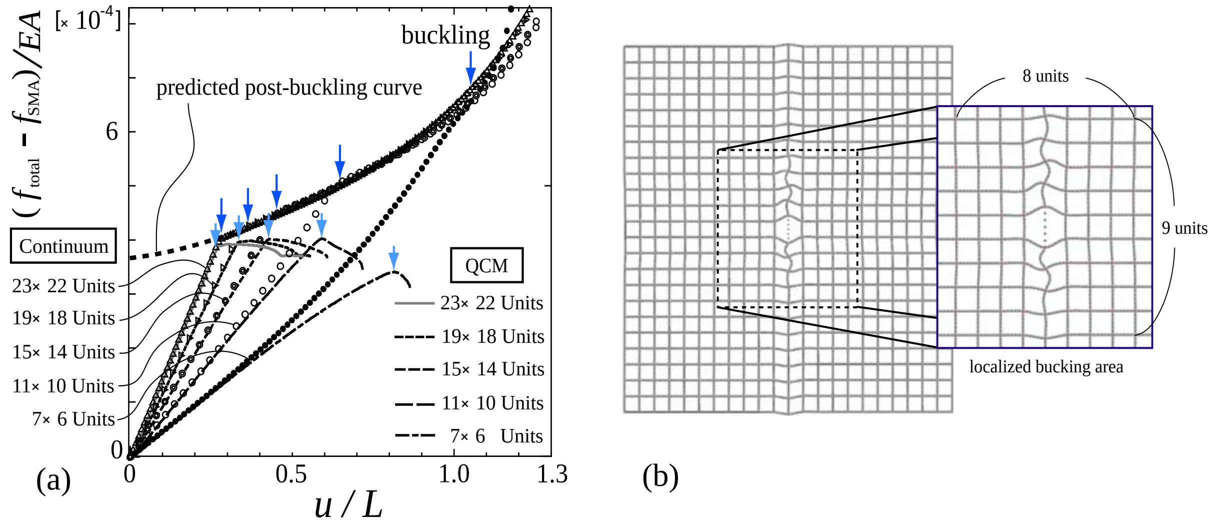

Fig.2 (a) Size dependence observed in load-displacement curves in the case of square grids. (b) the post-buckling shape of square grid structure (23×21 Units 6 Elements).

Acknowledgements

The author (H.T.) greatly acknowledges the support from educational program of design and integration.

References

[1] Desiraju, G.R., Supermolecular Synthons in Crystal Engineering-A New Organic Synthesis, Angewandte Chemie International Edition in English, Vol34, No.21 (1995), pp.2311-2327.

[2] Wicks, N., Guest, S.D., Single Member Actuation in Large Repetitive Truss Structures, International Journal of Solids and Structures, Vol.41, No.4 (2004), pp.965-978.

[3] Argyris, J., Excursion into large rotations, Computer Methods in Applied Mechanics and Engineering, Vol.32, (1982), pp.85-155.

[4] Gotou, H. Et al., A Simple Finite Displacement Formulation Using Eulerian Angles, Journal of Structural Engineering, A, Vol.43, (1997), pp.333-338.

[5] Li, C., Chou, T.W., A Structural Mechanics Approach for the Analysis of Carbon Nanotubes, International Journal of Solids and Structures, Vol.40, No.10 (2003), pp.2487-2499.

Finite elements computation of mechanical properties of copper thin film under tensile and cyclic loading

Filip Siska

Centre des Materiaux, Ecole des Mines de Paris, BP 87, 91003 Evry, France

The thin metallic films are very important parts of the modern electronics devices, and therefore it is necessary to study the properties of these films. The mechanical behaviour of the thin films is different from the behaviour of the bulk materials. Some of these differences are related to the film thickness and grain size. These effects are called size-effects. One possible way of studying of the properties are simulation with using of finite element method. In this work the film is represented by the polycrystalline aggregate. Material behaviour is described by the classical crystal plasticity. Parameters of the model are obtained from the tensile and cyclic tests of copper single crystal. The texture correspond to typical texture of the copper thin films which contains mainly {111} oriented grains and some part of {001} and randomly oriented grains. The computations were provide on the freestanding films and the films on the polyimide and silicon substrate. Tensile and cyclic loading was applied with prescribed amount of deformation. There were used two types of cyclic loading tension – compression, and cyclic tension. The results of computations from 5 realizations of the aggregate are collected and the development of plastic behaviour is compared, the evolution of the heterogeneities of the stress and strain in grains. The evolution of the surface roughness is also evaluated. The computations with using Cosserat crystal plasticity are made to check the possibility of the modelling of size–effects.

A new theory of electromigration

Adrian Sutton[1], *T.N. Todoroov*[2]

[1]*Imperial College London, Department of Physics, Exhibition Road, SW7 2AZ, London, United Kingdom*
[2]*School of Mathematics and Physics, Queen's University Belfast, BT7 1NN, Belfast, United Kingdom*

The current densities that can be achieved in metallic nanojunctions approach 1015 Am-2. At such high current densities forces on atoms cuased by the passage of the current can be so large they may lead to failure of the wire in much less than a second - a phenomenon we have called „current- induced embrittlement“ [1]. Current-induced forces also give rise to electromigration, the current-induced diffusional transport of matter, which is an important factor in the design of existing integrated circuits and may play an even greater role in molecular electronics. We have developed a thermodynamic analysis of electromigration [2,3] which reveals the macroscopic free energy that drives the process and relates it directly to the microscopic force and its quantum mechanical origin. At the heart of the analysis is the notion that current-induced forces are conservative, and we discuss an argument due to R Sorbello which suggests that current- induced forces are not conservative. We show that a Maxwell relation [3] in the thermodynamic analysis leads to a new physical picture of current- induced forces and we prove this relation independently for a self- consistent electronic structure model.

1. „Current-induced embrittlement of atomic wires“, T N Todorov, J Hoekstra and A P Sutton, Phys. Rev. Lett., 86, 3606-3609 (2001)

2. „Current-induced forces in atomic-scale conductors“, T N Todorov, J Hoekstra and A P Sutton, Phil. Mag. B, 80, 421-455 (2000)

3. „A Maxwell relation for current-induced forces“, A P Sutton and T N Todorov, Molecular Physics 102, 919-925 (2004)

Temperature Dependence of Peierls-Nabarro Barrier in Strained Crystal

A.V. Telezhnikov, **I.L. Maksimov**

Nizhny Novgorod University,Theoretical Physics Department, 23 Gagarin Ave., Nizhny Novgorod, 603950, Russian Federation; telezhnikov@phys.unn.ru, ilmaks@phys.unn.ru

ABSTRACT

We study the temperature effect on the dislocation mobility threshold inside the plastically deformed crystals within the Frenkel – Kontorova dislocation model. We obtained the temperature dependent the Peierls-Nabarro energy for both discrete and continuum limits.

1. Model

Many works are devoted to the study of a Peierls-Nabarro (PN) barrier energetics as a function of the mechanical strain of a material. However, the results obtained in previous works are valid mainly for the zero temperature case. At the present work we study the temperature influence on a dislocation mobility threshold within the Frenkel – Kontorova (FK) dislocation model. According to the FK model the dislocation energy in a field of the external force *F* playing a role of a shear stress, enters as

$$U = \sum_{n=-\infty}^{\infty} \left(U_0\{ x_n \} - F x_n \right),$$

where U_0 reflects the superposition of periodic and elastic components:

$$U_0(x_n) = A\left(1 - cos\frac{2x_n\pi}{a}\right) + \alpha\frac{(x_{n+1} - x_n - a)^2}{2};$$

here A is the modulation amplitude of a periodic potential, α is an elastic constant of the one-dimensional chain. We employ the technique developed by T.Matsubara [1] in order to analyse the thermal effects in solids. For this purpose we obtain the trial free Gibbs energy which is derived by means of averaging of the system hamiltonian on the basis of the ensemble of the statistically independent harmonic oscillators, the parameters of which are determined by means of variational procedure. The phonon hamiltonian with the help of which the averaging is performed, we choose as

$$H_0 = \sum_{n=-\infty}^{\infty} \left(a^2 \frac{k_n {w_n}^2}{2} + \frac{{p_n}^2}{2m} \right), \quad (1)$$

Hamiltonian of crystal with a dislocation with temperature fluctuations is

$$H = \sum_{n=-\infty}^{\infty} \left(\frac{{p_n}^2}{2m} + U_0(x_n, w_n) - aFx_n \right), \quad (2)$$

here $w_n = (x_n - x_{n0})/a$ represent the fluctuations caused by the influence of temperature.

Assuming the dislocation core to be located in a well with number *l*, we may carry out the averaging of (2) on the basis of the hamiltonian H_0 (1). As a result of standard, but cumbersome calculations (not included here), we obtain the trial Gibbs energy G^+ in a form

$$G^+ = \langle H - H_0\rangle_0 + F^0 \equiv \sum_{l=-\infty}^{\infty} G_l^+ = \sum_{l=-\infty}^{\infty}\left(A\left(1-\cos\left(\frac{2x_l\pi}{a}\right)\exp\left(-\frac{2\pi^2 T}{a^2 k_l}\right)\right)+\right.$$

$$\left.+\alpha\left(\left(\frac{x_{l-1}-2x_l+x_{l+1}}{2}\right)^2+\frac{T}{2k_l}\right)-Fx_l+\frac{T}{2}\ln k_l\right)$$

Minimization conditions for G^+ with respect to x_l and k_l, accordingly, are $\partial G^+/\partial x_l = 0$ and $\partial G^+/\partial k_l = 0$. The final equilibrium equations are

$$\begin{cases} Exp[-\tau/\lambda_n]Cos\xi_n + \gamma = \lambda_n, \\ Exp[-\tau/\lambda_n]Sin\xi_n + \dfrac{\gamma}{2}(2\xi_n - \xi_{n-1} - \xi_{n+1}) = f, \end{cases} \tag{3}$$

where we introduce the non-dimensional parameters

$$\xi_n = 2\pi x_n/a, \gamma = \alpha a^2/(2\pi^2 A), \tau = T/(2A), f = aF/(2\pi A), \lambda_n = k_n a^2/(4\pi^2 A).$$

The parameter γ is defined the ratio between the interatomic interaction energy along the FK chain and the atoms interaction energy with a substrate.

2. Results

We are interested in the analysis of two extremal cases. In the discrete limit (the parameter $\gamma \ll 1$) the equilibrium atom displacements in the FK chain may been easily calculated [3]. The solution of the system (3) (in a limit $\gamma \ll 1$) demonstrates two (numerical) functions $\xi_0^+(\tau)$ and $\xi_0^-(\tau)$, which describe two excitations with maximum and minimum energy. Thus, we find the energy of dislocation for a Frenkel-Kontorova model in a form:

$$U(\tau, f)/A \equiv \left(U\left(\xi_0^+\right) - U\left(\xi_0^-\right)\right)/A = cos\,\xi_0^- - \xi_0^+ + \frac{\gamma}{2}\left(\left(\xi_0^+\right)^2 - \left(\xi_0^-\right)^2 + \pi\gamma\left(\xi_0^- - \xi_0^+\right)\right).$$

The numerically calculated behaviour of the FK dislocation energy is shown in fig. 1. It is revealed that in the discrete limit the PN barrier height decreases with temperature according to the power-law $U(\tau) \approx U_0[1-\tau/\tau_c]^{3/2}$, where τ_c is the stress-dependent critical temperature ($U(\tau_c) = 0$).

In the continuum model ($\gamma \gg 1$), first analysed by [2], the equations set (3) may be appreciably simplified (in the case *f* = *0* [2]):

$$\begin{cases} Exp(-\tau/\gamma)Sin(2\pi\xi_k/a) = \gamma d^2\xi/dk^2, \\ \lambda_n = \gamma. \end{cases} \tag{4}$$

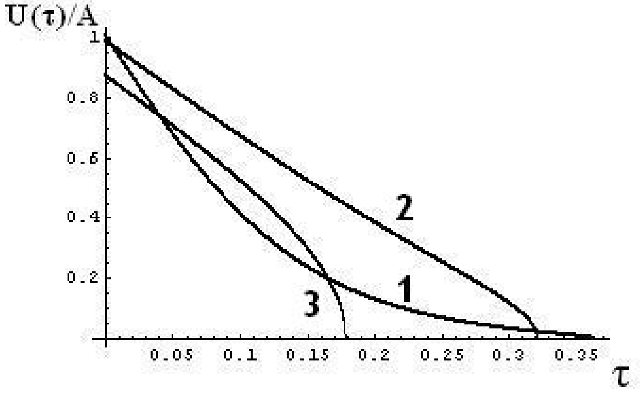

Fig.1. Dislocation energy within the FK model $U(\tau)/A$ ($\gamma = 0.01$);
1. f = 0.05, 2. f = 0.2, 3 f = 0.5.

With the help of the Eq. (4) one calculates the total energy of dislocation in a form

$$U = U_0(\tau) + 4A\sum_{m=1}^{\infty} Cos(2\pi m k_0)\int_{-\infty}^{\infty} \frac{1+(-1)^m e^{-\tau/\gamma}}{ch^2\left(\pi k' e^{-\tau/(2\gamma)}/l_0\right)} Cos(2\pi m k')dk',$$

$$U_0(\tau) = (4a/\pi)\sqrt{\gamma A}\, ch(\tau/2\gamma) \equiv U_0 ch(\tau/2\gamma).$$

Thus, the PN energy may be represented in term of series $U = U_0 + U_1 + U_2 + \dots$. For example, as a result of calculations we obtain the temperature dependence of the PN energy *U* within the former approximations [2, 3]. Namely, authors of [2, 3] include first two terms, U_0 and U_1, into the expression of *U*. Using such an approach we obtain the temperature dependence of *U(τ)*, and show that *U(τ)* is characterized by a double-exponential behaviour on the non-dimensional temperature τ:

$$U_1 = U_0 l_0 \pi Exp[-\pi l_0 Exp[\tau/2\gamma]]\left(2Exp[\tau/2\gamma]Sh(\tau/2\gamma) + 11\pi^2/18\right)$$

We should note that the value of other corrections has the same order as first ones. Indeed,

$$U_2 \approx -U_0 l_0 \pi^5 (137/1350) Exp\left(-\pi l_0 Exp[\tau/2\gamma]\right)$$

and (for the case τ = 0) we have $|U_2/U_1| \approx 1{,}6$. Thus, we may conclude that even for non-zero temperature, the contribution of other harmonics is quite essential. Therefore, one needs to calculate the total series $U = \sum_{n=0} U_n$ .in order to determine the total PN energy, the situation similar to that for a zero-temperature case.

References

1. I.L. Maksimov, K. Kitamura, K. Nishioka, Phil. Mag. Lett., v. 81, p.547 (2001).
2. V.L. Indenbom, Crystallography, v.3, p.195 (1958).

3. O.V.Usatenko, A.V.Gorbach. and A.S.Kovalev, Phys. Sol. State, v. 43, p.7 (2001).

A numerical method for homogenization in isotropic and anisotropic nonlinear elasticity

İlker Temizer, Peter Wriggers

Institute of Mechanics and Computational Mechanics
Leibniz University of Hannover, Appelstr. 9a, 30167 Hannover, Germany
E-mail: {temizer, wriggers}@ibnm.uni-hannover.de

ABSTRACT

In this contribution, homogenization of macroscopically anisotropic heterogeneous materials is addressed in the context of nonlinear elasticity. The concept of a material map, where one identifies the constitutive behavior of a material in a discrete sense through interpolation among various RVE states in the stress-strain space, is discussed together with its implementation in the finite element method. The homogenization of the nonlinearly elastic, macroscopically anisotropic heterogeneous material is then realized through the computation of its material map. An application of this approach to the analysis of a two-scale periodic particulate composite, where the matrix of the composite is also identified as a heterogeneous material, is presented.

1. Homogenization in the nonlinear deformation regime

Homogenization of microheterogeneous materials for the linear elastic analysis of macrostructures is well-established. In this regime, one identifies the macroscopic stress $\boldsymbol{\sigma}^*$ and strain $\boldsymbol{\epsilon}^*$ at a point of the macrostructure as the volume average of microscopic stress and strain fields over a statistically representative volume element (RVE) [1]. Explicitly, $\boldsymbol{\sigma}^* = \langle \boldsymbol{\sigma} \rangle_{\mathcal{V}_o}$ and $\boldsymbol{\epsilon}^* = \langle \boldsymbol{\epsilon} \rangle_{\mathcal{V}_o}$ where $\mathcal{V}_o$ denotes the undeformed configuration of the RVE, and $\boldsymbol{\sigma}$ and $\boldsymbol{\epsilon}$ denote stress and strain tensors in the linear regime, respectively. These macroscopic quantities are determined by subjecting the RVE to boundary conditions that satisfy Hill's energy criterion which reads $\langle \boldsymbol{\sigma} \cdot \boldsymbol{\epsilon} \rangle_{\mathcal{V}_o} = \langle \boldsymbol{\sigma} \rangle_{\mathcal{V}_o} \cdot \langle \boldsymbol{\epsilon} \rangle_{\mathcal{V}_o}$. The macroscopic elasticity tensor $\mathbb{E}^*$ then relates these two quantities via the linear elasticity constitutive equation $\boldsymbol{\sigma}^* = \mathbb{E}^* \boldsymbol{\epsilon}^*$. Therefore, it is sufficient to determine $\mathbb{E}^*$ once, and use it in subsequent linear elastic macrostructural analyses.

In the nonlinear elasticity regime, the macroscopic kinetic and kinematic quantities are identified as $\boldsymbol{P}^* = \langle \boldsymbol{P} \rangle_{\mathcal{V}_o}$ and $\boldsymbol{F}^* = \langle \boldsymbol{F} \rangle_{\mathcal{V}_o}$, where $\boldsymbol{P}$ and $\boldsymbol{F}$ denote microscopic 1^{st} Piola-Kirchhoff stress and deformation gradient tensors, respectively. These macroscopic quantities are determined by subjecting the RVE to boundary conditions that satisfy Hill's energy criterion in the nonlinear regime, which reads $\langle \boldsymbol{P} \cdot \dot{\boldsymbol{F}} \rangle_{\mathcal{V}_o} = \langle \boldsymbol{P} \rangle_{\mathcal{V}_o} \cdot \langle \dot{\boldsymbol{F}} \rangle_{\mathcal{V}_o}$. One then defines other kinetic and kinematic quantities using $\boldsymbol{P}^*$ and $\boldsymbol{F}^*$. In particular, $\boldsymbol{S}^* \overset{\text{def}}{=} (\boldsymbol{F}^*)^{-1} \boldsymbol{P}^*$ is the effective 2^{nd} Piola-Kirchhoff stress tensor and $\boldsymbol{E}^* \overset{\text{def}}{=} \frac{1}{2}\left((\boldsymbol{F}^*)^T \boldsymbol{F}^* - \boldsymbol{I}\right)$ is the effective Lagrangian strain tensor, where $\boldsymbol{I}$ is the identity tensor. Moreover, assuming that the constituents of the heterogeneous material are hyperelastic then so is the macroscopic material, and if one identifies $\mathcal{W}^* = \langle \mathcal{W} \rangle_{\mathcal{V}_o}$ where $\mathcal{W}$ is the microscopic strain energy, then $\boldsymbol{P}^* = \frac{\partial \mathcal{W}^*}{\partial \boldsymbol{F}^*}$ or, equivalently, $\boldsymbol{S}^* = \frac{\partial \mathcal{W}^*}{\partial \boldsymbol{E}^*}$.

---

[1] The notation $(.)^*$ denotes the macroscopic equivalent of a microscopic quantity. The volume average of a quantity $\mathcal{Q}$ with respect to a domain Ψ is defined as $\langle \mathcal{Q} \rangle_\Psi \overset{\text{def}}{=} \frac{1}{|\Psi|} \int_\Psi \mathcal{Q} \, \mathrm{d}\Psi$.

If the heterogeneous material displays macroscopic isotropy, the most general form of the constitutive equation of this material is $\boldsymbol{S}^* = \phi_0^* \boldsymbol{I} + \phi_1^* \boldsymbol{E}^* + \phi_2^* (\boldsymbol{E}^*)^2$ where ϕ_i^* are functions of the set of invariants of $\boldsymbol{E}^*$: $\phi_i^* = \widehat{\phi_i^*}(I_{\boldsymbol{E}^*}, I\!I_{\boldsymbol{E}^*}, I\!I\!I_{\boldsymbol{E}^*})$. However, explicit forms of the functions ϕ_i^* are not known *a priori* so material test data is required in order to characterize the macroscopic constitutive behavior. One method for this characterization involves proposing relatively general forms for ϕ_i^*, or alternatively for $\mathcal{W}^* = \widehat{\mathcal{W}^*}(I_{\boldsymbol{E}^*}, I\!I_{\boldsymbol{E}^*}, I\!I\!I_{\boldsymbol{E}^*})$, with free parameters which are determined by an optimization procedure that makes use of the test data [1]. An alternative method is the direct usage of material test data by referring to a database of RVE computation results during the macrostructural analysis, as attempted in [2, 3, 4]. This approach has been pursued in [5] for the homogenization of macroscopically isotropic heterogeneous materials, where a database (referred to as the *material map*) for the values of ϕ_i^* was created in the eigenvalue space $(\lambda^1_{\boldsymbol{E}^*}, \lambda^2_{\boldsymbol{E}^*}, \lambda^3_{\boldsymbol{E}^*})$ of $\boldsymbol{E}^*$. The use of this map during a macrostructural analysis essentially corresponds to interpolation among known RVE stress-strain states in order to generate a continuous stress-strain relationship that characterizes the macroscopic behavior of the heterogeneous material. In this contribution, this approach is extended to the analysis of macroscopically anisotropic heterogeneous materials in the context of nonlinear elasticity.

2. Homogenization in anisotropic nonlinear elasticity

Consider a periodic composite which displays macroscopic orthotropy. In the absence of microstructural bifurcations, the RVE $(\mathcal{V}_o)$ is identified as the unit cell of the periodic composite, and the macroscopic stress may be computed by imposing periodic boundary conditions which control $\langle \boldsymbol{F} \rangle_{\mathcal{V}_o}$. For clarity, the homogenization methodology is presented in a two-dimensional setting.

2.1 Generation of a material map and its implementation

Let the unit vector $\boldsymbol{n}$ denote the material orientation characterizing orthotropy. The macroscopic constitutive behavior of this composite is described by $\mathcal{W}^* = \widehat{\mathcal{W}^*}(\boldsymbol{E}^*, \boldsymbol{n} \cdot \boldsymbol{E}^* \boldsymbol{n})$ [6]. Although the tensorial dependence of $\boldsymbol{S}^*$ on $\boldsymbol{E}^*$ and $\boldsymbol{n}$ may be derived from $\mathcal{W}^*$ using $\boldsymbol{S}^* = \frac{\partial \mathcal{W}^*}{\partial \boldsymbol{E}^*}$, the number of unknown functions (similar to ϕ_i^*) that appear in the resulting form for $\boldsymbol{S}^*$ may not match the number of equations available through the components of $\boldsymbol{S}^*$, contrary to the macroscopic isotropy case [5]. This indeterminacy may be avoided by creating a material map for the components of $\boldsymbol{S}^*$.

The material test space $(\lambda^1_{\boldsymbol{E}^*}, \lambda^2_{\boldsymbol{E}^*}, \theta)$ is used for the generation of the map, where θ denotes the orientation of the eigenvector basis $\{\boldsymbol{v}_1, \boldsymbol{v}_2\}$ of $\boldsymbol{E}^*$ with respect to $\boldsymbol{n}$. The test space is meshed in a manner similar to the generation of a finite element mesh. The components $[\boldsymbol{S}^*]^v_{11}$, $[\boldsymbol{S}^*]^v_{22}$ and $[\boldsymbol{S}^*]^v_{12}$ of $\boldsymbol{S}^*$ are determined at the map mesh nodes, and the continuity of the map is ensured via interpolation using map element shape functions. Explicitly, $[\boldsymbol{S}^*]^v_{AB} = \sum_I [\boldsymbol{S}^*]^{v,I}_{AB}\, \Phi_I$ where $[\boldsymbol{S}^*]^{v,I}_{AB}$ is the nodal value of the stress component, and $\Phi_I = \widehat{\Phi}_I(\lambda^1_{\boldsymbol{E}^*}, \lambda^2_{\boldsymbol{E}^*}, \theta)$ is a map element shape function. Here, the notation $[\cdot]^v_{AB}$ denotes the components of a tensor with respect to the eigenvector basis of $\boldsymbol{E}^*$.

The macrostructural calculations require the macroscopic tangent stiffness $I\!\!L^* \overset{\text{def}}{=} \frac{\partial \boldsymbol{S}^*}{\partial \boldsymbol{E}^*}$ at each integration point of the macroscopic finite element mesh. For this purpose, the tangent induced by the material map is employed:

$$\mathbb{L}^* = \frac{\partial \boldsymbol{S}^*}{\partial \boldsymbol{E}^*} = \frac{\partial \boldsymbol{S}^*}{\partial \lambda^1_{\boldsymbol{E}^*}}\frac{\partial \lambda^1_{\boldsymbol{E}^*}}{\partial \boldsymbol{E}^*} + \frac{\partial \boldsymbol{S}^*}{\partial \lambda^2_{\boldsymbol{E}^*}}\frac{\partial \lambda^2_{\boldsymbol{E}^*}}{\partial \boldsymbol{E}^*} + \frac{\partial \boldsymbol{S}^*}{\partial \theta}\frac{\partial \theta}{\partial \boldsymbol{E}^*}\,. \tag{1}$$

Here, $\boldsymbol{S}^* = [\boldsymbol{S}^*]^v_{AB}\boldsymbol{v}_A \otimes \boldsymbol{v}_B$. The non-zero components of the terms $\frac{\partial \lambda^1_{\boldsymbol{E}^*}}{\partial \boldsymbol{E}^*}$, $\frac{\partial \lambda^2_{\boldsymbol{E}^*}}{\partial \boldsymbol{E}^*}$ and $\frac{\partial \theta}{\partial \boldsymbol{E}^*}$ are

$$\left[\frac{\partial \lambda^1_{\boldsymbol{E}^*}}{\partial \boldsymbol{E}^*}\right]^v_{11} = 1 \quad , \quad \left[\frac{\partial \lambda^2_{\boldsymbol{E}^*}}{\partial \boldsymbol{E}^*}\right]^v_{22} = 1 \quad , \quad \left[\frac{\partial \theta}{\partial \boldsymbol{E}^*}\right]^v_{12} = \frac{1}{2(\lambda^2_{\boldsymbol{E}^*} - \lambda^1_{\boldsymbol{E}^*})}\,. \tag{2}$$

The indeterminacy when $\lambda^1_{\boldsymbol{E}^*} = \lambda^2_{\boldsymbol{E}^*}$ is avoided by a small perturbation of the eigenvalues. It is noted that the components of $\mathbb{L}^*$ induced by the map does not necessarily display major symmetry, i.e. $[\mathbb{L}^*]^v_{ABCD} \neq [\mathbb{L}^*]^v_{CDAB}$, even when the constituents are hyperelastic, therefore macroscopic hyperelasticity is lost and the stiffness matrices generated in the finite element method are unsymmetric. However, the error in major symmetry $([\mathbb{L}^*]^v_{ABCD} - [\mathbb{L}^*]^v_{CDAB})$ diminishes with increasing map resolution.

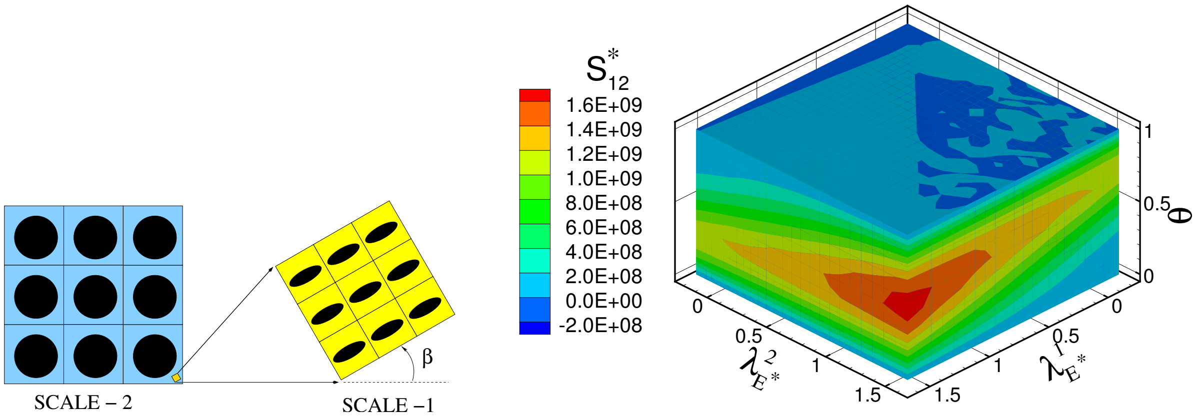

Figure 1: LEFT: A two-dimensional depiction of a two-scale periodic microstructure. RIGHT: The material map for S^*_{12} *of the Scale-1 composite which is generated by stretch increments of* 0.05 *and orientation increments of* 10°. *The orientation angle* $\theta \in [0, \pi/2]$ *is normalized to the interval* [0, 1].

Table 1: Test parameters used in calculations.

κ^0 (GPa)	μ^0 (GPa)	κ^1 (GPa)	μ^1 (GPa)	κ^2 (GPa)	μ^2 (GPa)	v_1 (%)	v_2 (%)
10	6	40	24	60	36	25	40

2.2 A numerical example

Consider a two-scale periodic particulate composite material, where the matrix of the composite (Scale-2) is also identified as a periodic particulate composite (Scale-1), as depicted in Fig 1. For experimental purposes, the strain energy functions of the constituents are chosen as a modified Kirchhoff-St.Venant type for which $\mathcal{W} = \frac{\kappa_1}{2}(\ln(J))^2 + \frac{\kappa_2}{2}(\operatorname{tr}(\boldsymbol{E}))^2 + \mu\boldsymbol{E}' \cdot \boldsymbol{E}'$. Here, $J = \det(\boldsymbol{F})$ and $\kappa_1 + \kappa_2 = \kappa$, where κ and μ are the bulk and shear moduli, respectively, and $(\cdot)'$ denotes the deviatoric part. In particular, $\kappa_1 = \kappa_2 = \frac{\kappa}{2}$ is employed. The simulation parameters used are given in Tab 1, where 0 denotes matrix of Scale-1, 1 denotes the particles of Scale-1, 2 denotes the particles of Scale-2 and v_i denotes the volume fraction of the particles for the corresponding scale. The particles of Scale-1 are elliptical with an aspect ratio of 2, and those of Scale-2 are circular [2].

---

[2] Macroscopic stress is insensitive to the position of the particle in the unit cell when periodic boundary conditions are used.

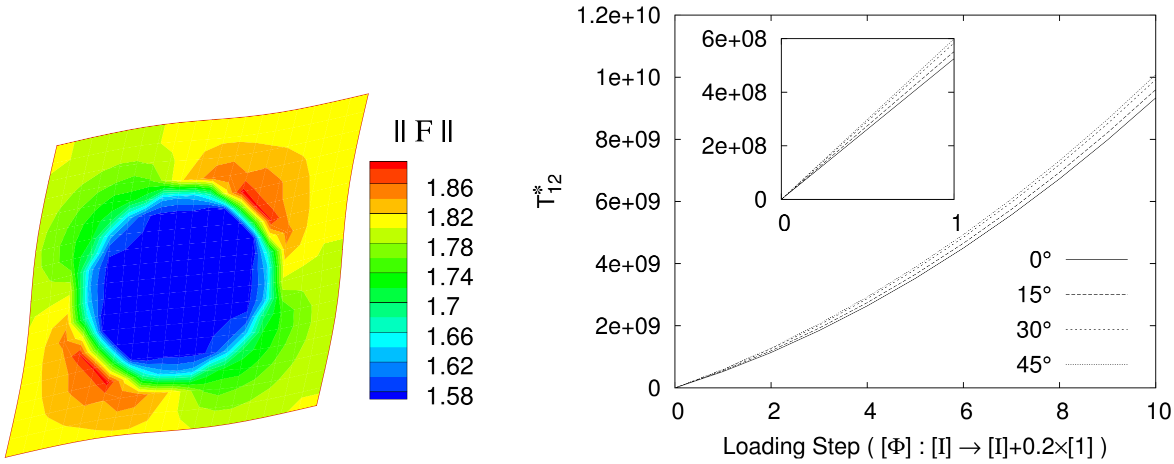

Figure 2: LEFT: $\|\boldsymbol{F}\|$ *distribution in the Scale-2 composite for* $\boldsymbol{\Phi} \overset{\text{def}}{=} \langle \boldsymbol{F} \rangle_{\mathcal{V}_o} = \boldsymbol{I} + 0.2 \times \mathbf{1}$*, where* $\mathbf{1}$ *is the tensor with all components equal to one with respect to the basis employed. RIGHT: The variation of the macroscopic Cauchy stress* $\boldsymbol{T}^* \overset{\text{def}}{=} \frac{1}{det(\boldsymbol{F}^*)} \boldsymbol{F}^* \boldsymbol{S}^* (\boldsymbol{F}^*)^T$ *component* T^*_{12} *in the Scale-2 composite with deformation and with the variation of the orientation angle* β *(see Fig 1) of the Scale-1 composite.*

The material map characterizing the macroscopic S^*_{12} stress component of the Scale-1 composite is shown in Fig 1. Note that this component would trivially vanish when the composite displays macroscopic isotropy. The computed material map is subsequently used in the analysis of the Scale-2 composite in order to observe its macroscopic behavior. The dependence of the S^*_{12} component of the macroscopic stress at Scale-2 is plotted for increasing deformation in Fig 2, where the dependence of this stress on the orientation (β) of the Scale-1 composite (see Fig 1) is also shown.

References

[1] M. Itskov, A. E. Ehret, and D. Mavrilas. A polyconvex anisotropic strain-energy function for soft collagenous tissues. *Biomechanics and Modeling in Mechanobiology*, 5(1):17–26, 2005.

[2] K. Terada and N. Kikuchi. Nonlinear homogenization method for practical applications. In S. Ghosh and M. Ostoja-Starzewski, editors, *Computational Methods in Micromechanics*, AMD-Vol.212/MD-Vol.62, pages 1–16. Proceedings of the ASME International Mechanical Engineering Congress and Exposition., 1995.

[3] N. Takano, M. Zako, and Y. Ohnishi. Macro-micro uncoupled homogenization procedure for microscopic nonlinear behavior analysis of composites. *Materials Science Research International*, 2(2):81–86, 1996.

[4] S. Ghosh, K. Lee, and P. Raghavan. A multi-level computational model for multi-scale damage analysis in composite and porous materials. *International journal of solids and structures*, 38:2335–2385, 2001.

[5] İ. Temizer and T. I. Zohdi. A numerical method for homogenization in non-linear elasticity. *Computational Mechanics (accepted)*, 2006.

[6] I.-S. Liu. *Continuum Mechanics*. Springer, Berlin Heidelberg New York, 2002.

Life of a dislocation in a nanocrystalline fcc metal

Helena Van Swygenhoven & **Peter M. Derlet**

Paul Scherrer Insitute, ASQ/NUM – Materials Science & Simulation, PSI-Villigen, CH-5232, Switzerland

ABSTRACT

Detailed analysis of the nucleation and propagation of dislocations from grain boundaries in nanocrystalline Al using molecular dynamics reveals that: (1) the leading and trailing partial dislocations are nucleated at different regions within a grain boundary or even different grain boundaries; (2) propagation is hindered by a pinning–depinning mechanism influenced by the relative orientation between the Burgers vector and the ledge geometry of the grain boundary and (3) depinning is thermally activated and therefore not purely mechanically driven.

1. Introduction

It is generally accepted that grain boundaries (GBs) act as both sources and sinks for dislocations when the grain size is reduced to the nanometre regime in face-centred cubic (fcc) metals. This mechanism has been suggested by molecular dynamics (MD) computer simulations [1–4], where a partial dislocation is emitted from a GB, travels through the entire grain, and is eventually absorbed in neighbouring and opposite GBs. MD has revealed that for some materials (such as Al) trailing partials can follow after the emission of the leading partial, whereas for other materials (such as Ni and Cu) a trailing partial is not observed and a stacking fault (SF) defect transecting the entire grain is formed. It has been recently demonstrated that to understand the MD results one has to consider both the stable and unstable SF energies through the generalised SF energy curve [5,6].

In the present work we study the nucleation, propagation and absorption of a full dislocation in nc-Al, paying attention to the role of the surrounding grain boundary structure and how temperature can affect the atomic scale processes at hand. In what follows we detail the lifetime of one representative full dislocation from nucleation and propagation to its eventual absorption [7]. Though we restrict this report to one dislocation, the observations presented and the associated conclusions may be considered quite general since the reported behaviour has been seen in all other studies of dislocation events.

2. Technical details of the simulation

An nc-Al sample was simulated that contains 15 randomly orientated grains with a mean grain size of 12 nm. This sample has a similar GB network structure and misorientation distribution to that used in a number of previous simulations. The sample was built using a Voronoi procedure in which individual grains are geometrically constructed followed by a molecular statics and room temperature MD relaxation procedure, which is outlined in greater detail in Ref. [8]. The Al EAM empirical potential of Mishin et al. [9] was used, which has a ratio of stable to unstable SF energy close to unity, indicating that given the nucleation of a leading partial dislocation there is a strong probability that the trailing partial follows within the timescale of the MD simulation. Thus the use of this potential allows for the study of the nucleation and propagation of full dislocations. A tensile load of 1.6 GPa was used resulting in several leading and trailing dislocations in different grains during 50 ps of deformation, one of which we describe in detail in the following section.

4. Nucleation

Fig. 1 shows the details of the nucleation process, starting from the configuration after elastic loading (set to 0 ps). The viewing direction is parallel to the normal of the (111) slip plane of grain. The first evidence of the leading partial is observed 0.25 ps after elastic loading where a local protrusion of non-fcc atoms occurs in GB 1–2 (circled region). Although at this early stage, no red hcp coordinated atoms evidencing a SF are observed, this protrusion can be identified as the nucleation of the dislocation core of the leading partial. Upon further deformation, the leading partial starts travelling away from the GB. The existence of the trailing partial in the GB is first visible at 5.75 ps (yellow arrow) but it is only after further propagation of the leading partial that the trailing will start to propagate (at 8.0 ps).

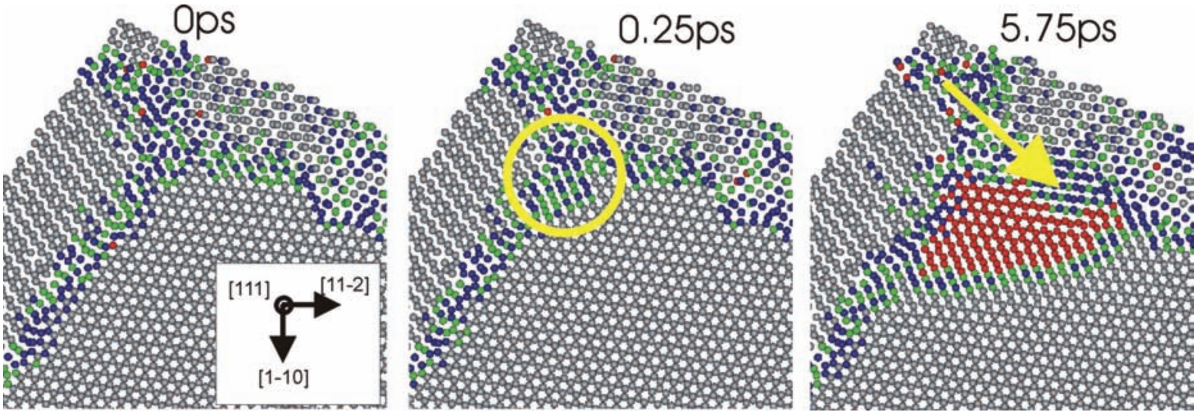

Figure 1: Early stages of nucleation and propagation of leading and trailing partial

5. Propagation

Fig. 2 displays a series of snapshots of the same atomic section and in the same orientation as in Fig. 1. At 8.75 ps the leading partial has reached a region in the GB (circled) which forms an obstacle for further propagation. Further propagation of the leading partial is only facilitated by the nucleation of a kink pair visualised first by the bulge (at 9.25 ps). A kink pile-up is formed at the pinning point of the dislocation, which continues until a maximum curvature is reached (at 11.25 ps) corresponding to a critical angle between the dislocation line and the GB plane resulting in the depinning of the dislocation (11.75 ps) and the further propagation of the leading partial. Similar simulations were performed at 5, 60 and 180 K starting from a configuration taken from the 300 K simulation snapshot where the full dislocation had already propagated to the pinning point. The time taken for the depinning is 2–3 times longer at 180 K and an order of magnitude longer for the 60 K simulation. Deppinning was not observed to occur at 5K.

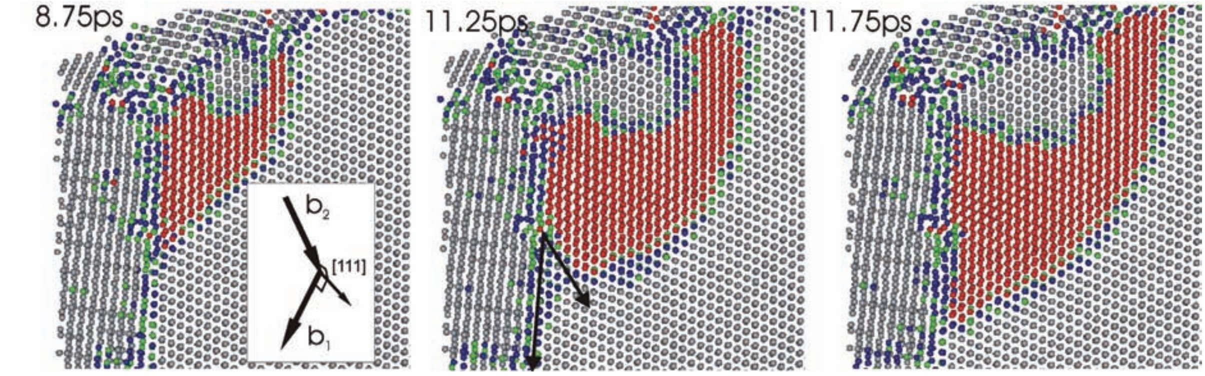

Figure 2: Propagation of leading partial, its pinning with subsequent kink pile up, and depinning due to a critical curvature.

5. Discussion

The above details of the life of a dislocation in a nc fcc metal reveal some important aspects regarding nucleation and propagation. Firstly, leading and trailing partial dislocations are not emitted at the same position and time suggesting that GB dislocation nucleation cannot be represented as a simple Frank–Read source. Secondly, GB ledges can hinder dislocation propagation - dislocations can become pinned. Finally, the present work finds that the time taken for unpinning is strongly dependent on temperature, providing evidence of a thermally activated process. In between such pinning areas, propagation of the dislocation is relatively easy and much less sensitive to temperature. These results demonstrate that dislocation propagation can play as important a role as dislocation nucleation and that this should be taken into account in any continuum model for the rate-controlling mechanism of dislocation activity in nc materials.

Acknowledgements

The authors acknowledge the financial support of the Swiss-FN (Grant No. 2000-056-835).

References

[1] H. Van Swygenhoven, P. M. Derlet, A. Hasnaoui, Phys Rev B 66 024101 (2004).
[2] P. M. Derlet, H. Van Swygenhoven, A. Hasnaoui, Philos Mag A 83 3569 (2003).
[3] J. Schiotz, K. W. Jacobsen, Science 301 1357 (2003).
[4] V. Yamakov, D. Wolf, S. R. Phillpot, H. Gleiter, Acta Mater 51, 4135 (2003).
[5] H. Van Swygenhoven, P. M. Derlet, A. G. Frøseth, Nat Mater 3, 399 (2004).
[6] A. G. Froseth, P. M. Derlet, H. Van Swygenhoven, Acta Mater 52, 5863 (2004).
[7] H. Van Swygenhoven, P. M. Derlet and A. G. Frøseth, Acta Mater. 54, 1975 (2006).
[8] P. M. Derlet, H. Van Swygenhoven, Phys Rev B 67, 014202 (2003).
[9] Y. Mishin, D. Farkas, M. J. Mehl, D. A. Papaconstantopoulos, Mater Res Soc Symp Proc 538, 535 (1999).

Size Effect in The Plastic Response of Sub-micrometer Sized Pillars: A Three Dimensional Discrete Dislocation Dynamics Study

Daniel M. Weygand[1]

Affiliation: [1]IZBS, University of Karlsruhe (TH), Kaiserstr. 12, 76133 Karlsruhe, Daniel.Weygand@izbs.uni-karlsruhe.de

ABSTRACT

The plastic behavior of single crystalline pillars with diameters between 0.5 and 2µm under uniaxial loading is simulated using a discrete dislocation dynamics simulation tool. The observed flow stress at 0.15% plastic strain shows a clear size effect: an increase in the strength of the pillars with decreasing diameter has been found. Furthermore the spread in the flow stress for different random initial dislocation configurations (same initial dislocation density) increases with decreasing sample size. Both observations agree with the experimental findings. The analysis of the dislocation microstructure shows that the density of dislocation reaction increases with increasing sample size. Despite the larger dislocation reaction density in the larger sample an initial softening for the 2µm sample is observed in the simulated plastic strain range.

1. Introduction

The plastic response of single crystalline materials, where the sample size reaches sub-micron scale, is known to be size dependent. The understanding of the possible origins for this size effect is important for the design and reliability issues of small scale devices.

Recently the size effect, characterized by an increasing flow stress with decreasing sample diameters, has also been observed for sample geometries and under loading conditions, where strain gradients are supposed to be absent, e.g. the compression experiments of micro-meter sized pillars [1-4]. These cylindrical pillars were cut out of specific grains of known orientation by FIB technique. In order to explain these experimental finding, a dislocation starvation mechanism was proposed [2], which assumes that the free surfaces of the sample act as an effective sink for dislocations during plastic deformation. The dislocations are likely to leave the smaller samples before multiplication mechanisms can occur. The loss of dislocations leads therefore to a higher flow stress in theses samples.

Classical continuum mechanics theories cannot describe size effects, as the dislocation microstructure in such small pillars can no longer be described correctly by homogenized dislocation densities and the properties of surfaces, e.g. as dislocation sink, strongly influence the possible deformation mechanisms. Therefore, the dislocation dynamics (DDD) methodology [5,6], taking explicitly into account the dislocation microstructure, is used to model the plastic response of sub-micrometer sized pillars.

2. Simulation setup

The plastic flow of idealized pillars is modeled. The chosen sample geometry is of cuboidal shape with aspect ratios of 1-2-1 where the long axis is the loading direction. The samples were deformed under uniaxial loading with an imposed strain rate of 5000/s. Simulations have been performed for samples with 0.5, 0.75, 1.0 and 2 µm diameter. The initial dislocation source distributions consist of randomly distributed Frank-Read sources with a source length of ~220nm. In the initial distribution all glide systems are equally occupied in order to avoid a preferred deformation mode. The initial dislocation density is ~2.1 10^{13} m^{-2}. The material parameters for Al where used and the DDD model allows for cross-slip [5]. All dislocation interactions in the DDD method are based on isotropic linear elasticity. The loading is applied in the (123) direction, which is a single slip orientation.

3. Results

The stress strain curves for samples of 0.5µm and a single sample of 2µm diameter are shown in Fig. 1. The curve shows a broad scatter in the results of the 0.5µm samples. Different deformation modes occur: some sample show, after an initial transition period, a periodic stress fluctuation. This behavior is linked to the periodic activation of single sources, either a pre-existing Frank Read source or one obtained after dislocation reaction, e.g. formation of glissile locks or a reaction involving cross-slip. Some of the simulations show a pronounced hardening, reaching a flow stress of more than 200MPa. In these samples reactions block the initially most active sources. With increasing stress, less favorable oriented glide systems will be activated.

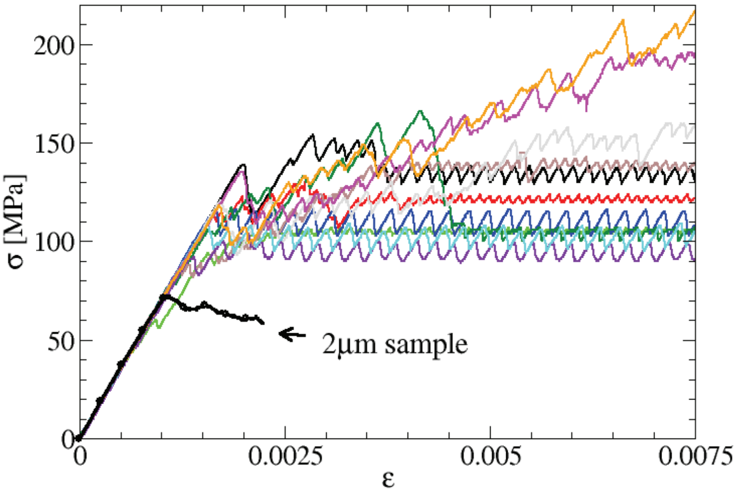

Figure 1: Stress strain curve for 0.5µm samples and a 2µm sample (indicated by an arrow).

Due to the computational demands, only one simulation has been performed for the 2µm pillar, till now. For this sample a different deformation behavior is observed. After the initial yield point, a drop of the flow stress is observed. During the dislocation microstructure evolution, the density of reaction between dislocations is increasing, allowing for new relaxation modes. Furthermore it is observed that the density of forest dislocation reaction increases with increasing sample size (Tab. 1).

Table 1: Density of forest dislocation reaction for the 1µm and 2µm samples; the density is normalized with respect to the smaller volume.

Sample diameter [µm]	Lomer lock density	Glissile reaction density	Hirth lock density	Collinear reaction density
1	3	9	0	6
2	8	11	0	12

Fig. 2 shows the flow stress at 0.15% plastic strain. The flow stress shows a clear size effect with an exponent of -0.6. The scatter in the flow stress increases with decreasing sample size.

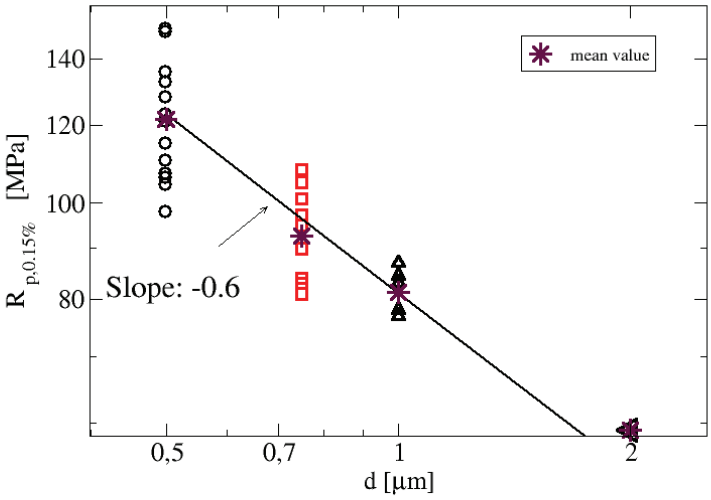

Figure 2: Flow stress at 0.15% of plastic strain. The spread is decreasing with increasing sample size.

4. Discussion

The observed plastic flow of the micro pillars under strain controlled conditions shows a pronounced size effect. The periodic stress drops in the smaller samples are comparable to the experimental strain bursts, obtained under force controlled loading conditions [3,4]. The large scatter in the stress strain curves shows that the initial dislocation microstructure plays an important role on the overall response of the sample. One possible reason for this scatter might be source limited plasticity, either due to reactions between dislocations or surface interaction, similar to the observation in thin film plasticity [7].

The strong dependency of the forest dislocation density on sample size shows that the probability of junction formation decreases with decreasing sample size. The role of reactions is twofold: on the one hand forest dislocation act as obstacles, on the other hand the glissile reaction can also play the role of a source for a new glide system. The observed softening of the 2µm samples suggests, that the sources in the initial dislocation microstructure are stronger than those forming due to reactions between dislocations.

5. Conclusion

Discrete dislocation dynamics simulations have successfully reproduced the experimentally observed size effect in the flow stress. The observed density evolution of dislocations and forest reactions support the hypothesis that the multiplication mechanism are less effective in small volumes due to the early loss of dislocations at the free surfaces. These observations have to be supplemented by more detailed analysis of the dislocation microstructure.

Acknowledgements

Financial support of the European Commission for the NANOMESO project under the contract no. NMP3-CT-2006-016710 is gratefully acknowledged.

References

[1] Uchic M.D., Dimiduk D.M., Florando J.N., and Nix W.D., Science 305(2004) 986.
[2] Greer J.R., Nix W.D., Appl. Phys. A. 80 (2005) 1625.
[3] Dimiduk D.M., Uchic M.D., and Parthasarathy T.A., Acta Materialia 53 (2005) 4065.
[4] Volkert C., Lilleodden E.T., in press, Phil. Mag. (2006).
[5] Weygand D., Friedman L.H.,Van der Giessen E., and Needleman A., Mod. Sim. Mat. Sci. Eng. 10 (2002) 437.
[6] Weygand D., Gumbsch P., Mat. Sci. Eng.A 400–401 (2005) 158.
[7] von Blanckenhagen B., Arzt E. , and Gumbsch P., Acta Materialia 52 (2004) 773.

Defect nucleation and shear instability of TiAl under different shear condition: an atomistic simulation

D. S. Xu[1], *H. Wang*[1] *and R. Yang*[1]

[1]*Institute of Metal Research, Chinese Academy of Sciences, Shenyang 110016, China*

TiAl based intermetallic alloys with good high temperature strength and creep resistance are very promising materials for high temperature parts in jet engine, but their practical applications are impeded by the room temperature brittleness. It is considered that the room temperature brittleness is due to the insufficient number of active slip system in polycrystalline TiAl, and the easiest to operate, {111}<110], consists of only 3 independent slip systems, which do not meet the requirement for the general deformation of polycrystalline material. In the last two decades, great effort has been made to explore the possibility of increasing the number of slip system or activating the deformation twinning, so that the crystal will have enough deformation mechanisms to yield a sufficient ductility for the processing and handling of the TiAl parts. In order to understand the atomic details of defect nucleation behavior and fundamental deformation mechanism, atomistic simulations were carried out using an EAM type interatomic potential. The lattice instability of this L10 structured intermetallic compound against shear under different stress conditions was simulated. The defect generation on the slip/twinning system of {111} <110], {111} <101], {111} <112] has been simulated by shearing the lattice on each of the above atomic plane, and dislocation and deformation twinning were found for the slip and twinning system, respectively. The energetics changes due to the shearing on one layer, two layers or affine shear were obtained and related to the instability under different loading, which are in agreement with the dynamic simulation of defect nucleation. Twinning-antitwinning asymmetry was found for the {111} <112] twinning system when sheared in different direction. The defect nucleation stress for the anti-twinning shear is much higher than that of the twinning shear, and the structure change was found in the lattice under antitwinning shear. Both defect nucleation stress and strain were reduced monotonically as the temperature increases. The defect nucleation stress and strain increase with the increase of the hydrostatic pressure under which the simulation was carried out. The introduction of both point defects, such as vacancy or interstitial atom, and planar defect, such as twin boundary, will decrease the defect nucleation stress and strain; planar defects have a much larger effect.

On The Arrangament Of Inhomogenity For MTM Method Used Elastic Moduli Estimation Of Particulate Composites

Safak Yilmaz,
Department of Mechanical Engineering, Technical University of Istanbul, Inonu Cad.
No. 87, 34437 Beyoglu, Istanbul , TURKEY
yilmazsaf@itu.edu.tr

ABSTRACT

The elastic moduli belonging the BCC unit cell calculated by FEM analysis and elastic moduli calculated by MTM method are compared each other for both void and rigid inhomogenity cases. For low volume fractions (Vf < 20%), FEM and MTM results are very close to each other. FEM results also close to MTM results at moderate volume fractions (20% <Vf < 45%) at the case of rigid inhomogenity. Increasing volume fraction increases the interactions beetween the inhomogenities and thus the differances between the FEM and MTM results increases with incerasing volume fractions. It was concluded that inhomogenty arrangement character in the elastic moduli estimation of MTM method is close to the BCC type inhomogenity arrangement style.

1. Introduction

The overall properties of composite materials depends not only on the properties of constituents but also the arcitecture of microstructure, i.e shape, orientation, arrangement geometries of constituents. Therefore, material engineers need a powerfull property estimation method considering all microstructural parameters for tailoring of composite materials. The computational limitations is overcome by simplification assumption; the continuum media of composite can be built up using a representive unit volume element (RVE), i.e. homogenisation method [1]. There are several idealised inhomogenity-matrix packing system called unit cell in order to built up real microstructure. Material flows during manufacturing processing can make the microstrucal geometry close to one of the idealised unit cell geometries[2]. The success of homogenisation methods depends on the presentability of RVE used instead of real microstructural geometry.

Eshelby[3], proposed a shophisticated analytical approach considiring the shape of the inhomogenity by means of Eshelby tansor and assumes that inhomegenity is embedded in continuum media having similar shape with inhomogenity. Mori-Tanaka[4] modified the Eshelby method in order to take into acount the inhomogenty interactions at the high volume fractions. The analitical solutions of Mori-Tanaka Method(MTM) can be found in elsewhere for simple spheroised shaped inhomogenities embedded into similar spheroised shaped RVE [5]. The effects of inhomogenity shape and orientation effects at the axises of spheroids can easly followed by MTM aproaches.

In this work, what kind of arrangement geometry corresponds to the consideration of MTM aproache is investigated. In order to clarify the arrangement character of MTM method, the elastic moduli calculated with finite element analysis using body centered cubic (BCC) type unit cell can be compared with the estimations of MTM aproaches.

2. Approach

BCC unit cell type idealised inhomogenity-matrix packing system can be built up by a three dimensional Voronoi tesellations containing a complete inhomogenity[6]. The shape of this Voronni cell and so the shape of the RVE for materials having BCC unit cell packing system including spherical inhomogenity is tetrakaidecahedron. Since the shape of the tetrakaidecahedron is very close to spherical geometry (surface are of tetrakaidecahedron is about 10 % greather than surface are of sphere for a certain volume), the results of finite element analysis using BCC type unit cell were chosen for comparison. BCC type unit cell and tetrakaidecahedron Voronni cell are shown in Fig. 1 schematically.

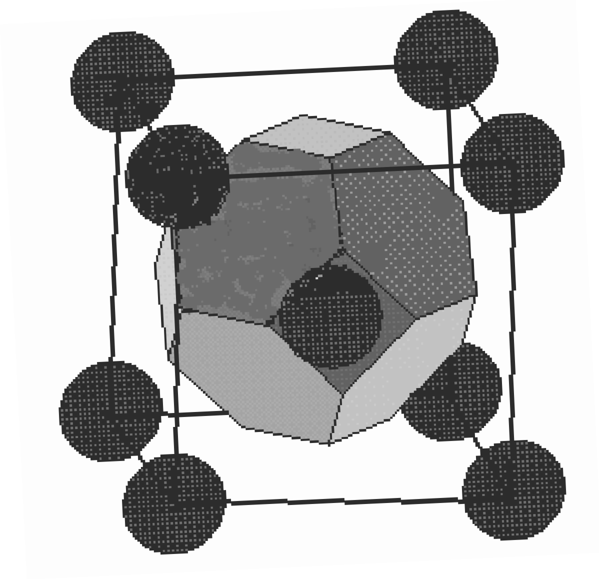

Figure 1. BBC type unit cell and corresponding Voronoi cell to built up 3D infinite periodic array of homogeneity embedded in the matrix.

The elastic moduli of BBC unit cells determined by finite elements analysis. In the FEM analysis, the opposite walls of the unit cells must remain parallel and the angles between the walls must be preserved. If the unit cell includes second phase particles, the interfaces between the phases were assumed to be strong enough to assure continuity. Models with different element sizes (meshes of different fineness) were considered for accuracy of results. The detail of such FEM investigation can be found elsewhere [7]. The case of spherical inhomogenity was chosen for comparison of FEM results and results of MTM.

In order to isolate the effect of elastic behaviour of inhomogenity and thus to clarify the pure geometrical effects, the matrix including ellipsoidal voids were considered. To appear the of stiffeness effect of imhomogenity, rigid inhomogenties were considered. The value of 10^{32} GPa used for elastic modulus of rigid inhomogenity in the MTM calculations.

4. Results and Discussions

The elastic moduli belonging the BCC unit cell calculated by FEM analysis and elastic moduli calculated by MTM method are given in Fig 1. with respect to volume fractions both void and rigid inhomogenity cases. As can be seen from Fig. 1, general agreement between the variations of FEM and MTM results depending on the volume fraction is very good.

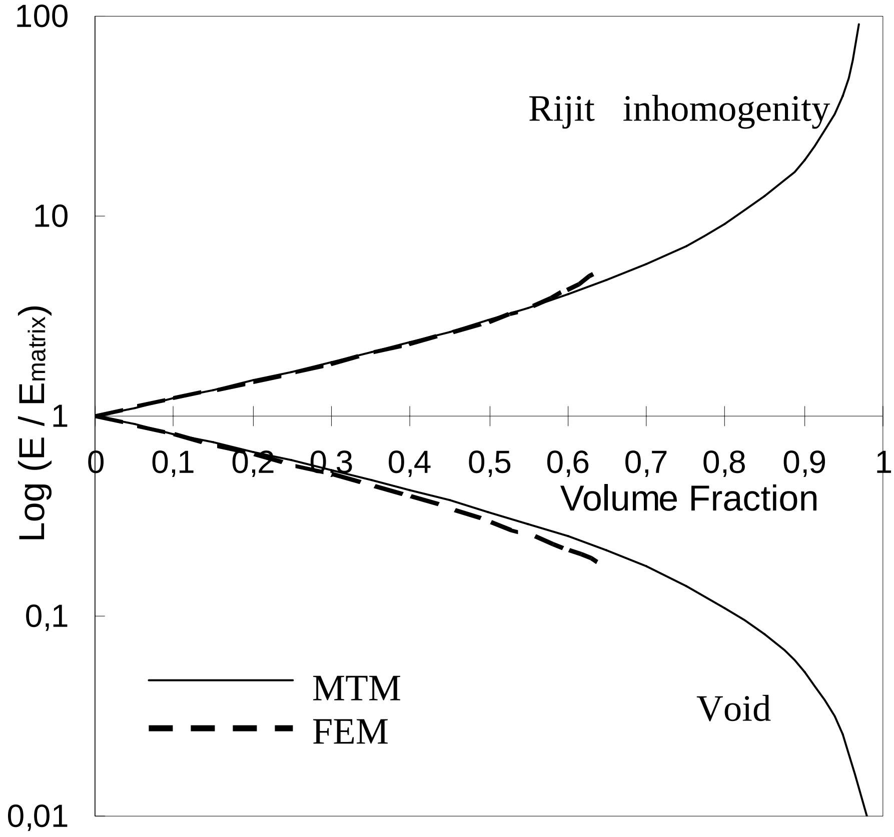

Figu [illegible]
moduli are given in logarithmic scale.

In order to apear the agreement between the FEM and MTM results, the ratio of FEM results to MTM results are ploted in Fig. 3 with respect to volume fractions. It is seen from Fig. 3 that, FEM results of BCC type arrangement very close to MTM results at low volume fractions (Vf<20 %). Since the effects of interactions between the inhomogenities are ignorable at low volume fractions, the effects of inhomogenity arrangement on the elastic moduli is not dominant at low volume fractions. After low volume fractions, interaction contrubution of inhomogenities in BCC type arangement is different than that of Mori-Tanaka modification to take into acount the inhomogenty interactions at the high volume fractions. Increasing volume fraction increases the interactions beetween the inhomogenities. Thus, the differances between the FEM and MTM results increases with incerasing volume fractions. FEM results are always lower than MTM results for void type inhomogenty. Void and rigid inhomogenty lines are also very close to each other at low volume fractions. This implies that, elastic behaviour of inhomogenity has similar geometrical effects without arrangement contrubition at low volume fractions. However, discrepency from the MTM results in the case of rigid inhomogenity is not pronounced as void case for the moderate volume fractions (20% <Vf < 45%). FEM results of rigit inhomogenity case are closer to MTM results than that of void case after low volume volume fractions althugh FEM results of rigit inhomogenity case are still lower than MTM results. On the other hand, FEM results of rigit inhomogenity case are higher than MTM results at high volume fractions. The hindered deformations at narrow gap between the inhomogenties due to the Poisson contraction effect become pronaunced while the volume fraction increasing for the case of rigid inhomogenity. Stress-strain distributions in FEM models become more homogeneous in the case of rigid inhomogenity such as assumption of MTM calculations. Hence, FEM results become more close to MTM results. It is clear that, modifications of Eshelby method can be made to take into acount the inhomogenty interactions at the high volume fractions for the case of the different kinds of special arrangenmets such as simple cubic (SC), face centered cubic (FCC), and close packed hexagonal (CPH) packing systems.

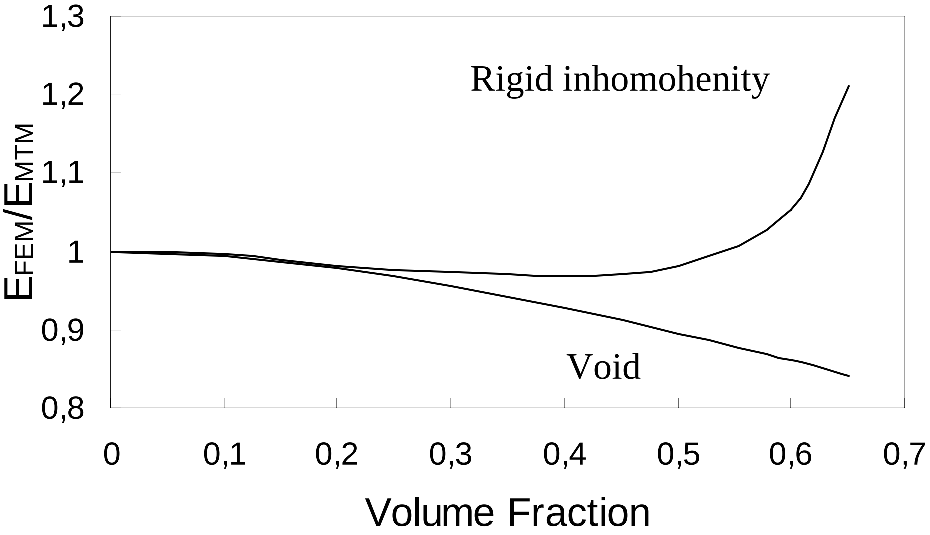

Figure 3. Comparison of elastic moduli calculated both FEM and MTM method with respect to volume fractions

3. Conclusions

Elastic moduli of continuous matrix including spherical inhomogenity calculated by MTM method and FEM analysis using BCC type unit cell for the cases of void and rigid inhomogenities. Elastic moduli calculated by both approaches were compared each other for different volume fractions. For low volume fractions, FEM and MTM results are very close to each others. FEM results also close to MTM results at moderate volume fractions in the case of rigid inhomogenity. It was concluded that inhomogenity arrangement character in the elastic moduli estimation of MTM method is close to the BCC type inhomogenity arrangement style.

References

[1]S. Nemat-Nasser, M. Hori, *Micromechanics:Overall Properties Of Heterogeneous Materials*, (North Holland, Amsterdam, 1993), p. 11.

[2] Yilmaz, S., Aran, A., *Finite Element Analysis Of The Effect Of Particle Alignment On The Deformation Behavior For A Ductile Matrix Containing Hard Particles*, Canadian Metallurgical Quarterly, **38,** No. 3, 201, (1999).

[3]J. D. Eshelby, *The Determination Of The Elastic Field Of An Ellipsoidal Inclusion And Related Problems*, Proc. Roy. Soc. London Ser., **A252**, 561, (1957).

[4]T. Mori, K. Tanaka, *Average Stress In The Matrix And Average Elastic Energy of Materials With Misfitting Inclusions*, Acta Metall Mater., **21**, 571, (1973).

[5]M. Toshio, *Micromechanics Of Defects In Solids*, (Kluwer Academic Publishers,Boston, 1998), p.74.

[6]N. Ahuja, B.J. Schachter, *Pattern Models*, (Wiley, New York, 1983)

[7]E. Weissenbek, H.J. Bohm, F.G. Rammerstorfer, Micromechanical Investigations Of Arrangement Effects In Particle Reinforced Metal Matrix Composites, Comput. Mater. Sci., **3**., 263, (1994)

From 2D HRTEM images to 3D atomistic/continuum models of GaN/Al_2O_3 interfacial region

Toby Young [1], Pawel Dluzwski [1], Joseph Kioseoglou [2], Philomela Komninou [2]

[1] *Institute of Fundamental Technological Research PAS, ul. Swietokryska 21, 00-049 Warsaw, Poland*
[2] *Department of Physics, Aristotle University of Thessaloniki, GR-54124 Thessaloniki, Greece*

In the paper we present an atomistic and finite element model of a GaN/Al_2O_3 interface including a complex net of misfit dislocations with nodes forming a 3D atomistic transition of Al_2O_3 to GaN lattice. In the first step of computer processing of the GaN/Al_2O_3 interface, a trial of the reconstruction the lattice distortion fields from High Resolution Transmission Electron Microscopy (HRTEM) observations of the GaN/Al_2O_3 interface were performed along the [1-210] zone axis. Having as input the experimental values of the lattice constants α= 3.147Å and c = 5.19Å for the GaN film, a 3D atomic configuration of the interface was constructed and HRTEM image simulations were calculated. Geometric phase analysis was then applied to the experimental and the corresponding simulated images in order to obtain the displacement and strain fields in the interfacial region. This data was used as input for Finite Element (FE) analysis. To obtain a 3D model corresponding to a few parallel misfit dislocations in the HRETM image, we multiplied the structure in such a way as to obtain an appropriately thick sample with dislocation nodes inside. In result we have obtained 3D atomistic and continuum structures in which the hexagonal net of misfit dislocations in GaN/Al_2O_3 structure was obtained. Our atomistic and continuum model were used in the analysis of physical effects observed on the interface in various cross-sections of the resultant FE mesh. From a mathematical point of view our FE constitutive model [1] comes back to the idea of continuum theory of dislocations [2,3] in which dislocation cores and dislocation nodes occupy a 3D subregion in our FE mesh.

[1] Th. Kehagias, Ph. Komninou, G. Nouet, P. Ruterana, and Th. Karakostas, Phys. Rev. 84 195329 (2001).

[2] S. Kret, P. Dłuzewski, P. Dłuzewski, and J.-Y. Laval, Phil. Mag. 83, 231 (2003).

[3] P. Dłuzewski, G. Maciejewski, G. Jurczak, S. Kret and J.-Y. Laval, Comput. Mat. Sci. 29, 379 (2004).

Atomistic Study of Structure and Failure of fcc/bcc Heterophase Boundaries

Adham Hashibon[1], [2]

[1]*Institut fuer Zuverlaessigkeit von Bauteilen und Systemen (IZBS), Universitaet Karlsruhe (TH), Kaiserstr 12, 76131 Karlsruhe, Germany*

[2]*Fraunhofer-Institut für Werkstoffmechanik IWM, Woehlerstr. 11, 79108 Freiburg, Germany*

Heterophase interfaces between fcc and bcc metals are present in many microelectronic devices and composite materials. The functional properties of these systems hinges strongly on the micro and nano-mechanics of the interfaces. The Copper-Tantalum system is a technologically important fcc/bcc interface system, since Ta may be used as a diffusion barrier to keep the Cu from interacting with the Si-chip. The structure and mechanical properties of the Copper-Tantalum interfaces are investigated via molecular dynamics and static simulations employing a specifically developed Cu-Ta interatomic potential which is based on a generalization of the embedded atom method by the addition of angular-dependent interactions, which are believed to be important in describing the structure of dislocation cores and of interfaces. Interfaces considered include those with the two well known low energy orientation relationships for fcc/bcc interfaces, namely the Kurdjumov-Sachs (KS) and Nishiyama-Wasserman (NW) orientations, for which the closed packed planes and directions are parallel to each other. In addition, interfaces formed by depositing liquid Cu on Ta free surfaces are also considered. It is found that for the equilibrium interface structure, the first layer of Cu has a distinct structure from the rest of the fcc Cu lattice. This layer facilitates the transition from the bcc to the fcc crystal structures across the interface. Results for the vacancy formation energy profile, pore nucleation and dislocations at the interface will be presented.

Molecular Dynamics Simulations of the Mechanism of Twin Boundary Migration of Nano-twinned Copper Crystals

Lan Li [1], *Nasr M. Ghoniem* [1]

[1] *Mechanical & Aerospace Engr. Dept., 48-121 Engineer IV, UCLA, 90095 - 1597 Los Angeles, United States of America*

Recently, it has been experimentally shown that nano-twinned copper can be produced by pulsed electro-plating, and that the strength is several GPa without significant loss of electrical conductivity. We present here a study of the mechanism of twin boundary migration (TBM) in copper crystals with a nano-twin structure utilizing Molecular dynamics simulations. The effects of grown-in twin size and the strain rate on the deformation process are emphasized. It is shown that the dominant deformation mode a high strain rates is by twinning and that deformation is mainly attributed to TBM. The mechanism of TBM is shown to be controlled by the nucleation and spreading of partial dislocations at the boundary interface. The dependence of the stress-strain characteristics on the strain rate and crystal geometry will be shown.

Fiber-reinforced elastomers: Effective behavior, microstructure evolution and macroscopic instabilities

Pedro Ponte Castaneda

University of Pennsylvania, Mechanical Engineering and Applied Mechanics, 19104-6315 Philadelphia, USA

This talk will present the application of a recently developed “second-order” homogenization technique to generate estimates for the effective behavior, microstructure evolution and loss of ellipticity in fiber-reinforced elastomers that are subjected to finite deformations. The main concept behind the method is the introduction of an optimally selected “linear comparison composite,” which can then be used to convert standard linear homogenization estimates into new estimates for the nonlinear hyperelastic composite. Explicit results are provided for materials with isotropic and strongly elliptic constituents. The dependence of the macroscopic response on fiber concentration, shape and orientation is elucidated. It is found that the overall behavior may lose ellipticity at sufficiently large deformations, which corresponds to the possible development of shear band-type instabilities. The reasons for this result have been linked to the evolution of the microstructure, which, under appropriate loading conditions, can induce “geometric softening” leading to the overall loss of ellipticity.

On Contact And Size Effects In Discrete Dislocation Modelling Of Wedge Indentation

A. Widjaja[1], E. Van der Giessen[1], V. S. Deshpande[2] and A. Needleman[3]

[1]University of Groningen, Dept. of Applied Physics, Nyenborgh 4, 9747 AG Groningen, The Netherlands; [2]Cambridge University, Dept. of Engineering, Trumpington Street, Cambridge CB2 1PZ, UK; [3]Brown University, Division of Engineering, Providence, RI 02912, USA.

ABSTRACT

We study the plane strain indentation of a single crystal by a rigid wedge using discrete dislocation plasticity. The dislocations are all of edge character and modelled as line singularities in a linear elastic material. The crystal has initial sources and obstacles randomly distributed over three slip systems. The lattice resistance to dislocation motion, dislocation nucleation, dislocation interaction with obstacles and dislocation annihilation are incorporated through a set of constitutive rules. Several definitions of the contact area (or contact length in plane strain) are used to illustrate the sensitivity of the hardness value in the sub-micron indentation regime to the definition of contact area.

1. Introduction

Indentation is commonly used for measuring material properties such as Young's modulus and hardness. At a sufficiently small scales, the indentation hardness is often size dependent [1], which is not captured by classical continuum plasticity. Various frameworks have been used to model indentation size effects, such as molecular dynamics [2], strain gradient plasticity [3], and dislocation dynamics [4] which is ideally suited for indentation in the (sub-) micron regime.

While indentation is a relatively simple experiment to perform, the difficulty lies in the interpretation of the outcome. Although the indentation force can be easily recorded, the hardness requires knowledge of the contact area. In this paper we report on discrete dislocation computations that use various definitions of contact area, leading to different values of the hardness, and significant variations in the predicted size effect.

2. Model

We analyse the plane strain wedge indentation of a single crystal using a discrete dislocation plasticity framework [5]. The crystal is taken to be elastically isotropic with Young's modulus $E = 70$ GPa and Poisson's ratio $\nu = 0.33$. It is considered to be symmetric with respect to the plane $x_1 = 0$, see Fig. 1(left). Plasticity takes place on a set of three slip systems inside a process window, and is accommodated by the collective motion of edge dislocations with magnitude $b = 0.25$ nm of the Burgers vector. Dislocation sources and obstacles are randomly distributed over the slip systems, Fig. 1(right).

In plane strain, the contact area is determined by the contact length in the plane of deformation. The simplest measure of contact length is the nominal contact length, $a_N = h \tan\alpha$, which is the projection of the indenter on the x_1-axis. The second is the contact length a_S estimated on

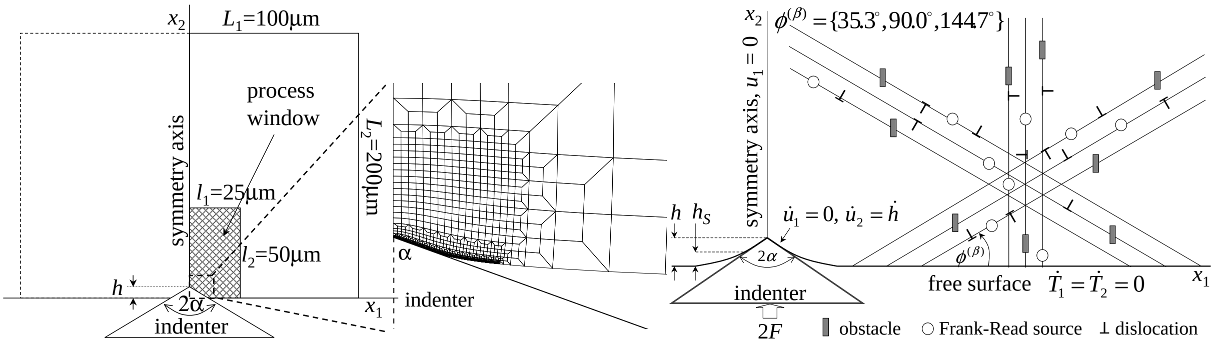

Figure 1: Left: Schematic diagram of the model. Planar symmetric single crystal indented with wedge indenter at a depth h. The tip angle of the wedge indenter is 2α. The actual area of the crystal is 16 times larger than the process window inside of which plastic deformation is accounted for. The finite element mesh (see zoomed area) is highly refined near the tip. Right: Boundary conditions on the crystal surface at a sink-in depth h_S. Dislocations, Frank-Read sources and dislocation obstacles are living on slip planes in the process window.

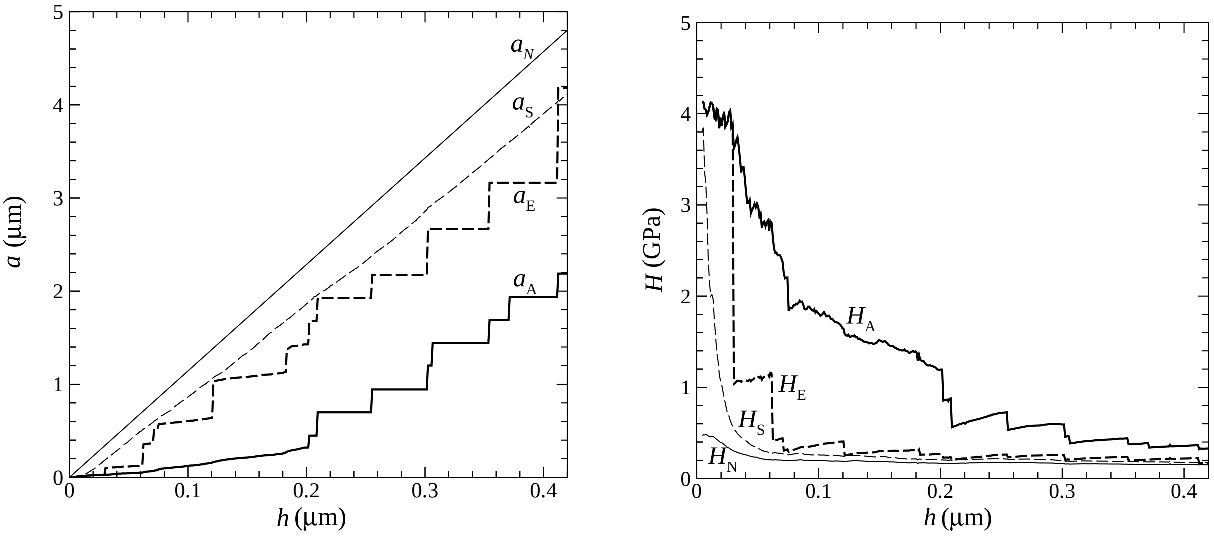

Figure 2: Left: Evolution of the four contact length measures (a_N, the nominal contact area; a_S, the Oliver–Pharr estimate; a_E, the end-to-end contact area; and a_A the actual contact area) with indentation depth h for wedges with $\alpha = 85°$. Right: Hardness versus depth. The various measures with subscripts A, E, S or N are based on the corresponding contact length measures.

the basis of the elastic unloading stiffness $S = \mathrm{d}F/\mathrm{d}h$, as proposed by Oliver and Pharr [6, 7]. The third is the contact length measured as the distance of the farthest point in contact to the $x_1 = 0$ plane, which we call the end-to-end contact length a_E. The last measure we consider is the actual contact length $a_A = \int_{x \in S_c} \mathrm{d}x$, where S_c is the surface in contact with the indenter and transmit traction that contributes to the indentation force. Evidently, $a_A \leq a_E$. The reader is referred to Widjaja *et al.* [8] for a detailed discussion.

3. Numerical Results

The evolution of the four measures of contact length and their corresponding hardnesses with indentation is shown in Fig. 2. The values of a_A, a_E and a_S are very close before plasticity starts (around $h = 6.1$ nm), but smaller than a_N; this is due to elastic sink-in. Correspondingly, H_N is smaller than the other hardness measures.

Once plasticity has initiated, the hardnesses H_A and H_E are larger than H_S and H_N. This is caused by the fact that contact lengths a_S and a_N overestimate the actual value. The difference between the nominal contact length a_N and the Oliver–Pharr estimate a_S is due to sink-in, while the difference between a_S and the end-to-end contact length a_E is due to the fact that plastic slip is neglected in the calculation of a_S. The difference between the end-to-end contact length a_E and the actual contact length a_A is due to the evolving surface roughness. This surface roughness is caused by significant steps appearing in the surface profile due to localized plastic deformation resolved by discrete dislocation plasticity. The large differences in hardness at very small depths decrease as indentation continues and more jumps in contact length occur. Eventually, all measures converge to the same value. However, the rate at which the hardness drops with h is quite a strong function of the measure of contact length used. This phenomenon is more pronounced for sharper indenters, see [8].

4. Discussion

The indentation hardness is sensitive to the definition of contact length, and, as a consequence, so is the indentation size effect. Most experimental studies of nano- and micro-indentation adopt the Oliver–Pharr procedure, while relatively simple theories of the indentation size effect apply to the nominal hardness [3]. The present discrete dislocation plasticity simulations emphasize that not only may there be a significant difference between these two measures of hardness, but both may deviate significantly from the hardness based on the actual contact area. Quite interestingly though, the predicted nominal hardness response fits well the simple Nix–Gao [3] theory, see [4].

References

[1] Q. Ma and D. R. Clarke. Size dependent hardness of silver single crystals. *J. Mater. Res.*, 10:853–863, 1995.

[2] T. Zhu, J. Li, K.J. Van Vliet, S. Yip and S. Suresh. Simulation of nanoindentation via interatomic potential finite element method. *Comput. Fluid. Solid. Mech.*, 1-2:795–799, 2003.

[3] W.D. Nix and H. Gao. Indentation size effects in crystalline materials: a law for strain gradient plasticity. *J. Mech. Phys. Solids.*, 43:411–423, 1998.

[4] D.S. Balint, V.S. Deshpande, A. Needleman and E. Van der Giessen. Discrete dislocation plasticity analysis of the wedge indentation of films. in preparation, 2006.

[5] E. Van der Giessen and A. Needleman. Discrete dislocation plasticity: a simple planar model. *Model. Simul. Mater. Sc.*, 3:689–735, 1995.

[6] W.C. Oliver and G.M. Pharr. An improved technique for determining hardness and elastic-modulus using load and displacement sensing indentation experiments. *J. Mater. Res.*, 7: 1564–1583, 1992.

[7] W.C. Oliver and G.M. Pharr. Measurement of hardness and elastic modulus by instrumented indentation: Advances in understanding and refinements to methodology. *J. Mater. Res.*, 19:3–20, 2004.

[8] A. Widjaja, A. Needleman, V.S. Deshpande and E. Van der Giessen. On contact and size effects in discrete dislocation modelling of wedge indentation. in preparation, 2006.